Thesis for the degree of Master of Engineering

Constitutive Modelling of the 6061-T6 Aluminum Alloy under High-temperature Compression Deformation Conditions

Li Sijia

Department of Mechanical Engineering

The Graduate School

Jeju National University

August 2023

Constitutive Modelling of the 6061-T6 Aluminum Alloy under High-temperature Compression Deformation Conditions

A Thesis submitted to the graduate school of

Jeju National University in partial fulfillment of

the requirements for the degree of Master of Mechanical Engineering

under the supervision of Prof. Dong Won Jung

The thesis for the degree of Master of Mechanical Engineering

by Li Sijia

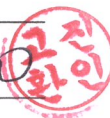has been approved by the dissertation committee.

June 15, 2023

Chair   Kang, Chang Nam

Member

Member

Constitutive Modelling of the 6061-T6 Aluminum Alloy under High-temperature Compression Deformation Conditions

Li Sijia

The Department of Mechanical Engineering
The Graduate School
Jeju National University

Abstract

Aluminum alloy is favored for its good processability, lightweight, high strength, weldability, and wear resistance. 6061 belongs to the Al-Mg-Si series and is a typical deformed aluminum alloy, which has been extensively utilized across different domains. In this paper, the 6061-T6 aluminum alloy is used as the research object. Gleeble-3800 thermal simulation testing machine is used for unidirectional thermal compression test at different temperatures (573K~783K), different strain rates (0.001~0.1s-1), and different strains (0.1~0.8, the interval is 0.1). Perform data preprocessing on the experimental data, the flow stress-strain curve is drawn to study the relationship between the stress and the strain when the material is subjected to external loading. The constitutive relation is one of the basic problems in the analysis and

application of aluminum alloy structures. The seven constitutive models that can describe the 6061-T6 aluminum alloy are established through the data obtained from the high-temperature compression experiment: modified Johnson-Cook (MJC) model, Arrhenius-Type (A-T) model, modified Zerilli-Armstrong (MZA) model, Wang-Jiang (W-J) model, SK-Paul model, Kobayashi-Dodd (K-D) model, and modified Fields-Backofen (MFB) model.

The suitability of seven models for the alloy was assessed by comparing the predicted values with the experimental results. This evaluation involved calculating the coefficient of determination (R^2) and the average absolute relative error (AARE). The aim was to obtain a more fitting constitutive equation for the 6061 alloy.

In comparison, the three models of the A-T model, MZA model, and MFB model have better-predicted structures. They are less affected by changes in temperature and strain rate, followed by the MJC model and SK-Pual model, which will change due to changes in temperature and strain rate. The W-J model and K-D model have the worst accuracy. Among them, MAZ shows a good fitting effect, and its R^2 is 0.99138, which is the closest to 1, and the AARE value is the smallest at 10.66%. It is the most accurate prediction of the flow stress of aluminum alloy material 6061-T6 at high-temperatures.

Then, in the research based on the A-T constitutive equation, the activation energy diagram is established, which describes the influence of Q value by temperature, strain, strain rate, internal microstructure of the alloy, and other factors.

고온 압축 변형 조건에서 6061-T6 알루미늄 합금 구성 모델링

이사가

제주대학교 대학원 기계공학전공

요약

두랄루민은 양호적인 가공 성능, 경량성, 고강도, 용접성, 그리고 내마모성으로 인해 매우 인기가 있다. 6061 은 Al-Mg-Si 시리즈에 속하며 대표적인 변형 두랄루민으로 다양한 분야에 널리 적용되고 있다. 본 연구는 6061-T6 두랄루민을 연구 대상으로 진행하기로 한다. Gleeble-3800 열 시뮬레이션 시험기는 다양한 온도(573K~783K), 다양한 변형공률(0.001~1s-1), 그리고 단향적 열압축 시험에 사용된다. 실험 데이터를 사전처리를 진행하여 유동 응력-변형 곡선을 제작하며, 재료는 외부 조건에서의 응력-변형 관계를 연구하였다. 기본 구조 관계는 두랄루민 구조를 분석 및 응용할 때의 가장 기분적은 문제 중 하나이다. 고온 압축 실험에서 얻은 데이터를 통해 6061-T6 두랄루민을 설명할 수 있는 7 가지 구성 모델은 설정됩니다. 이는 수정된 Johnson-Cook (MJC) 모델, Arrhenius-Type (A-T) 모델, 수정된 Zerilli-Armstrong (MZA) 모델, Wang-Jiang(W-J) 모델, SK-Paul 모델, Kobayashi-Dodd (K-D) 모델 및 수정된 Fields Backofen (MFB) 모델이다.

예측치를 실험 결과와의 비교를 통해 7 가지의 모델이 두랄루민에 적용성을 평가하였다. 6061 두랄루민에 대해 더 적합한 기본구조 방안을 얻기 위하는 목적을 가지고 있으므로 이 평가는 계산결정계수(R^2)와 평균절대상대오차 (AARE) 를 포함하였다. 비교해 보면 A-T 모델, MZA 모델, MFB 모델 이 세 가자의 모델은 더 좋은 예측 구조를 갖고 있으므로 온도와 변형률 변화의 영향을 상대적으로 적게 받았다. 다음으로 MJC 모델과 SK-Pual 모델이며 이들은 온도와 변형률 변화에 따라 변한다. W-J 모델과 K-D 모델은 정확도가 가장 낮다. 이 가운데 MAZ 는 양호적인 적합성을 드러내고 있으며 R^2 은 0.99138 로 1 에 근접하고 AARE 치가 최소인 10.66%로 나타나므로 두랄루민 재료인 6061-T6 은 고온에서의 유동적 응력에 대한 가장 정확한 예측이다.

마지막으로 A-T 기분구조 방정식에 대한 연구를 기반으로 활성화 에너지 그래프를 구축하여 온도, 변형, 응변율, 두랄루민 내부 미시적 조직 등 요인이 Q 치에 대한 영향을 설명하였다.

Acknowledgment

Two years have passed in a flash, summer has come again, and the two-year postgraduate career is ending. I am twenty-five years old this year, and two years have flown bs just yesterday. In August 2021, I stepped into South Korea for the first time and entered Jeju National University for the first time. Everything was new and unfamiliar. After two years of various things, I can now be on my own. In the past two years, wherever I look, there are memories.

First of all, I would like to express my sincere gratitude to my thesis advisor, Professor Dongwon-Jung. Professor Jung is known for his rigorous teaching approach, extensive academic knowledge, and responsible work ethic, which have greatly benefited me academically and personally. Throughout the process of topic selection and revision of my entire thesis, Professor Jung's meticulous review and patient guidance have been indispensable. I will always remember his teachings and strive to work hard, continuously improve, and surpass myself, whether it is in academic pursuits or in personal and professional endeavors.

Furthermore, I am thankful to my family, especially my parents Li Yongming and Tian Jinyan, for their devoted care throughout these 25 years. I am particularly grateful for their financial and emotional support over the past two years, which enabled me to pursue my studies without worries or burdens. I want to thank my younger sister Li Sitian for her caring nature and the joy she shares with me, which brings me a sense of relaxation. I am grateful to my cousin Li

Dan, who is a university professor, for her support and guidance in my academic pursuits. Her assistance has helped me clarify my goals and achieve them more efficiently.

Next, I would like to extend my appreciation to my lab mate and best friend, Chen Wenning. He has been the person I have spent the most time with over these past two years. We have supported and overcome challenges together along this journey, helping each other through problems and difficulties. I am grateful for his academic support and care for me in personal matters.

Furthermore, I am grateful to all the professors in the School of Mechanical Engineering. I am thankful for the knowledge imparted by professors from various disciplines. And all my friends Krishna Singh Bhandari, Shahid Aziz, Muhammad Awais Farooqi, Song Anran, Peng Haoruo, Li Jiqiong, etc. I am grateful for their various forms of assistance and the countless times they extended a helping hand when I encountered difficulties.

The road is long and obstructed, but if you keep going, you will reach your destination.

Contents

List of figures

List of tables

List of abbreviations and symbols

Commonly used notations

※ Some symbols appear more than once, their specific meaning follows from their context.

JC	Johnson-Cook
MJC	Modified Johnson-Cook
A-T	Arrhenius-type Model
MZ-A	Modified Zerilli-Armstrong Model
W-J	Wang-Jiang Model
K-D	Kobayashi-Dodd
MFB	Modified Fields–Backofen Model
DRV	Dynamic recovery
DRX	Dynamic recrystallization
σ_y	frictional resistance of dislocation movement in the grain
σ_i	yield strength of a single-grain metal
d	grain size
K	constant
T	deformation temperature
T_m	absolute temperature of the melting point of the metal

$\dot{\varepsilon}$	strain rate
μ	shear modulus
b	Burger's vector
ρ	dislocation density
S	standard deviation
σ	flow stress
$\bar{\sigma}$	mean flow stress
m'	the number of repeated experiments
n'	the number of true strain points specified
A	material constant
B	material constant
C	material constant
m	material constant
n	material constant
$\dot{\varepsilon}^*$	dimensionless strain rate
T^*	dimensionless temperature
$\dot{\varepsilon}_r$	reference strain rate
T_r	reference temperature
T_m	melting temperature

B_i	material constant
Z	Zener-Hollomon parameter
Q	activation energy
R	gas constant (8.314 Jmol^{-1}K^{-1})
n_1	material constant
β	material constant
α	material constant
C_i	material constant
$\dot{\varepsilon}_0$	ultimate strain rate
U	activation energy
k	Boltzmann's constant
σ_0	stress at 0 K
U_0	activation energy at 0 K
ε_p	plastic strain
T_a	room temperature
H	material constant
G	material constant
n_c	work-harding contant
m_c	strain-rate sensitivity index

b	material contant
s	an exponent for the work softening influence
v	a attempt frequency
$\bar{v}$	average apeed
$\Delta G(\sigma_s)$	free energy of the activuty
ΔF	total free energy
τ	external stress
AARE	average absolute relative rrror
R^2	correlation coefficient
N	the number of data point
E_i	experimental value
P_i	predicted value
$\bar{E}$	the average value of experimental values
$\bar{P}$	the average value of predicted values

1 Introduction

1.1 Introduction of materials

6061 aluminum alloy is a common aluminum alloy that is composed of aluminum, magnesium, silicon, copper, and other elements. Magnesium and silicon are the primary elements used to form the Mg_2Si phase. Although its strength is not as good as the 2XXX or 7XXX series, it has good processing performance and corrosion resistance. The following are some characteristics of 6061 aluminum alloy:

(1) Good processing performance: 6061 aluminum alloy can be formed, cut, drilled, milled, and welded by various processing methods. This alloy can be cold-worked and hot-worked, and the processed product has a smooth surface and is not easy to crack.

(2) Corrosion resistance: Due to the addition of elements such as magnesium and silicon, 6061 Aluminum has good corrosion resistance and can be used in harsh environments, such as seawater, chloride, nitrate, and other retestable media.

(3) Good weldability: 6061 aluminum alloy has good weldability and can be connected by various welding methods. This alloy has high welding strength and no pores, cracks, and other defects at the interface.

In general, 6061 aluminum alloy has Extraordinary physical properties, corrosion resistance, and processing performance, and has been widely employed in diverse areas, as shown in **Fig.**

제주대학교 중앙도서관
JEJU NATIONAL UNIVERSITY LIBRARY

1.1. Typical uses include:

Fig.1.1 Applications files of 6061-T6

The application of strip materials is widely seen in various industries including aerospace, defense, decoration, transportation, packaging, construction, electronics, and aviation.

Aluminum materials for aerospace are used to make rotors, fuselage frames, aircraft skins, girders, and landing gear struts, propellers, fuel tanks, as well as in the forging of rocket rings and the construction of spacecraft panels, etc.

Aluminum is a versatile material widely used in the production of electronic home appliances. It can be found in a lot of components such as refrigerators, conductors, busbars, cables, wiring, electrical components, air conditioners systems, and other applications. The material is available in various specifications, including round and square rods. Some of its common uses are in aerospace fixtures, electrical fixtures, and communication equipment.

Aluminum materials commonly used in printing are typically utilized for the production of PS

2

plates. They serve as a novel material in the printing industry, specifically for automated plate making and printing processes.

Aluminum materials for transportation are used for car body structural materials of railway passenger cars, automobiles, high-speed passenger cars, subway vehicles, body panels, doors, wheels, automotive engine parts, shelves, radiators, and ship materials.

Aluminum materials play a significant role in the packaging industry, particularly in the manufacturing of various containers such as barrels, bottles, cans, lids, and packaging foils. These aluminum materials are commonly used in the form of thin plates and foils, serving as versatile metal packaging materials. Their wide-ranging applications encompass packaging in industries such as pharmaceuticals, beverages, food, cigarettes, cosmetics, and industrial products.

Aluminum alloys for architectural decoration are mainly widely used in windows of building structures, decorative surfaces, and suspended ceilings, etc., because of their welding performance and nice corrosion resistance, excellent process performance, sufficient strength. Such as checkered panels, , profiled panels, color-coated aluminum panels, aluminum profiles for curtain walls, etc. The basic state codes of aluminum alloys are shown in **Table 1-1**:

When it comes to heat-treated aluminum alloys, the state code commonly includes the letter T followed by one or more Arabic numerals, indicating the T-subdivision state (TX state) of the alloy.

The number following the T specifies the heat treatment procedure required for the specific application, and further information can be found in **Table 1-2**.

3

Table 1-1 The basic state codes of aluminum alloys:

Code	Processing state	Features
F	Free processing	This state is reserved for products with specific work hardening and heat treatment requirements during the forming process. However, the mechanical characteristics of products in this state are indeterminate, which is an unusual occurrence
O	Annealing	This situation is mostly applicable to processed products that have been fully annealed, where this state occasionally exhibits the lowest strength among the available options.
H	Work hardening	This state is appropriate for products that experience an increase in strength due to work hardening. Once the work hardening is complete, the product additional heat treatment is applied to reduce the strength of the material. Typically, this state is employed for materials that do not require heat treatment for strengthening.
W	Solution heat treatment	This state is unstable and is used exclusively for alloys that naturally age at room temperature after solution heat treatment. It is important to note that this state code indicates the ongoing natural aging process which is not a common occurrence.
T	Heat treatment	Unlike the F, O, and H states, the T state is used for products that have been stabilized after heat treatment, with or without work hardening. The utilization of the T code necessitates the inclusion of one or more Arabic numerals, commonly denoting heat-treated alloys with enhanced strength.

Table 1-2 Heat treatment program for TX state:

Subdivision status (TX status)	Heat treatment procedure
T1	This state is achieved when the product is cooled through a high-temperature forming process and allowed to age naturally to a stable state. It is typically used for products that have not undergone any cold processing, such as straightening and leveling, which do not affect their mechanical properties limits.
T2	This state is achieved by cooling the product through a high-temperature forming process and allowing it to age naturally to a stable state after undergoing cold working. It is primarily used for products that have undergone both high-temperature forming and

4

	cold processing, such as straightening and flattening, in order to improve their strength.
T3	The material undergoes cold working and natural aging to reach a stable state after solution heat treatment, making it ideal for products that require cold straightening, working, and leveling to enhance its strength post-heat treatment.
T4	The material is naturally aged to achieve a stable state following solution heat treatment, making it appropriate for products that don't require cold working after heat treatment. While straightening and leveling can still be performed, they don't affect the mechanical properties limit. The material is then naturally aged for further enhancement of its properties.
T5	This material is produced through high-temperature shaping and subsequent artificial aging. It is well-suited for high-temperature forming of products, eliminating the need for cold processing. Straightening and leveling procedures can be carried out while maintaining the mechanical property limit. Artificial aging is then applied to enhance the material's properties.
T6	This material undergoes artificial aging following solution heat treatment and is appropriate for products that don't require cold working after heat treatment. While straightening and leveling can still be performed, they won't affect the mechanical property limit. The material is then artificially aged to further enhance its properties.
T7	This material is artificially aged after solution heat treatment and is suitable for products that require specific important properties obtained by exceeding the highest peak point on the aging curve during artificial aging. This allows for the enhancement of strength after solution heat treatment.
T8	This material undergoes cold working after solution heat treatment, followed by artificial aging, and is ideal for products that require enhanced strength achieved through cold processing, straightening, or leveling.
T9	This material is artificially aged after solution heat treatment and cold working, and is suitable for products that require increased strength achieved through cold processing.
T10	This material is cold-worked and artificially aged after being cooled through high-temperature forming and is ideal for products that require enhanced strength achieved through cold processing, straightening, or flattening.

1.2 Overview of Methods for Evaluating Mechanical Properties of Materials

The mechanical properties of materials are essential indicators for evaluating the quality and reliability of materials, and testing is the main method for evaluating the mechanical properties of materials. Depending on the performance indicators to be evaluated and the test conditions, there are a variety of different test methods to choose from. Some of the main test methods are described below.

(1) Tensile test: Place the sample on a tensile machine, apply tension along the sample's axial direction, measure the tensile force and elongation, and calculate the elastic modulus, ultimate strength, yield strength, and other mechanical properties of the material.

(2) Compression test: Put the sample on the compressor, apply a compressive load along the axial direction of the sample, measure the compressive force and compressive deformation, and calculate the mechanical properties such as compressive strength and yield strength of the material.

(3) Bending test: Put the sample on a bending machine, apply a bending load, measure the bending force and bending deformation, and compute the material's mechanical characteristics, such as bending strength and elastic modulus of the material.

(4) Torsion test: Place the sample on a torsion machine, apply a torsional load, and measure the torsional force and torsion angle to calculate the mechanical properties, such as the shear strength of the material.

제주대학교 중앙도서관
JEJU NATIONAL UNIVERSITY LIBRARY

(5) Hardness test: Press the needle of the hardness tester into the surface of the sample, and measure the indentation depth or diameter of the needle to calculate the hardness of the material.

(6) Impact test: Impact load is applied by an impact testing machine, and impact absorption capacity and impact toughness is measured to evaluate the durability of materials under impact load.

(7) Fatigue test: use a fatigue testing machine to apply cyclic loads to measure the fatigue life and fatigue limit of materials under multiple cyclic loads.

In addition to the above test methods, there are other special test methods, such as high-temperature compression tests, tensile-shear composite tests, nano-indentation tests, etc., which can more accurately evaluate the special properties of materials. The selection of an appropriate test method depends on the material properties to be evaluated and the test conditions required.

1.3   Compression Molding Process Overview

1.3.1 Low temperature compression and high-temperature compression

Both low-temperature and high-temperature compression are employed as testing methodologies to analyze the mechanical properties of materials [1]. However, they differ significantly in terms of the test conditions employed during the experiments.

Low-temperature compression tests are usually carried out at or below room temperature, and

제주대학교 중앙도서관
JEJU NATIONAL UNIVERSITY LIBRARY

the test temperature range is usually between -196°C and room temperature. Low-temperature compression tests usually require placing the sample in a low-temperature environment and testing the stress-strain properties and rheological behavior of the material through compression loading. The main applications of low-temperature compression tests include failure analysis of materials, research on plastic deformation mechanisms, research on the strength and toughness of materials, etc.

In contrast, high-temperature compression tests need to be carried out in a high-temperature environment, and the test temperature is usually between room temperature and thousands of degrees Celsius. A high-temperature compression test can be used to study the rheological behavior, deformation mechanism, deformation stress distribution, yield strength, and other mechanical performance parameters of materials in a high-temperature environment. High-temperature compression test has important application value in the research, development, and application of materials.

Compression at high-temperatures is a test method used to evaluate the plastic behavior and high-temperature mechanical properties of materials under high-temperature conditions[2]. At present, the high-temperature compression test has become one of the important means to study and evaluate the plastic behavior and high-temperature mechanical properties of high-temperature materials such as metal materials, ceramic materials, and composite materials. In terms of test methods, constant velocity compression test, thermal simulation test, cell simulation test, Gleeble simulation test, etc., are commonly used test methods, and different test methods are suitable for different types of materials, and strain rate ranges. In terms of test

equipment, atmosphere furnace test, vacuum furnace test and resistance furnace test are common high-temperature compression test equipment. In terms of test conditions, factors such as temperature, strain rate, strain, and sample geometry have important effects on test results and should be selected and controlled according to specific conditions. In terms of data processing, methods such as rheological analysis, finite element simulation, and statistical analysis are widely used in the processing and analysis of high-temperature compression test data.

1.3.2 Principles and advantages of high-temperature compression

The high-temperature compression test operates on the principle of subjecting the material to compression and load within a high-temperature environment. By measuring the material's mechanical performance parameters, such as stress, strain, and deformation under high-temperature conditions, this test allows for the evaluation of the material's high-temperature mechanical properties and reliability. During high-temperature compression testing, the testing machine measures the stress and strain of the material under elevated temperature conditions, enabling the derivation of the stress-strain curve. By analyzing the test data allows for the evaluation of the material's rheological behavior and mechanical performance parameters, such as yield strength, strain hardening exponent, stress relaxation rate, etc., can be obtained to evaluate the performance and reliability of the material in a high-temperature environment. The advantages of high-temperature compression test are as follows:

(1) Provide comprehensive performance data: The high-temperature compression test can

제주대학교 중앙도서관
JEJU NATIONAL UNIVERSITY LIBRARY

provide the compression performance data of the material in the high-temperature environment so as to comprehensively evaluate the application performance and reliability of the material in the high-temperature environment[3].

(2) Simulate the actual application environment: High-temperature compression tests can simulate the high-temperature environment in some actual engineering applications, such as applications in the fields of engines, aerospace vehicles, nuclear power plants, etc., so as to more accurately evaluate the performance and reliability of materials.

(3) Research on material deformation and damage behavior: high-temperature compression tests can study the deformation and damage behavior of materials under a high-temperature environment[4], such as plastic deformation, fracture, fatigue, etc., and provide necessary data for material research.

(4) Improve the level of material design: High-temperature compression tests can provide necessary performance data for material design to guide the rational design and optimization of materials, thereby improving the application performance and reliability of materials.

In conclusion, the high-temperature compression test has a wide application value in the field of material science and engineering[5]. With the continuous development and improvement of test methods, equipment, and data processing technology, the research on high-temperature plastic behavior and high-temperature mechanical properties of materials will be more in-depth, comprehensive, and precise.

1.4   Tissue Mechanical Properties Research

Grain size is an important parameter of grain size in the crystal structure of metals and alloys [6], which exerts a considerable influence on the mechanical characteristics of metals and alloys. Changes in grain size can lead to changes in the mechanical properties, plasticity, and toughness of metals and alloys.

1.4.1 The Effect of Grain Size on the Strength of Metals and Alloys

The grain size directly influences the strength of metals and alloys [7]. In general, finer grains increase the strength of metal materials because there are relatively more grain boundaries between finer grains, and the diffusion path for dislocation movement and crystal slip is shorter, thus hindering the dislocation[7]. The wrong movement improves the yield strength, tensile strength, and hardness of the material. The yield strength of the material is governed by the grain size d, following the empirical equation known as the Hall-Petch relationship:

$$\sigma_y = \sigma_i + K d^{-\frac{1}{2}} \tag{1-1}$$

where σ_y is the frictional resistance of dislocation movement in the grain, and d is the grain size. σ_i is the yield strength of a single-grain metal, and K is the constant associated with the influence of grain boundaries on strength captures the relationship between grain boundaries and the mechanical strength of the material, which is related to the structure of the grains and has little to do with temperature[8].

1.4.2 Effect of Grain Size on Plasticity and Toughness of Metals and Alloys

11

The plasticity of metals and alloys is significantly influenced by the grain size as well. In general, fine grains help to improve the plasticity of metals and alloys because fine grains can provide more grain boundaries, thereby increasing the yield point of the material and restricting the movement of dislocations, thereby improving the plasticity of the material. In addition, fine grains can also inhibit crystal slip and grain boundary diffusion, which contributes to the improvement of the fracture toughness of the material.

For the toughness of metals or alloys, coarse grains will make a decrease in the toughness of metals and alloys because, inside coarse grains, there are relatively few grain boundaries, and dislocation movement is easier, thereby reducing the toughness of the material. On the contrary, fine grains restrict the movement of dislocations and enhance the effect of grain boundary strengthening, which contributes to the toughness of the material.

1.4.3 Effect of Grain Size on Fatigue Properties of Metals and Alloys

(1) Fatigue Life: Smaller grain size generally contributes to improved fatigue life of metals and alloys. Fine grains can limit the growth of cracks and slow down the rate of crack formation and growth, thereby prolonging the fatigue life of the material [9]. This is because there are many grain boundaries in the fine grains, and the grain boundaries can hinder the expansion of cracks, thereby inhibiting the expansion of cracks. However, cracks are easy to form inside the coarse grains, and the cracks are easy to expand in the grain, resulting in a decrease in fatigue life.

(2) Cyclic Hardening Behavior: Grain size also has an effect on the cyclic hardening behavior

of metals and alloys[10]. Cyclic hardening is the phenomenon in which a material gradually

hardens under cyclic loading. Studies have shown that fine grain size can reduce the cyclic

hardening rate of metals and alloys. That is, the material hardens at a slower rate under cyclic

loading. This is because the fine grains can limit the movement and aggregation of dislocations

and reduce the accumulation of dislocations[11], thereby reducing the cyclic hardening

behavior of the material.

Overall, finer grain size contributes to improved fatigue properties of metals and alloys,

including increased fatigue life, reduced crack growth rate, and slowed cyclic hardening

behavior. Therefore, in the design and preparation of metals and alloys, controlling the grain

size is an important means that can be used to improve the fatigue properties of materials.

1.5   Flow Stress of Thermal Deformation of Metal Materials

The deformation temperature $T > 0.6T_m$ (T_m is the absolute temperature of the melting

point of the metal [12]), and the deformation with a strain rate exceeding $10^{-4}s^{-1}$ is called

thermal deformation. In the thermal deformation processing, there are structural changes and

metal flow inside the metal, so thermal deformation has a very important influence on the

structure, performance and flow stress of the metal [13].

1.5.1 Flow Stress of Thermal Deformation of Metal Materials

The flow stress of a material, determined by the yield limit at a specific deformation

temperature, deformation degree, and deformation rate [14], serves as a fundamental parameter for characterizing its plastic deformation capability [15]. The flow stress of a material plays a crucial role in determining the applied load and energy consumption during plastic deformation. It serves as a significant indicator for assessing the material's plastic processing performance and plays a pivotal role in equipment selection and validation.

During the plastic processing of metals and alloys, the magnitude of the flow stress of the material determines the required load and energy consumption during deformation, usually determined by the material at different deformation temperatures T, deformation rate $\dot{\varepsilon}$, and deformation degree ε under single-item compression (or tension), the yield stress, peak stress or steady-state stress value is measured, and it is also related to other conditions such as material composition, grain size, heat treatment system, and deformation history, that is, the available **Eq. (1-2)** can be express:

$$\sigma = f(\varepsilon, \dot{\varepsilon}, T,) \tag{1-2}$$

1.5.2 Softening Mechanism of Thermal Deformation of Metal Materials

Work hardening occurs when metallic materials are deformed at lower temperatures with increasing dislocation density.

When deformed at a higher temperature（$T > 0.6T_m$）, the material is in a highly plastic state, and there are work hardening and dynamic softening phenomena at the same time. The true stress-true strain curve of the material is precise because of the interaction of these two contradictory factors. It has the characteristics of first hardening, then softening, and then a

14

steady state. Dynamic recovery (DRV) and dynamic recrystallization (DRX) are the dominant mechanisms governing material softening during thermal deformation, and its typical rheological curve shape is shown in **Fig. 1.2**, and **1.3**.

(1) DRV

At extremely low levels of deformation, the stress exhibits a linear relationship with the strain, indicating a proportional response. It is generally believed that work hardening is related to the dislocation density. That is, the flow stress is proportional to $^{\mu b}\!\sqrt{\rho}$, where can be expressed as proportional to the square root of the product of the shear modulus (μ), Burger's vector (b), and dislocation density (ρ). When the deformation is high, the growth trend of the dislocation density will gradually weaken, so the work-hardening effect will gradually be lower than the linear growth law. This phenomenon is mainly because that the recovery phenomenon during the deformation process, so it is called DRV; its typical rheological profit curve is shown in **Fig. 1.2**. DRV mainly occurs during the thermal processing of metals with high stacking fault energy, such as Al, α-Fe and their alloys. The DRV in the deformation process can be regarded as a process similar to the usual static recovery. In this process, screw dislocations slip and edge dislocations climb, resulting in dislocation cancellation and rearrangement, and the process of "polygonization": the reaction between dislocations, such as dislocations of opposite signs on the same slip plane undergo merging and disappearing. Alternatively, the dislocations can react with vacancies in the dislocation line, causing them to climb and undergo a process known as dislocation climb. causing them to transition from their initial horizontal arrangement to a vertical arrangement. [16]. The crux of this process lies in

15

the transformation of dislocations from a high-energy mixed configuration to a low-energy

ordered configuration, resulting in the formation of vertically aligned dislocation walls or sub-

grain boundaries and ultimately leading to a more refined internal structure of the grain.

Therefore, in this stage, the internal stress of the crystal is greatly reduced, the strength is

slightly reduced, and the plasticity is slightly increased.
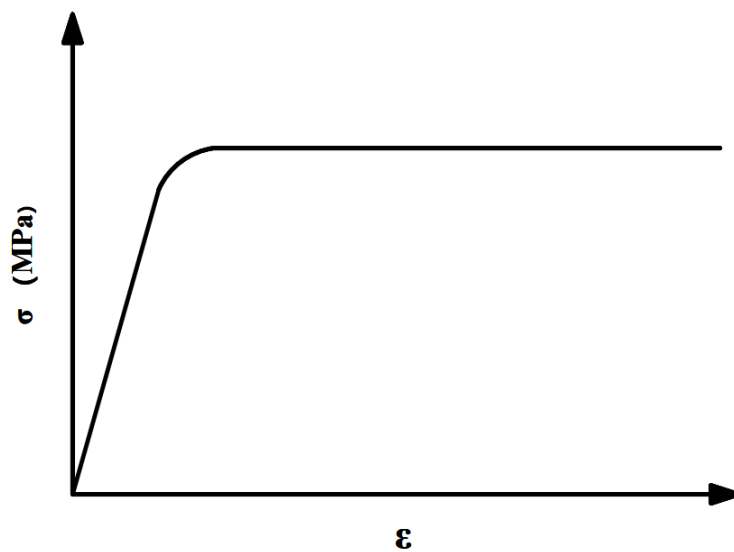
Fig. 1.2 Typical flow stress curves under thermal deformation conditions

As shown in **Fig 1.2**, when the metal material undergoes DRV from thermal deformation, It

can be primarily divided into three distinct stages: The micro-deformation stage is the first one.

At this time, The strain rate in the material progressively increases from zero to reach the

desired strain rate set for the test, the work hardening rate is very high, and the true stress-

strain curve exhibits an approximation of a linear relationship. When the stress reaches the

yield stress, the strain enters the second stage. At this time, the material begins to undergo

DRV to cause softening, and the rate of work hardening gradually decreases, although the

softening effect remains less pronounced compared to the hardening effect. The first two stages are also called the transition deformation stage. Finally, it enters the third stage, which is the steady state deformation stage. At this time, the softening effects of DRV counterbalance work hardening, as the accumulation of dislocations resulting from deformation approaches a rate of elimination due to DRV. This dynamic equilibrium is established when a balance between these two opposing mechanisms is achieved, so the last curve is close to the horizontal line [17].

In the actual thermal processing deformation, the amount of deformation is generally large, and the deformation is usually located in the deformation stage of the problem.

(2) DRX

DRX mainly refers to the process of recrystallization nucleation and growth under appropriate deformation conditions (deformation temperature, strain rate, deformation degree, etc.) when the material undergoes plastic deformation at high temperatures [18], discontinuous DRX and continuous DRX are the primary mechanisms observed during high-temperature plastic deformation, etc., the typical stress-strain curve of metals that undergo DRX in the processing range is shown in **Fig. 1.3**. The DRX behavior of materials not only significantly impacts the flow stress during high-temperature plastic deformation. [19], but also is a decisive factor in determining the final structure and performance of the product. DRX mainly happens in metals under low stacking fault energy conditions, such as Cu, γ-Fe, Ni, and their alloys. This type of alloy is prone to stacking faults. The stacking fault band in the extended dislocation is wider, the cross-slip and climb of the dislocation are difficult, and it is not easy to produce DRV.

Therefore, during the thermal working process, a sufficiently high dislocation will accumulate local density, leading to DRX.
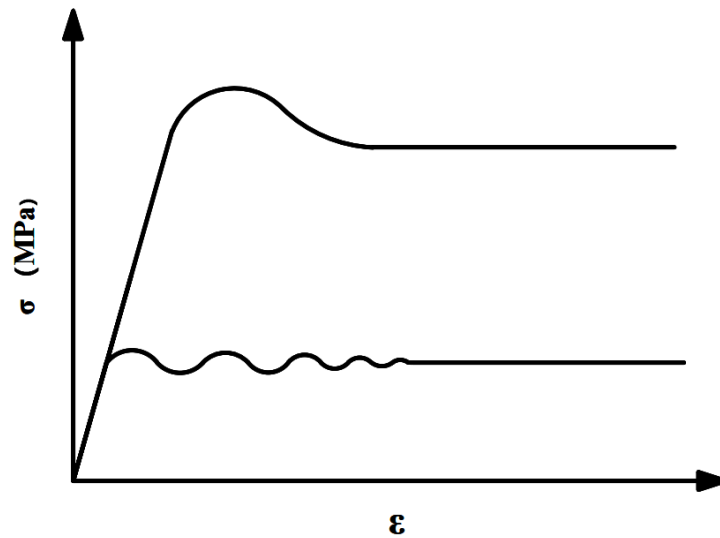
Fig. 1.3 Typical DRX flow stress curve (DRX) under dynamic and thermal deformation conditions

As shown in **Fig. 1.3**, when DRX occurs during the thermal processing of metal materials, the curve rises rapidly to a peak at low temperature and high strain rate and then softens due to DRX, reducing the flow stress to a certain value between the peak stress and the yield stress, and then keep basically stable, that is, in the stable deformation stage, this type of recrystallization is called continuous DRX. At elevated temperatures and low rates of strain, metals undergo discontinuous DRX. At this time, the softening resulting from DRX alternates with the deformation and subsequent re-hardening of recrystallized grains [20], and the rheological curve may appear periodically similar to sawtooth rheological characteristics. Each peak corresponds to the start of a new DRX, after which the softening effect is greater

제주대학교 중앙도서관
JEJU NATIONAL UNIVERSITY LIBRARY

than the hardening effect, causing the curve to descend. Each trough represents the completion of recrystallization. Afterward, the curve exhibits an upward trend as the hardening effect surpasses the softening effect. [21]. When the storage energy accumulates to a certain extent, new recrystallization begins, the volume fraction of recrystallization in the metal increases [22], and the interaction between softening and hardening becomes less and less obvious, so that the rheological curve tends to be stable.

1.6 Constitutive equation

The constitutive equation represents a mathematical model that captures the mechanical response of materials when subjected to stress. It expresses the relationship between stress and strain of materials through mathematical formulas or equations. And the mechanical response of materials is described when subjected to external loads.

It can help material research through material performance prediction, material design and optimization, material processing simulation, material damage and fracture analysis, and new material research and development. There are three main categories: Phenomenological-based models and empirical mathematical models based on experiments or experience, which are usually fitted by experimental data, and do not involve detailed consideration of the internal microstructure and mechanism of materials[23], [24]. Phenomenological models usually describe the macroscopic mechanical behavior of materials by fitting experimental data, such as fitting the stress-strain curve of materials through experimental data; Physical-base models

are mathematical models based on the microstructure and mechanical mechanism of the material. The form is relatively complex, and the macroscopic mechanical behavior of the material can be described through the physical properties and mechanical mechanism of the material[25], [26]. Physical models are usually based on microscopic mechanisms such as the crystal structure of materials, intermolecular interactions, dislocation movement, and grain boundary behavior, and combine experimental data and theoretical assumptions to construct macroscopic mechanical models of materials; Intelligence-based models based on machine learning and artificial intelligence technology, establish mechanical models of materials by learning and training a large amount of experimental data [27]–[29]. Intelligence-based models can predict the macroscopic mechanical behavior of materials by learning and identifying patterns and regularities in material data without prior in-depth knowledge of the material's physical mechanisms.

In the field of materials science and engineering, the constitutive equation holds significant importance in studying the mechanical properties, behavior, and response of materials, especially in the design, processing, damage, and fracture analysis of materials. The form of constitutive equations is usually based on experimental data and theoretical assumptions, which can be simple linear models or complex nonlinear models to suit the mechanical behavior of different materials.

1.7 The research content and significance of this paper

Metal materials are usually strain-sensitive. When subjected to dynamic loads such as explosions, impacts, and collisions, their mechanical response characteristics are different from those in quasi-static conditions and are usually accompanied by plastic deformation and fracture damage. The suitable constitutive model is the key to accurately predicting the mechanical response of materials under external loads. Therefore, it has a great significance for designing and optimization of protective structures to carry out research that can describe the constitutive relationship of metal materials under different strains and loads.

In order to better understand the flow stress of 6061-T6 aluminum alloy, this study uses Gleeble-3800 thermomechanical simulator at different temperatures (573K~783K) and different strain rates ($0.001s^{-1}$~ $1 s^{-1}$) was subjected to high-temperature compression tests, and the compression rate was 80%. And then, the stress-strain data of 6061 were obtained.

In this paper, seven widely used constitutive models are used to describe the flow behavior of 6061-T6 aluminum alloy [30]–[34].

The above seven constitutive equations that can track the 6061-T6 aluminum alloy were established through the data obtained from the high-temperature compression experiment, the predicted values were compared with the experimental results, and the seven types were evaluated by calculating the R^2 and the AARE. The applicability of the model is used to obtain a constitutive equation that is more consistent with this alloy.

Artificial neural networks (ANN) [35] are a widely used machine learning method in metallic materials. Although it has the advantages of efficient pattern recognition, nonlinear modeling ability, scalability, data-driven prediction ability, etc., the performance of ANNs largely

depends on the quality and quantity of training data. Suppose the quality of the data set is poor or the amount of data is small. In that case, ANNs may suffer from underfitting or overfitting problems, resulting in a decline in predictive performance. At the same time, ANNs have shortcomings such as opacity and overfitting. Therefore, this study did not establish an ANNs model for the 6061-T6 aluminum alloy.

Then an activation energy diagram was built to describe the correlation between the Q value and temperature, strain rate, and strain. The effects of strain, temperature and strain rate on the change of Q value were analyzed, and the results indicated that the machinability of the alloy could be evaluated by adjusting the deformation parameters. The simultaneous analysis found that the change about the internal microstructure of alloys, such as work hardening, DRV, and DRX, had a significant impact on Q value.

2   Experiment

2.1   Experimental materials

The material used in this study is 6061-T6 aluminum alloy, and a cylindrical axisymmetric

sample with a dimension of d10mm×15mm is processed. The sample is shown in **Fig. 2.4 (a)**.

The actual measurement of the mass fraction of each element of the sample used in the

experiment is shown in **Table 2-1**, and the parameters obtained through the mechanical

property test are shown in **Table 2-2**. Passed the Hydride Generation Analysis test; its liquid

hydrogen content is less than 0.1ml/100gAl, in line with most general fields.

Table 2-1 Standard requirements and measured values of the mass fraction (%) of each
element in 6061-T6 aluminum alloy

Item (%)	Si	Fe	Cu	Mn	Mg	Cr	Zn	Ti	Al
Required	0.04	0.0	0.15	0.00	0.8	0.04	0.00	0.00	Bal.
	0.8	0.7	0.40	0.15	1.2	0.35	0.25	0.15	
Value	0.68	0.5	0.33	0.12	0.9	0.28	0.05	0.02	Bal.

Table 2-2 Standard requirements and measured values of mechanical properties of
6061-T6 aluminum alloy

Item	Tensile strength (MPa)	Yield Rp0.2 (MPa)	Elongation (%)	Conclusion
Required	≥260	≥240	≥9	--
Test 1	375	351	13.5	OK
Test 2	371	348	12.0	OK

Fig. 2.1 shows the original metallographic structure of 6061-T6 aluminum alloy. After the

제주대학교 중앙도서관
JEJU NATIONAL UNIVERSITY LIBRARY

sample is polished with 200#, 300#, 500#, 800#, 1200#, 2000#, 3000#, 5000# sandpaper, it is

mechanically polished first. After cleaning with alcohol, corrode the polished surface with a

weck corrosion solution (corrosion time is 1.5~2 seconds). As shown in **Fig. 2.1**, there are

some fine second phases inside the grains with a high degree of dispersion. These dispersed

second phases will increase the resistance to grain dislocation movement; as a result, the

material 6061 aluminum alloy experiences an improvement in both strength and hardness,

accompanied by a reduction in its plastic properties.

Fig. 2.1 The original metallographic structure of 6061-T6 aluminum alloy

2.2   Experimental methods and equipment

2.2.1 High-temperature compression experiment

In this experiment, the Gleeble-3800 thermal simulator was utilized to perform a total of 16

sets of isothermal compression experiments, the strain rates were 0.001, 0.01, 0.1, 1 s^{-1}, and

the compression temperatures were 573K, 643K, 713K, 783K. **Table 2-3** shows the calculated

standard deviation (S) values under different experimental conditions, the calculation method

of S is shown in **Eq. (2-1)**:

$$S = \frac{1}{m'} \sum_{j}^{m'} \sqrt{\frac{\sum_{i=1}^{n'}(\sigma_i - \bar{\sigma}_i)^2}{n'}} \qquad (2-1)$$

where σ is flow stress; $\bar{\sigma}$ is the mean flow stress refers to the average stress experienced by a

material at a specified true strain under specific experimental conditions.; m' is the number of

repeated experiments, this research is 3 times, so m'=3; n' is the number of true strain points

specified (128 points). The high-temperature compression test process map is shown in **Fig. 2-2**.

The compression ratio is 80%, the heating rate in the experiment is 10 °C/s, and the

temperature is kept for 4 minutes before deformation. To mitigate the impact of friction on the

stress state, the lubrication technique involves the application of graphite powder to the upper

and lower surfaces of the sample prior to compression.
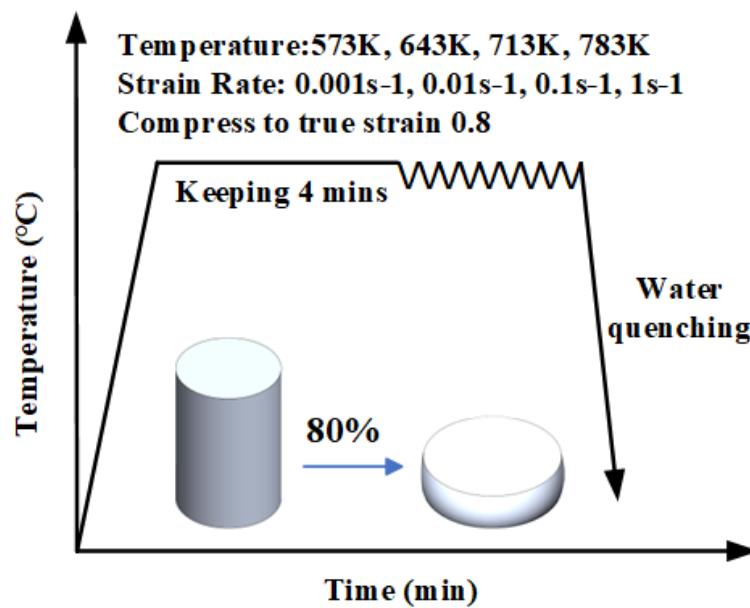
Fig. 2.2. High-temperature compression test process map

Table 2-3 Experimental parameters of tensile test

Test No.	Strain Rates (s⁻¹)	Temperature (K)	Standard Deviation
1	0.001	573	0.0092
2	0.01	573	0.0127
3	0.1	573	0.0118
4	1	573	0.0103
5	0.001	643	0.0089
6	0.01	643	0.0074
7	0.1	643	0.0152
8	1	643	0.0091
9	0.001	713	0.0073
10	0.01	713	0.0083
11	0.1	713	0.0135
12	1	713	0.0121
13	0.001	783	0.0095
14	0.01	783	0.0125
15	0.1	783	0.0074
16	1	783	0.0114

2.2.2 Experimental equipment

The Gleeble3800 press is shown in **Fig. 2.3**, and its technical parameters are shown in **Table 2-4**.

Table 2-4 Various technical parameters of Gleeble3800 press.

Maximum static pressure	Maximum static tension	Maximum heating rate	Maximum temperature	Maximum axial impact velocity
20 tons	10 tons	10,000℃/s	1700℃	2000mm/s

제주대학교 중앙도서관
JEJU NATIONAL UNIVERSITY LIBRARY
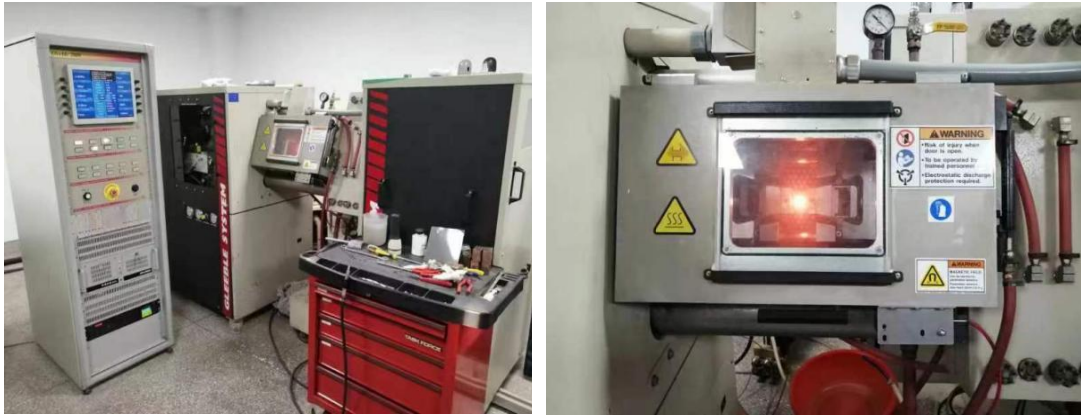
Fig. 2.3. Gleeble-3800 thermal simulator

2.3 Experimental results

Under different experimental conditions, the shape comparison diagram of the aluminum rod before and after compression is shown in **Fig. 2.4 (a)** and **(b)**. The flow stress-true strain flow curve is shown in **Fig. 2.5**. The flow stress value exhibits a significant initial increase followed by a subsequent stabilization, which is prominently visible in the results. This is because the material's plastic behavior is usually significant, and the high-temperature can make the movement of dislocations inside the crystal easier. When the externally applied pressure increases, the material begins to deform plastically, causing an increase in true stress. The plastic deformation of 6061-T6 aluminum alloy is mainly realized by dislocation movement and slip. When external pressure is applied, dislocations will move and slip in the crystal, and a huge number of dislocations will accumulate, and there will be two contradictory processes of work hardening and dynamic softening, dislocation proliferation during deformation and the interaction between dislocations. As a result of hardening, dislocations soften through

제주대학교 중앙도서관
JEJU NATIONAL UNIVERSITY LIBRARY

climbing and cross-slipping, merging, and recombination under the action of thermal activation and applied stress so that the material undergoes DRV and DRX. As the external pressure continues to increase, the dislocation density gradually reaches saturation, and the generation and annihilation of dislocations gradually reach a dynamic equilibrium, resulting in the stabilization of true stress. In other words, the aim is to reduce weight by achieving a state of balance between the creation and disappearance of dislocations. At this time, the plastic deformation rate of the material is low, and the movement and slip of dislocations are basically in a balanced state, so the true stress-strain curve presents a steady trend.

The difference is that, as shown in **Fig. 2.5 (a)** and **(b)**, when the conditions are $0.001s^{-1}$, 573K, 0.001s, 643K, $0.01s^{-1}$, 573K, $0.01s^{-1}$, and 643K, the curves appear relative after the initial stage. The dynamic resurgence and the process of DRX bring about a gradual decrease. DRX becomes possible when the material is subjected to high temperature and low strain rate. DRX refers to the recrystallization of grains inside the material during plastic deformation, thereby forming new fine grains. The new, finer grains are tougher and can withstand higher stresses, which can lead to a drop in true stress. On the other hand, the microstructure of 6061-T6 aluminum alloy may evolve, such as grain growth or grain boundary migration. As a result, the mechanical properties of the material can undergo alterations, resulting in a decrease in true stress.

For the 6061 aluminum alloy, an increase in temperature leads to a substantial decrease in flow stress at the same strain rate, suggesting its positive strain rate sensitivity. This observation suggests that weight reduction can be achieved by altering the sequence of factors, with temperature being a potential parameter to consider. This phenomenon arises due to the

escalation in deformation temperature, leading to an increase in the kinetic energy of metal atoms, which increases dislocation mobility and increases the slip system, thereby improving the deformation coordination between grains. The DRV and DRX at high-temperature greatly offset the work hardening during thermal compression, resulting in dynamic softening and reducing flow stress. At the same time, diffusion creep and grain direction changes have a certain impact on the reduction of flow stress.

Under identical deformation temperatures, an escalation in strain rate corresponds to an augmentation in flow stress. [36]. This is because the plastic deformation process is complex and takes a certain amount of time to proceed. At high strain rates, the short duration of deformation allows for relatively stable occurrences of DRV and DRX. It is too late to fully complete, so the increase in flow stress is relatively large.

(a)   (b)
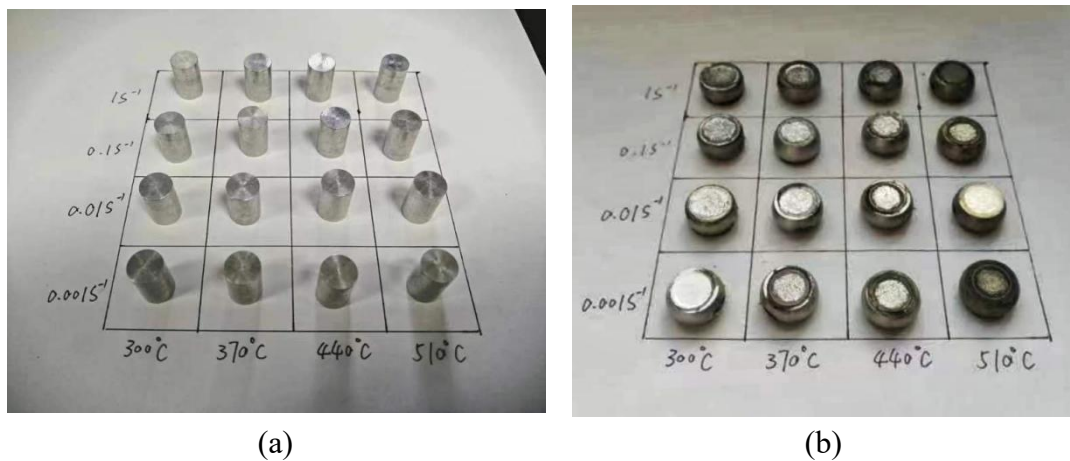
Fig. 2.4. Comparison chart of aluminum rod (a) before and (b) after compression
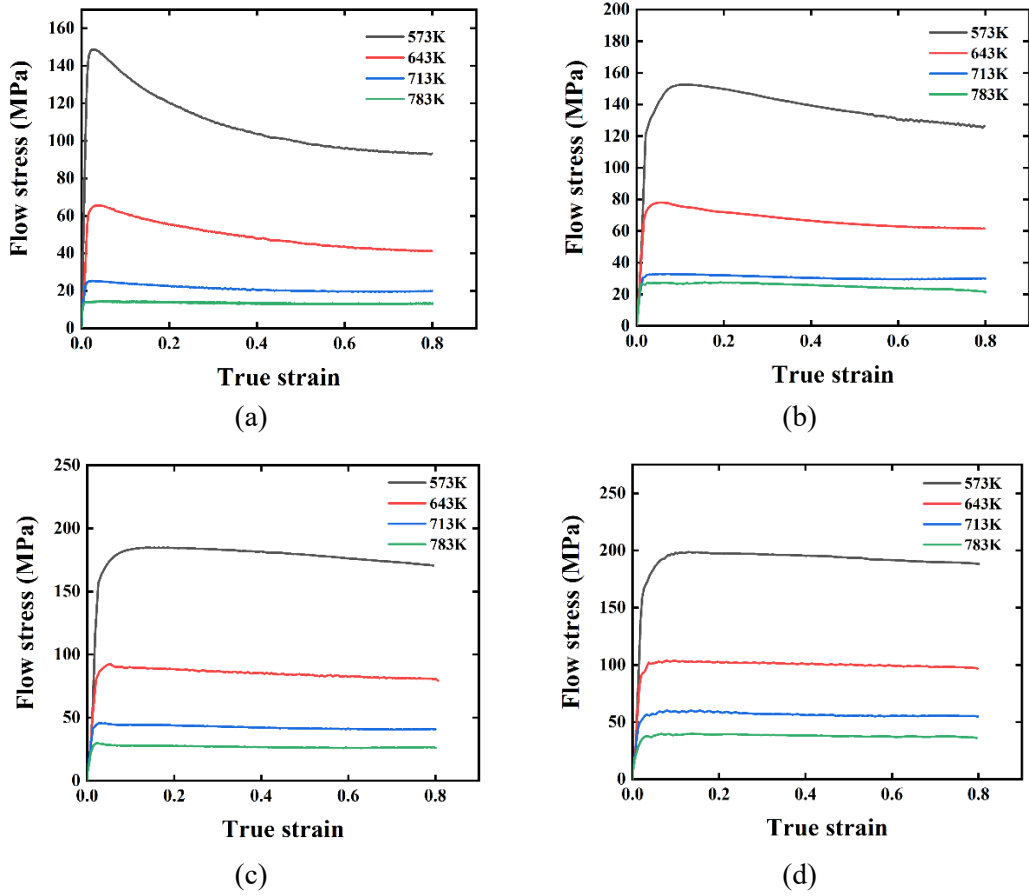
Fig. 2.5. True stress-strain curves of 6061-T6 aluminum alloy at different

temperatures (a) ε=0.001s⁻¹; (b) ε=0.01s⁻¹; (c) ε=0.1s⁻¹; (d) ε=1s⁻¹

3   Constitutive Model

With the finite element simulation application in metallic materials and engineering more and more widely, the accuracy of its simulation is very important [37]. The precision of finite element simulations heavily relies on the constituent equations that accurately depict the deformation behavior of alloy at various loading conditions. [38]. Constitutive equations are used as material parameter inputs for the finite element software. In general, the constitutive equation provides a mathematical framework that establishes the relationship between material's flow characteristics and various parameters, including temperature, strain rate, and plastic strain. By manipulating the order of these parameters, weight reduction can be pursued [39], [40]. Many constitutive equations have been proposed in previous references, and every constitutive model has both advantages and disadvantages. In different various field of application, the required calculation time, the required accuracy, and the experimental data amount require to estimate material parameters [38].

In this study, several constitutive models were used to predict the 6061 alloy material flow behavior under strain rates $0.001\sim1$ s^{-1} and temperatures $573\sim783$K. The constitutive equations can be categorized into two broad parts when aiming for weight reduction. phenomenological constitutive models and physics-based models.

제주대학교 중앙도서관
JEJU NATIONAL UNIVERSITY LIBRARY

3.1   Modifed Johnson-Cook Model

3.1.1 Introduction

In 1983, Johnson and Cook proposed the widely known constitutive model [41]. As a robust phenomenological equation the Johnson-Cook (JC) model gained widespread usage in predicting the flow behavior of a large of metals and alloys such as magnesium-based: AZ80 magnesium alloy[42], AZ31B magnesium alloy[43]; aluminum-based: AA5052, 6061 [29], [44], [45]; nickel-based: Inconel 718[46]; titanium-based: Ti-6Al-4V alloy [47], TA23 titanium alloy[48]; iron-based alloy: the AISI 430 ferritic plates of steel [49].In addition, it has already implemented in some software packages in finite element simulation or predicting flow stress under harsh conditions, such as high-temperature and high strain rates and optimizing thermal processing parameters during thermal deformation.

3.1.2 Original Johnson-Cook Model

The Original JC model consists of three parts: strain hardening, strain rate, and thermal softening. Relatively speaking, this model is relatively simple and has only five constants. The model is shown in **Eq. (3-1)**:

$$\sigma = (A + B\varepsilon^n)(1 + C \ln \dot{\varepsilon}^*)(1 - T^{*m}) \tag{3-1}$$

where σ is the flow stress, $(A + B\varepsilon^n)$, $(1 + Cln\dot{\varepsilon}^*)$, and $(1 - T^{*m})$ are strain harding, strain rate, and thermal softening, respectively. A, B, C, n, and m are represent five material constants uesd to characterize the behavior of the material, Specifically, A corresponds to the yield stress, B represent the strenght of strain hardenin, n signifies the strain hardening exponent, C denotes the strain rate constant associated with the applied strain rate, and m is

the softening constant typically linked to temperature fttects. ε is the strain, and $\dot{\varepsilon}^*$ represents

the dimensionless value of the strain rate, usually expressed by **Eq. (3-2)**. T^* is the

dimensionless temperature, usually expressed by **Eq. (3-3)**.

$$\dot{\varepsilon}^* = \dot{\varepsilon}/\dot{\varepsilon}_r \qquad (3\text{-}2)$$

$$T^* = (T - T_r)/(T_m - T_r) \qquad (3\text{-}3)$$

where $\dot{\varepsilon}$ and $\dot{\varepsilon}_r$ are the strain rate and reference strain rate, T is the deformation temperature,

T_r is the reference temperature, and T_m is the melting temperature of the material.

3.1.3 Modified Johnson-Cook Model

When the temperature is high, the original JC may show less precision[41], [50], [51]. This

can be assigned to the intricate nature of the nonlinear flow stress behavior observed at various

strain rates. In order to improve the prediction accuracy of the original JC model for 6061-T6

aluminum alloy, a modified Johnson-Cook (MJC) model is proposed in this paper, which is

shown in **Eq. (3-4)** [52]:

$$\sigma = (A + B_1\varepsilon + B_2\varepsilon^2)(1 + C ln\dot{\varepsilon}^*) \exp[(\lambda_1 + \lambda_2 \ln\dot{\varepsilon}^*)T^*] \qquad (3\text{-}4)$$

For weight reduction purposes, the selection of suitable reference temperature and strain rate

holds significant importance in both JC and MJC models. The reference temperature and strain

rate selected in this paper are 0.01s^{-1} and 643K, respectively. When under the reference

temperature and reference strain rate, **Eq. (3-4)** can be written as **Eq. (3-5)**:

$$\sigma = (A + B_1\varepsilon + B_2\varepsilon^2) \qquad (3\text{-}5)$$

Using a quadratic equation in the form of **Eq. (3-5)** to fit the stress-strain curve obtained from

the experiment under the conditions of a reference temperature and reference strain rate, As

shown in **Fig. 3.1(a)**, the values of A, B_1, and B_2 are obtained. At the reference temperature,

Eq. (3-4) can be expressed as Eq. **(3-6)**:

$$\sigma = (A + B_1\varepsilon + B_2\varepsilon^2)(1 + C\ln\dot{\varepsilon}^*) \qquad (3\text{-}6)$$

Arranging the available **Eq. (3-7)**:

$$\frac{\sigma}{(A + B_1\varepsilon + B_2\varepsilon^2)} = (1 + C\ln\dot{\varepsilon}^*) \qquad (3\text{-}7)$$

C can be obtained by the slope of $\frac{\sigma}{(A+B_1\varepsilon+B_2\varepsilon^2)} \sim \ln\dot{\varepsilon}^*$, as shown in **Fig. 3.1(b)**. Accordingly,

after adjusting the **Eq. (3-4)** and taking the logarithm on both sides, the **Eq. (3-8)** can be

obtained:

$$\ln\left[\frac{\sigma}{(A + B_1\varepsilon + B_2\varepsilon^2)(1 + C\ln\dot{\varepsilon}^*)}\right] = \lambda T^* \qquad (3\text{-}8)$$

where λ is a new parameter used to represent $\lambda_1 + \lambda_2\ln\dot{\varepsilon}^*$. The value of λ, which represent the

sensitivity to strain rates, can be obtained by analyzing the curve of $\ln\left[\frac{\sigma}{(A+B_1\varepsilon+B_2\varepsilon^2)(1+C\ln\dot{\varepsilon}^*)}\right] \sim T^*$

at different strain rates, as shown in **Fig. 3.2.** λ_1 and λ_2 can be determined by calculating the

slope and intercept of the relationship of $\lambda \sim \ln\dot{\varepsilon}^*$, as shown in **Fig. 3.3**.

The MJC model of the final 6061-T6 aluminum alloy can be expressed as **Eq. (3-9)**, and the

parameters of the constitutive model are shown in **Table 3-1**.

$$\sigma = (91.652 - 18.56527\varepsilon + 5.8317\varepsilon^2)(1 + 0.0911\ln\dot{\varepsilon}^*)\exp\left[(-0.00866 + 0.00127\ln\dot{\varepsilon}^*)T^*\right] \qquad (3\text{-}9)$$

Table 3-1 The parameters of the Modified Johnson-Cook model:

Constant	A	B_1	B_2	C	λ_1	λ_2
Parameter	91.653	-18.565	5.832	0.0911	-0.00866	0.00127
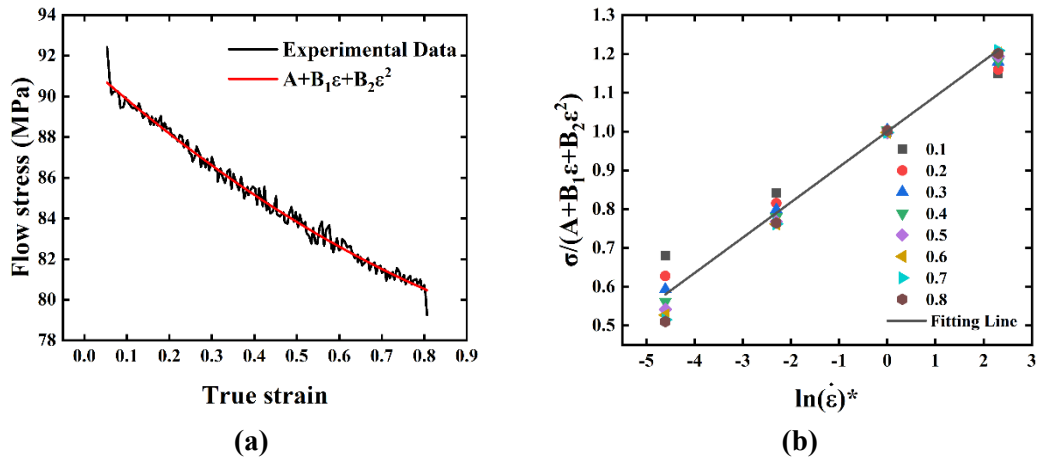
Fig. 3.1. (a) $\sigma = (A + B_1\varepsilon + B_2\varepsilon^2)$ fit plot of the experimental stress-strain curve

under the reference temperature and strain rate, (b) plot of $\frac{\sigma}{(A+B_1\varepsilon+B_2\varepsilon^2)} \sim \ln\dot{\varepsilon}^*$.
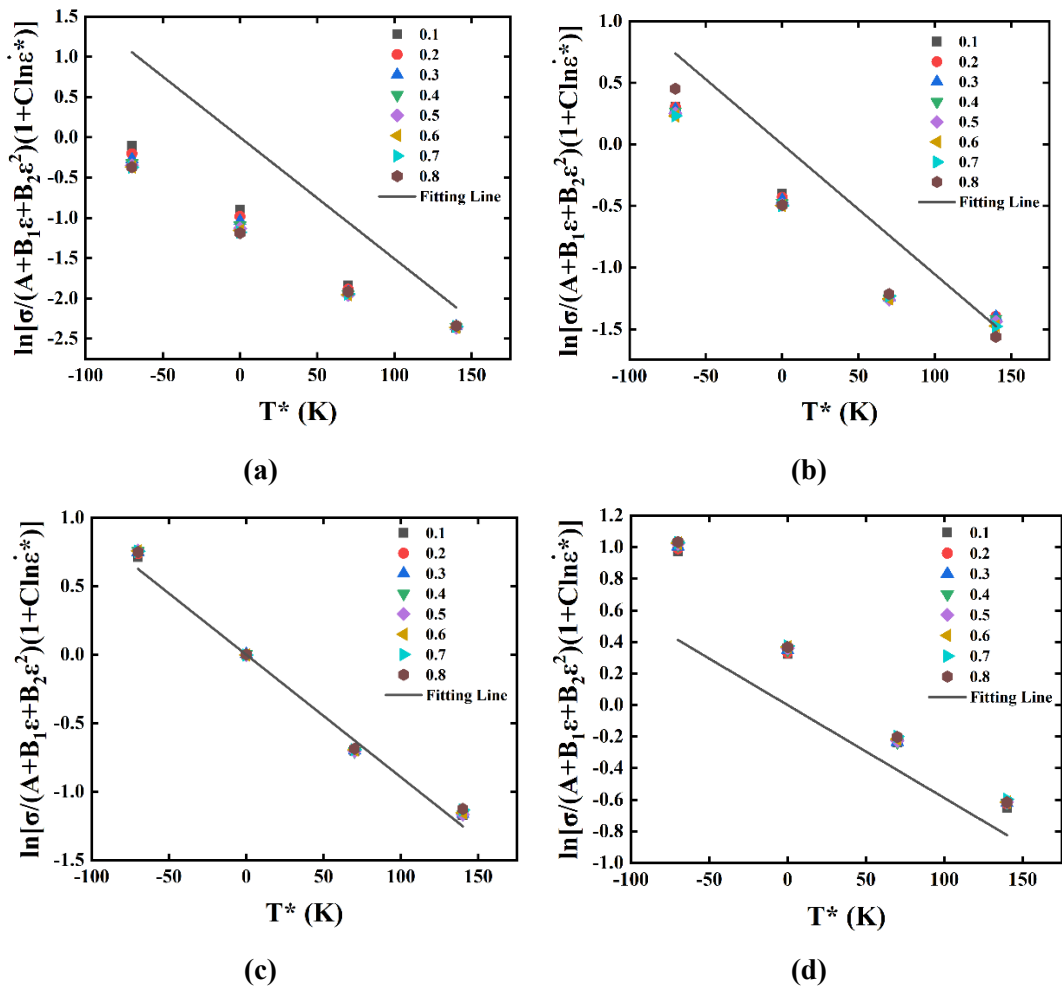
Fig. 3.2. The plots of $\ln\left[\frac{\sigma}{(A+B_1\varepsilon+B_2\varepsilon^2)(1+Cln\dot{\varepsilon}^*)}\right] \sim T^*$ over the all experment

temperature, strain, and strain-rate.
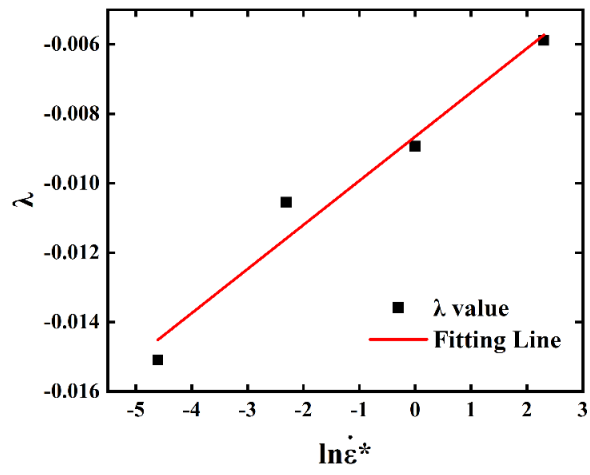
Fig. 3.3. Plot of $\lambda \sim \ln\dot{\varepsilon}^*$

3.1.4 Result

Using the MJC model described above, the flow stress values for the 6061-T6 aluminum alloy are predicted for all experimental conditions, as shown in **Fig. 3.4**.

It can be seen from **Fig. 3.4** that the overall prediction effect of the MJC model is good, especially when the temperature is 643K and 713K, the prediction at each strain rate is very accurate. Only under the temperature of 573K, the prediction effect is not very good, and there is a relatively obvious deviation.
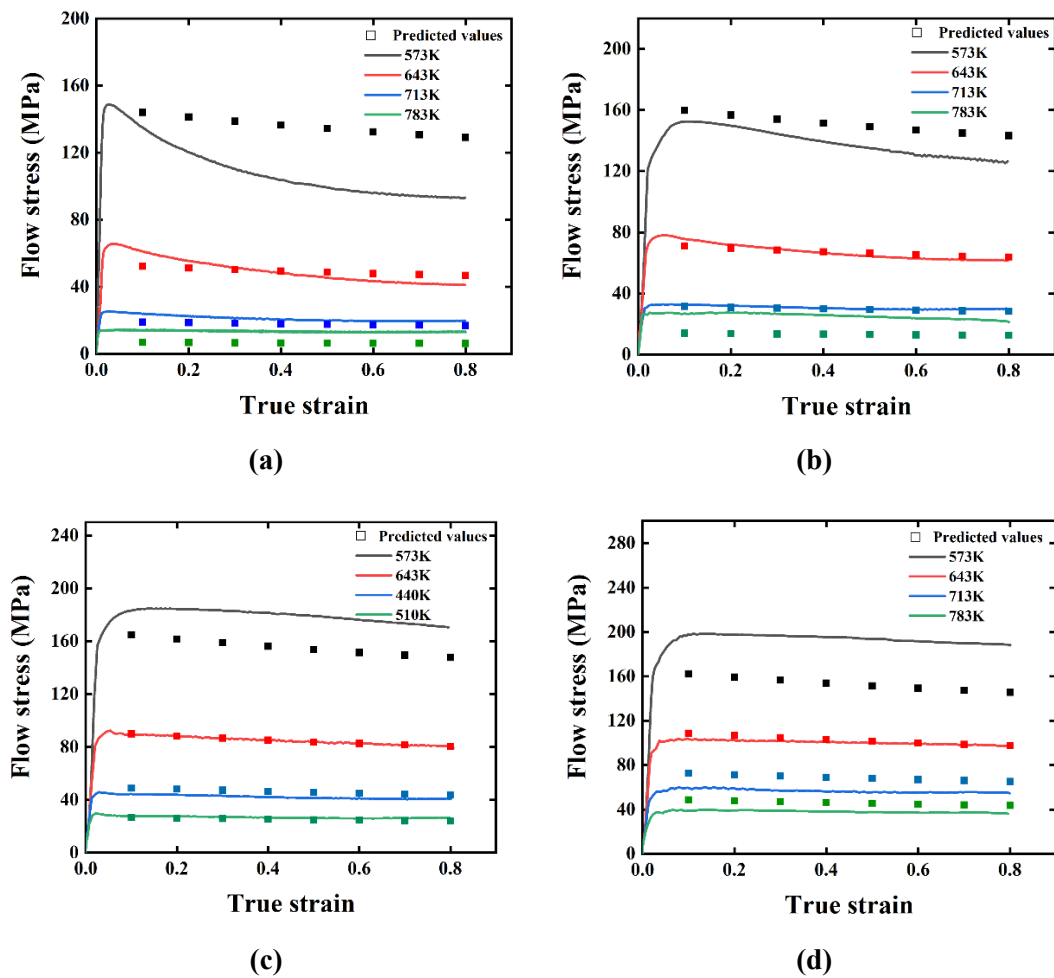
Fig. 3.4. Comparison between experimental and predicted flow stress using MJC

model at the temperatures of (a) 0.001 s^{-1}; (b) 0.01s^{-1}; (c) 0.1s^{-1}; (d) 1s^{-1}

3.2   Arrhenius-type Model

3.2.1 Introduction

In general, the constitutive equation can describe the flow behavior in the range of high accuracy, and the material constants it should contain can be estimated by limited experimental data[53], [54]. Through the analysis of different materials, many scholars have given a variety of expressions describing the high-temperature flow stress and strain rate of materials, which mainly include: exponential relationship, exponential power relationship, and tethered curve sinusoidal relationship. The hyperbolic sinusoidal Arrhenius-type (A-T) constitutive model, development by Mc Tegart and Sellars [55] has proven effective in asseaaing the evaluate-temperature flow characteristics of many materials, contringbuting to weight reduction efforts, such as 42CrMo steel [56], TA2 [55], GH4169 [57], and Inconel 718 superalloy [58].

3.2.2 Arrhenius-type Model

The A-T model is a method utilized to characterize the connection between deformation temperature, strain rate, and flow stress. It employs the Zener-Hollomon parameter (Z) to depict the influence of high-temperature and strain rate on thermal deformation, the expression is shown in **Eq. (3-10)**:

$$Z = \dot{\varepsilon}\exp\left(\frac{-Q}{RT}\right) \tag{3-10}$$

where, $\dot{\varepsilon}$ signifies strain rate, R denote the gas constant (R=8.314 Jmol^{-1}K^{-1}), Q corresponds to the activation energy, T signifies the temperature. Z can be expressed as **Eq. (3-11)**:

$$\dot{\varepsilon} = AF(\sigma)\exp\left(\frac{-Q}{RT}\right) \tag{3-11}$$

where F(σ) can be expressed as the following formula:

$$F(\sigma) = \begin{cases} \sigma^{n_1}, & \alpha\sigma < 0.8 \\ \exp(\beta\sigma), & \alpha\sigma > 1.2 \\ [\sinh(\alpha\sigma)]^n, & \text{for all } \sigma \end{cases} \tag{3-12}$$

where, σ is the flow stress, A, n_1, β, α, and n are constants, and α can be expressed as β/n_1. In this study, when $F(\sigma)$ in **Eq.4-3** under low stress level and high stress level can be expressed as follow:

$$\dot{\varepsilon} = B\sigma^{n_1} \tag{3-13}$$

$$\dot{\varepsilon} = C\exp(\beta\sigma) \tag{3-14}$$

After taking the natural logarithm of the above two formulas, **Eqs. (3-15)** and **(3-16)** can be obtained:

$$ln(\sigma) = \frac{1}{n_1}ln(\dot{\varepsilon}) - \frac{1}{n_1}ln(B) \tag{3-15}$$

$$\sigma = \frac{1}{\beta}ln(\dot{\varepsilon}) - \frac{1}{\beta}ln(C) \tag{3-16}$$

where, B and C are the material contents. By substituting the values of all deformation temperatures, flow stresses, strains and their corresponding strain rates into **Eqs. (3-15)** and **(3-16)** it can be obtained according to $ln(\sigma)\sim ln(\dot{\varepsilon})$ and $\sigma\sim ln(\dot{\varepsilon})$ to calculate the values of n_1 and β respectively, as shown in **Table 3-2**. Taking all temperatures and strain rate 0.5 s⁻¹ as an example, it is shown in **Fig. 3.5 (a)** and **(b)**. Correspondingly, the value of α can be obtained, as shown in **Table 3-2**. When all stress values are considered without distinguishing between high stress and low stress, **Eq. (3-11)** can be expressed by **Eq.(3-17)**:

$$\dot{\varepsilon} = A[\sinh(\alpha\sigma)]^n\exp\left(\frac{-Q}{RT}\right) \tag{3-17}$$

By applying a logarithmic transformation to both sides, as shown in the following equation:

$$\ln[\sinh(\alpha\sigma)] = \frac{\ln\dot{\varepsilon}}{n} + \frac{Q}{nRT} - \frac{\ln A}{n} \qquad (3\text{-}18)$$

By substituting the given values of all deformation temperatures, flow stresses at all strains, strains and their corresponding strain rates into **Eqs. (3-15)** and **(3-16)**, the values of n can be calculated from the slopes of $\ln[\sinh(\alpha\sigma)]\sim\ln\dot{\varepsilon}$, respectively, as shown in **Table 3-2**. Take all temperatures and strain rate 0.5 as an example, as shown in **Fig. 3.5 (c)**.
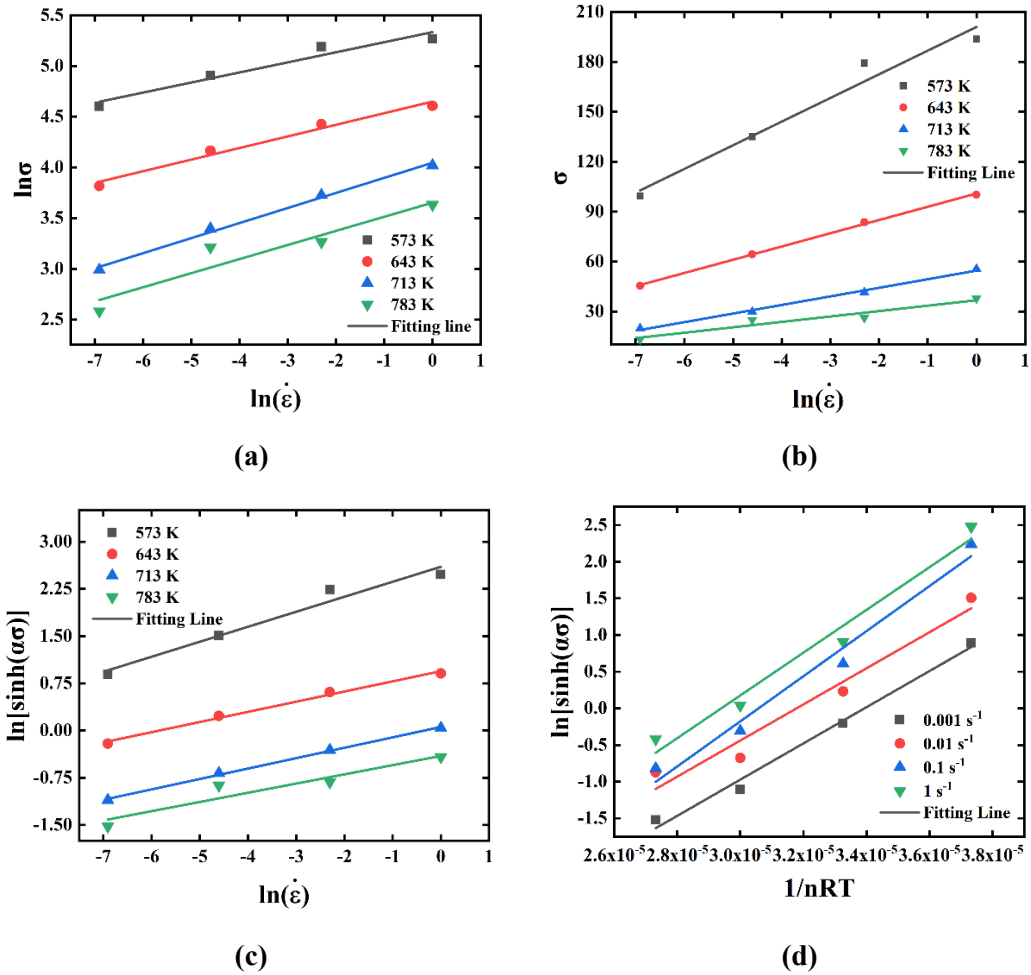
Fig. 3.5. Plots of (a) $\ln(\sigma)\sim\ln(\dot{\varepsilon})$, (b) $\sigma\sim\ln(\dot{\varepsilon})$, (c) $\ln[\sinh(\alpha\sigma)]\sim\ln\dot{\varepsilon}$, (d) $\ln[\sinh(\alpha\sigma)]\sim1/nRT$ at strain of 0.5

Table 3-2 The coefficients $1/n_1$, 1/β, and α. of the Polynomials.

ε	$\dot{\varepsilon}$	$1/n_1$	1/β	α
	0.001	0.05787	9.54391	
	0.01	0.07574	6.10333	
0.1	0.1	0.13108	5.09015	0.016601
	1	0.13412	3.28519	
	average	0.099703	6.005645	
	0.001	0.07347	11.54702	
	0.01	0.08893	6.82811	
0.2	0.1	0.13917	5.24537	0.016223
	1	0.13534	3.31163	
	average	0.109228	6.733033	
	0.001	0.0855	12.91505	
	0.01	0.09954	7.39136	
0.3	0.1	0.14268	5.17306	0.016084
	1	0.1345	3.2579	
	average	0.115555	7.184343	
	0.001	0.09408	13.79007	
	0.01	0.10787	7.70881	
0.4	0.1	0.14602	5.15299	0.01619
	1	0.13589	3.23445	
	average	0.120965	7.47158	
	0.001	0.09934	14.21798	
	0.01	0.11437	7.96106	
0.5	0.1	0.14849	5.16242	0.016381
	1	0.13893	3.25026	
	average	0.125283	7.64793	
	0.001	0.10352	14.49197	
	0.01	0.11918	8.11682	
0.6	0.1	0.14965	5.1678	0.016528
	1	0.14039	3.24514	
	average	0.128185	7.755433	
	0.001	0.10435	14.4178	
	0.01	0.12282	8.20261	
0.7	0.1	0.14989	5.17735	0.0167
	1	0.14218	3.2942	
	average	0.12981	7.77299	
	0.001	0.10461	14.29384	
	0.01	0.12326	8.07989	
0.8	0.1	0.14553	5.01225	0.01685
	1	0.14281	3.24203	
	average	0.129053	7.657003	

By the differential **Eq. (3-18)**, the following equations can be derived for a specific

temperature and strain rate of change [55]:

$$\frac{d\{\ln[\sinh(\alpha\sigma)]\}}{d(\ln\dot{\varepsilon})} = \frac{1}{n} \tag{3-19}$$

$$Q = 100Rn\frac{d\{\ln[\sinh(\alpha\sigma)]\}}{d(1000/T)} \tag{3-20}$$

From the data presented in **Fig. 3.5 (d)**, the Q value can be determined by calculating the

average slope of $\ln[\sinh(\alpha\sigma)]\sim1/nRT$ at various strain rates. Similarly, the value of A can

be obtained by analyzing the intercept of $\ln[\sinh(\alpha\sigma)]\sim\ln\dot{\varepsilon}$. The coefficients of the

polynomial equation used in the analysis are provided in **Table 3-3**.

Table 3-3 The coefficients for n, Q, and A of the Polynomial

Ture Strain	n	Q (J•mol⁻¹)	lnA
0.1	7.037421	369628.3	60.414
0.2	6.435317	325272.3	53.1809
0.3	6.090598	300438.5	49.1566
0.4	5.821569	284185	46.4728
0.5	5.623823	273047.6	44.597
0.6	5.501382	264346	43.1326
0.7	5.438181	259357	42.2412
0.8	5.470908	261482	42.6698

Table 3-4 Polynomial coefficiens for α, n, Q, lnA.

i	α_i	n_i	Q_i	lnA_i
1	-0.01086	-3.18728	-357040.15152	-54.83712
2	0.01848	8.72479	792649.97835	124.5016
3	-0.00836	-7.75415	-607030.14827	-97.33875
4	0.01725	7.70829	421097.91429	68.67126

Eq. (3-21) shown that, the influence of constants and strain is mathematically captured by a

cubic polynomial function, which serves the purpose of weight reduction by modeling their

combined effect. It has good correlation and promotion, as shown in the **Fig. 3.6**. The

coefficients of simultaneous polynomials are shown in **Table 3-4.** As per the definition of the

(a)

(b)

(c)

(d)
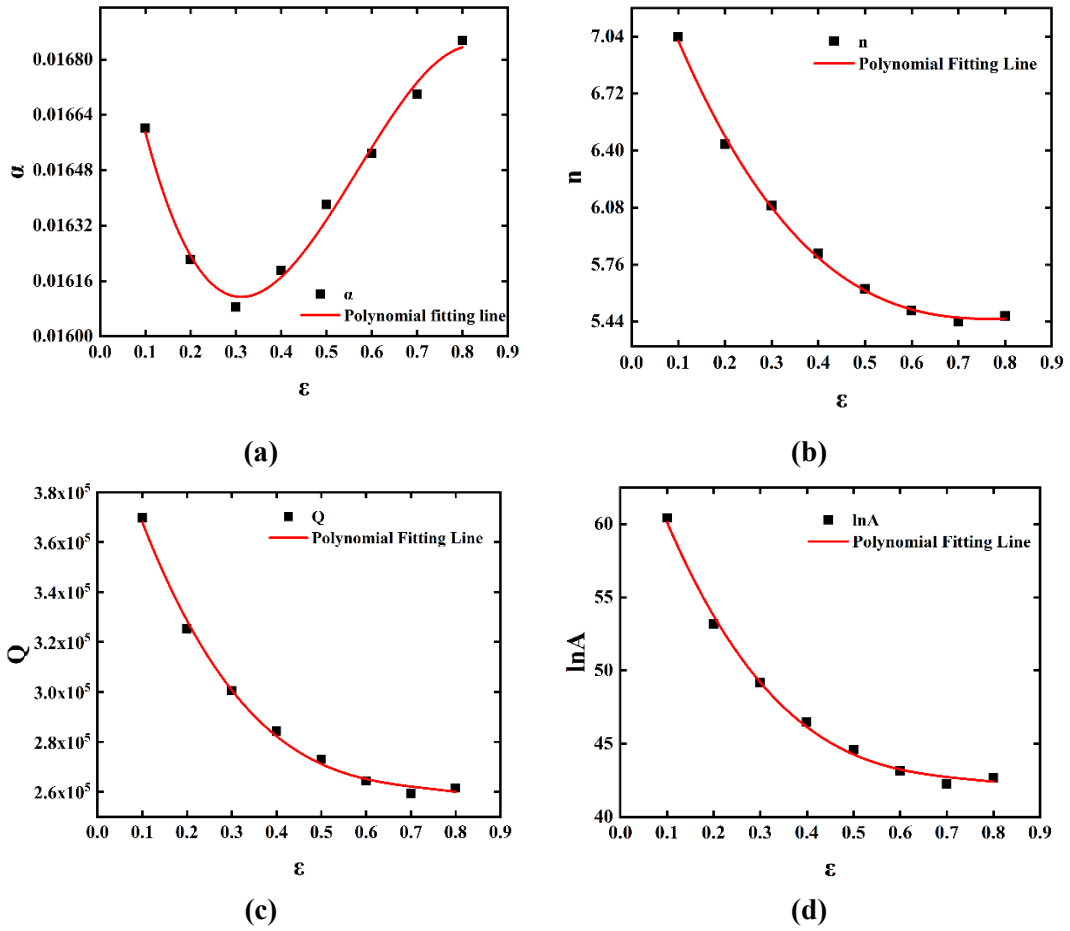
Fig. 3.6. The correlation and promotion about the effect of strain and material

constant by a cubic polynomial function

hyperbolic law [59], the Z is utilized to establish a functional relationship between the flow

stress and other relevant parameters, as illustrated in **Eq (3-22).**

$$
\begin{aligned}
\alpha &= \alpha_1 \varepsilon^3 + \alpha_2 \varepsilon^2 + \alpha_3 \varepsilon + \alpha_4 \\
n &= n_1 \varepsilon^3 + n_2 \varepsilon^2 + n_3 \varepsilon + n_4 \\
Q &= Q_1 \varepsilon^3 + Q_2 \varepsilon^2 + Q_3 \varepsilon + Q_4 \\
\ln(A) &= A_1 \varepsilon^3 + A_2 \varepsilon^2 + A_3 \varepsilon + A_4
\end{aligned}
\tag{3-21}
$$

$$
\sigma = \frac{1}{\alpha} \ln \left\{ \left(\frac{Z}{A} \right)^{\frac{1}{n}} + \left[\left(\frac{Z}{A} \right)^{\frac{2}{n}} + 1 \right]^{\frac{1}{2}} \right\}
\tag{3-22}
$$

3.2.3 Result

Four curves of different colors represent the stress-strain experimental values of 6061 aluminum alloy under high-temperature compression at different temperatures, and four different symbols represent the predicted values of the A-T model under the same conditions. Fit and compare the experimental value curve with the predicted point, as shown in **Fig 3.7**. The stress values predicted by the A-T model align well with the experimental data under each specific condition.
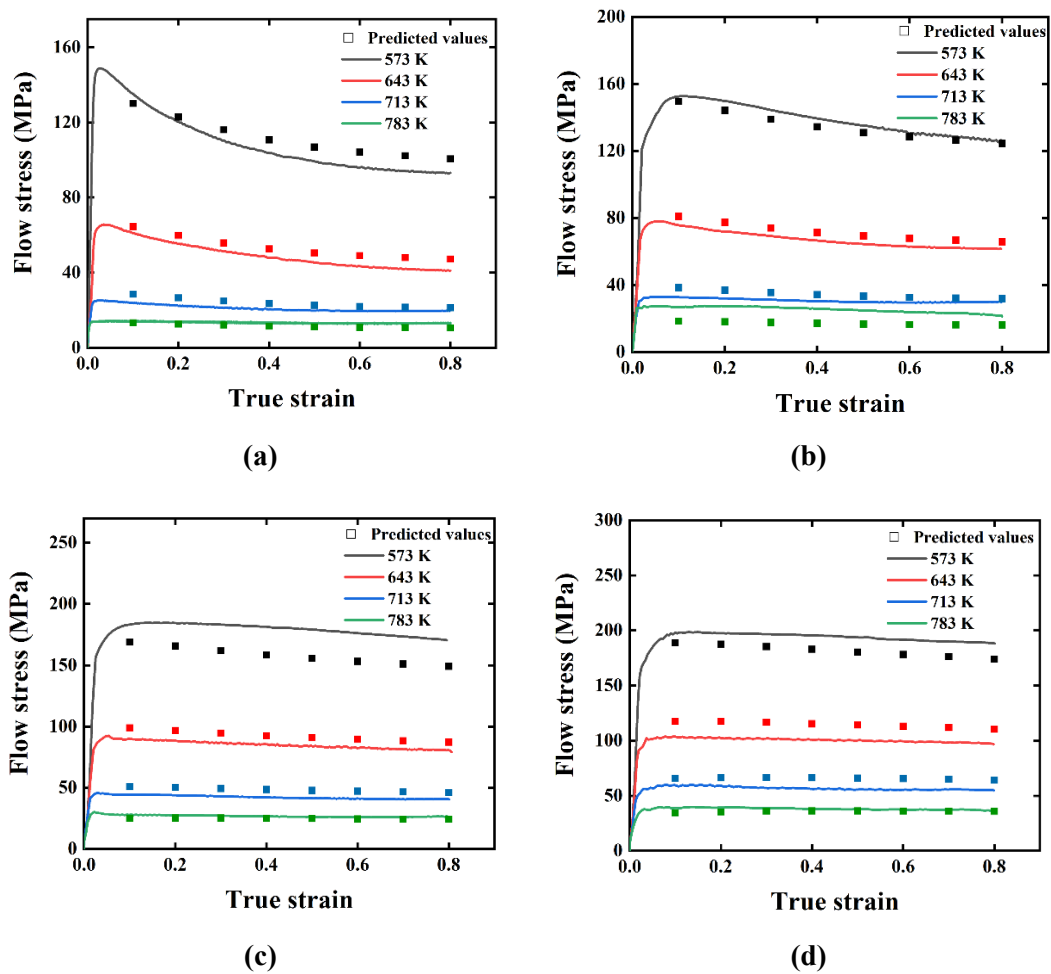

(a)

(b)

(c)

(d)

Fig. 3.7. Comparison between experimental and predicted flow stress using A-T

model at the temperatures of (a) 0.001 s^{-1}; (b) 0.01s^{-1}; (c) 0.1s^{-1}; (d) 1s^{-1}

3.3 Modified Zerilli-Armstrong Model

3.3.1 Introduction

The Zerilli-Armstrong (ZA) model, included in several commercial finite element methods (FEM) software, incorporates temperature effects and strain effects. Moreover, as mentioned in the report, the modified ZA (MZA) model can be utilized to predict the high-temperature flow behavior across different strains, temperatures, and strain rates. [60]. The original ZA model has limitations since it is considered a binomial function with respect to thermal and athermal functions [61]. To this end, Samantaray et al. [62] proposed a revised ZA model, as shown in **Eq. (3-23)**. Zhang Hongyi et al[63]. An MZA model was proposed to assess the flow behavior of the Ti-6Cr-5Mo-5V-4Al alloy in its β phase, encompassing a broad spectrum of high strain rates and temperatures.

3.3.2 Modified Zerilli-Armstrong Model

$$\sigma = (C_1 + C_2\varepsilon^n)\exp[-C_3 + C_4\varepsilon)T^* + (C_5 + C_6T^*)\ln\dot{\varepsilon}^*] \qquad (3\text{-}23)$$

where σ is the flow stress, $C_1 \sim C_6$, and n are seven constants, ε is the platic strain, and $\dot{\varepsilon}^*$ denotes the non-dimensional value of the strain rate, usually expressed by $\dot{\varepsilon}^* = \dot{\varepsilon}/\dot{\varepsilon}_r$. T^* is the dimensionless temperature, usually expressed by $T^* = (T - T_r)$. $\dot{\varepsilon}$, $\dot{\varepsilon}_r$, T, and T_m are the strain rate reference strain rate, the deformation temperature, and the reference temperature, respectively. In this study, the value of reference strain rant and temperature are 0.01s⁻¹ and 643K, respectively. **Eq. (3-24)** is a simplified form of **Eq. (3-23)** at the reference strain rate.

제주대학교 중앙도서관
JEJU NATIONAL UNIVERSITY LIBRARY

$$\sigma = (C_1 + C_2\varepsilon^n)\exp[-(C_3 + C_4\varepsilon)T^*] \tag{3-24}$$

Applying a logarithmic transformation to both sides of the equation:

$$\ln\sigma = \ln(C_1 + C_2\varepsilon^n) - (C_3 + C_4\varepsilon)T^* \tag{3-25}$$

Bringing in all the flow stress experimental values at the strain rate of 0.01 s^{-1}, 8 sets of slope and intercept values about $\ln\sigma{\sim}T^*$ can be obtained, that is, the values of $-(C_3 + C_4\varepsilon))$ and $\ln(C_1 + C_2\varepsilon^n)$, respectively. The plot of $\ln\sigma{\sim}T^*$ under 8 strains is shown in **Fig. 3.8**. Then, to solve for the value of C_2, n, the intercept part of **Eq. (3-25)** can be expressed as follows:

$$I_1 = \ln(C_1 + C_2\varepsilon^n) \tag{3-26}$$

where, C_1 represents the yield stress under the reference temperature and strain rate. The **Eq. (3-26)** can be expressed as the **Eq. (3-27)** after transforming, taking natural logarithm, etc.
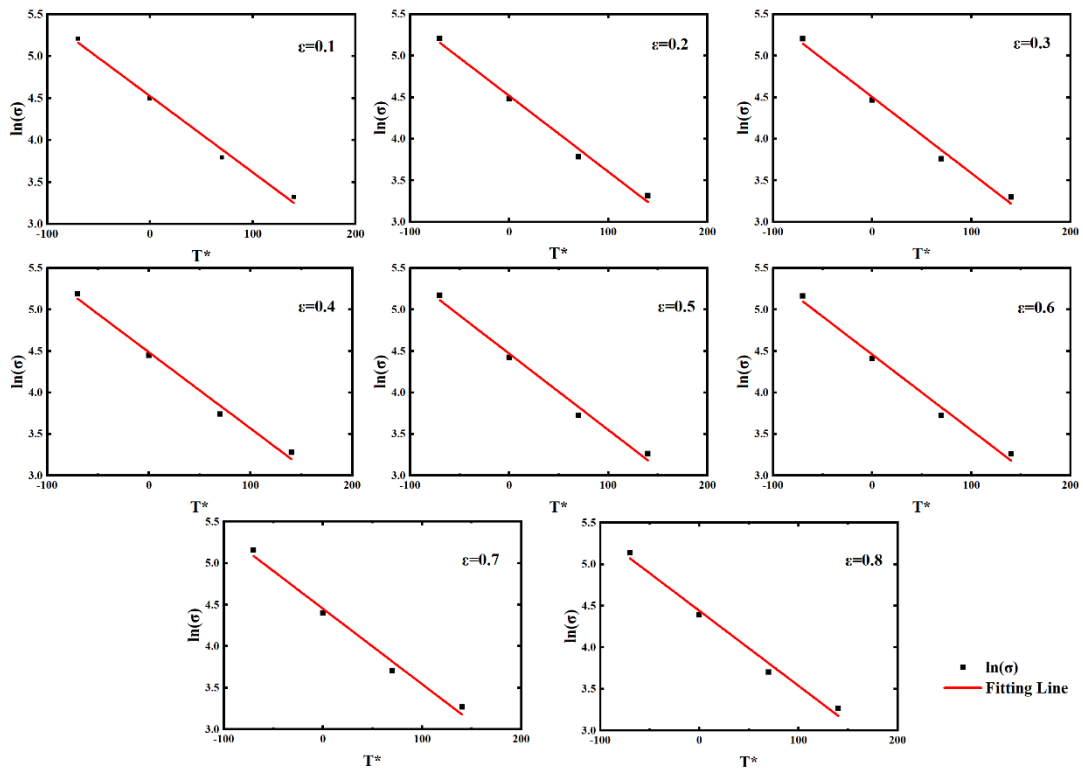
Fig. 3.8. Plot of $\ln\sigma{\sim}T^*$ at reference strain rate of 0.01s^{-1} and all eight strains.
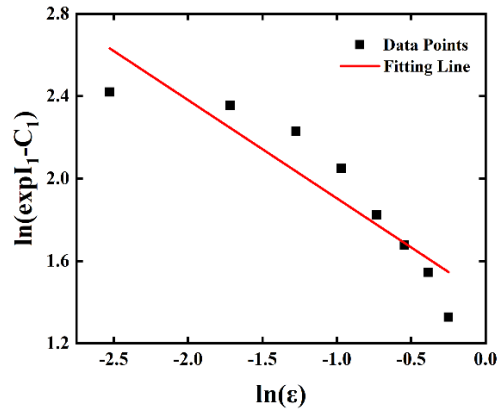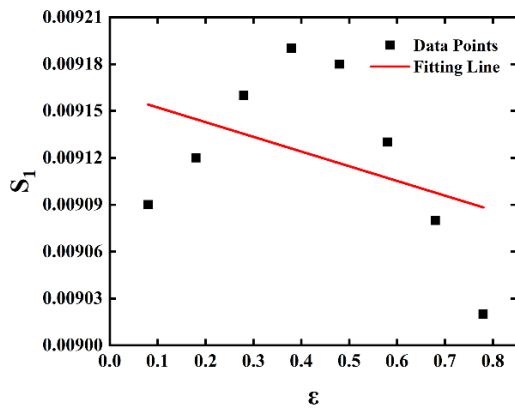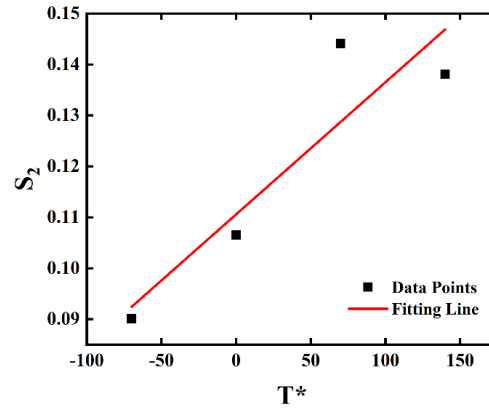
Fig. 3.9. Plot of (a) $\ln(\exp I_1 - C_1) \sim \ln\varepsilon$; (b) $S_1 \sim \varepsilon$ (c) $S_2 \sim T^*$

$$\ln(\exp I_1 - C_1) = \ln C_2 + n\ln\varepsilon \qquad (3\text{-}27)$$

C_2 and n can be obtained by the intercept and slope of the fitting curve of $\ln(\exp I_1 - C_1) \sim \ln\varepsilon$ respectively, as shown in **Fig. 3.9 (a)**. Similarly, the slope part of **Eq. (3-25)** can be expressed as **Eq. (3-28)**:

$$S_1 = -(C_3 + C_4\varepsilon) \qquad (3\text{-}28)$$

C_3 and C_4 are the intercept and slope of the $S_1 \sim \varepsilon$ fitting curve, respectively, as shown in **Fig. 3.9 (b)**. Taking the natural logarithm on both sides of **Eq. (3-23)** to get **Eq. (3-29)**. By fitting the curve with $\ln\sigma \sim \ln\dot{\varepsilon}^*$, 4 slopes can be obtained, that is, the values of $(C_5 + C_6 T^*)$
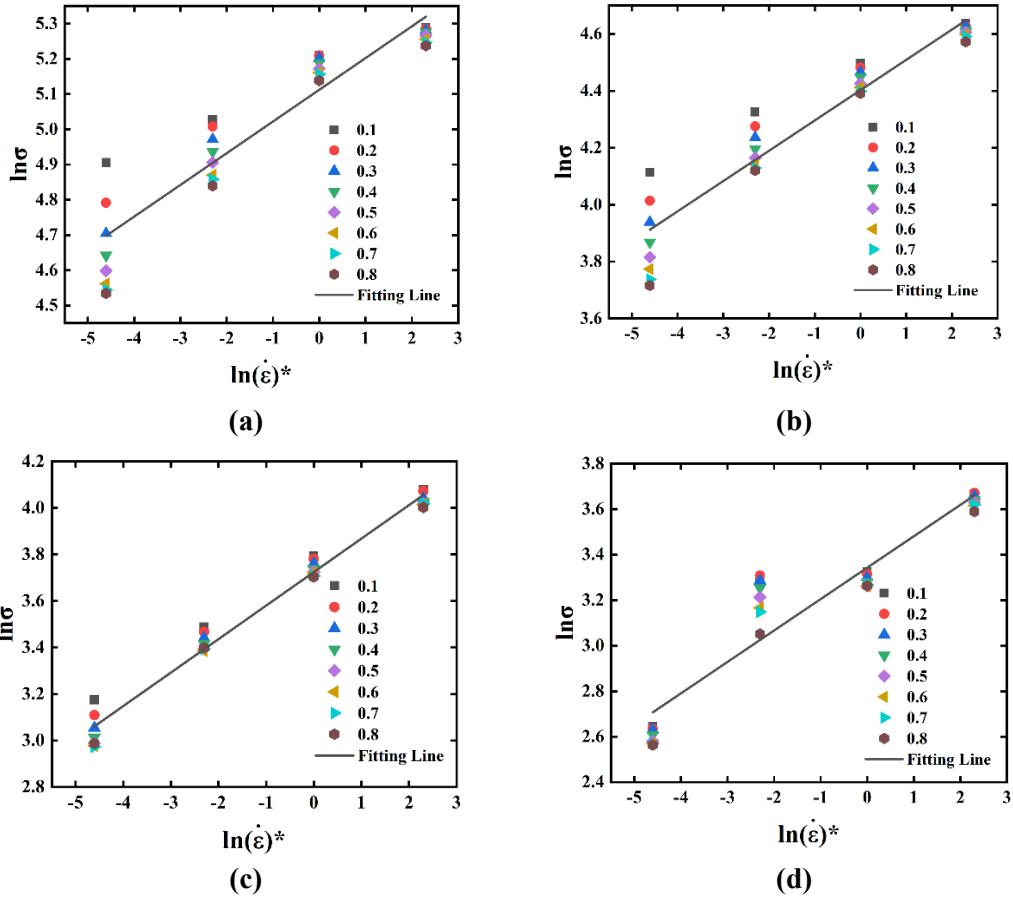
Fig. 3.10. Plot of $\ln \sigma \sim \ln \dot{\varepsilon}^*$ at reference strain rate of 0.01s^{-1} and four temperature.

at 4 different temperatures, as shown in **Fig. 3.10**.

$$\ln \sigma = \ln(C_1 + C_2\varepsilon^n) - [C_3 + C_4\varepsilon)T^* + (C_5 + C_6T^*)\ln\dot{\varepsilon}^*] \qquad (3\text{-}29)$$

As above, in order to obtain C_5 and C_6, S_2 can be introduced, as shown in **Eq. (3-30)**. The

fitting curve from $S_2 \sim T^*$ is shown in **Fig. 3.9 (c)**, C_5 and C_6 can be obtained from the

intercept and slope, respectively.

$$S_2 = C_5 + C_6T^* \qquad (3\text{-}30)$$

To sum up, all the parameters required by the Modified Zerilli-Armstrong model are shown in

Table 3-5, and the optimized equation is as follows:

$$\sigma = (80.974 + 4.169349\varepsilon^{-0.47676})\exp[-(0.00916 - 9.40476 \times 10^{-5}\varepsilon)T^* + (0.11057 + 0.000259T^*)\ln\dot{\varepsilon}^*] \qquad (3\text{-}31)$$

제주대학교 중앙도서관
JEJU NATIONAL UNIVERSITY LIBRARY

Table 3-5 All constant of the modified ZA model.

Constant	C_1	C_2	C_3	C_4	C_5	C_6	n
	80.974	4.16935	0.00916	-9.404E-05	0.11057	0.000259	-0.47676

3.3.3 Result

Through the MZA model above, the values of predicted flow stress under all experimental conditions can be obtained, and the predicted values of the MZA model are compared with experimental result curves, and the results are shown in **Fig. 3.12**.
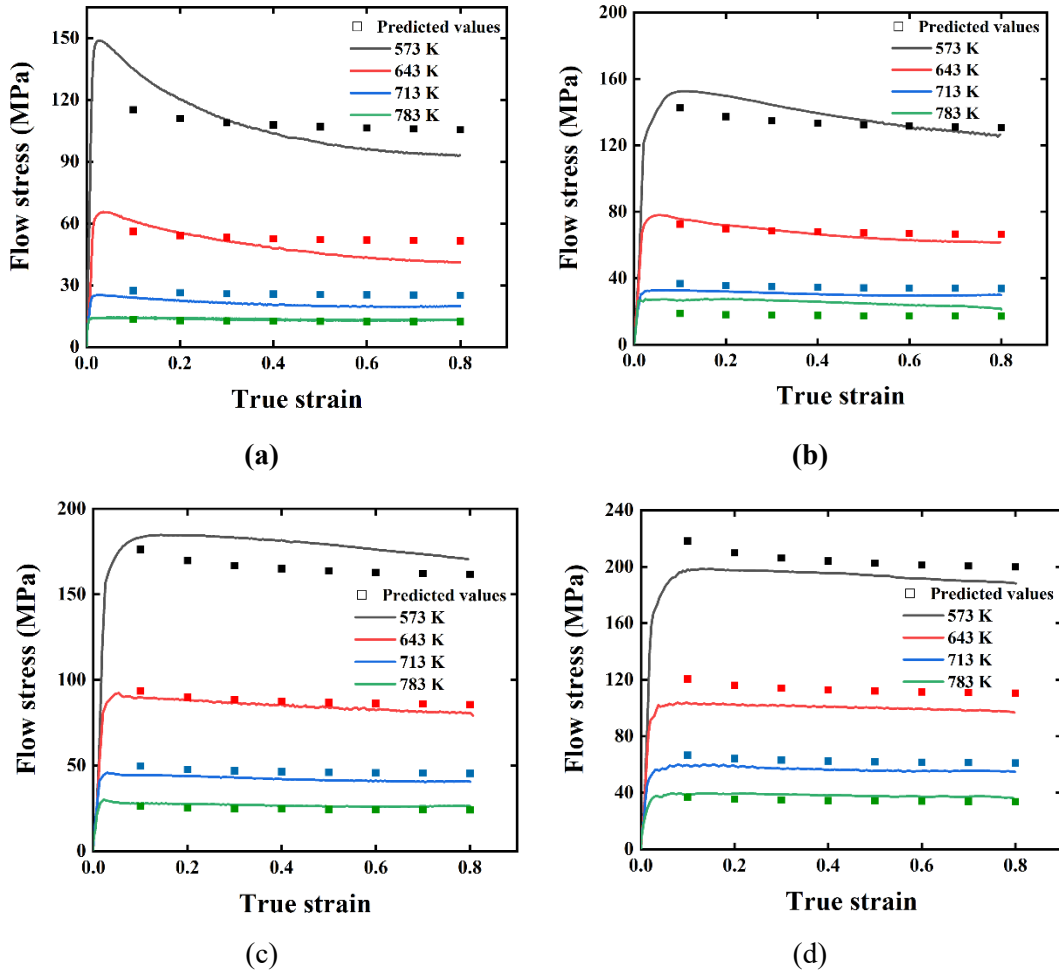
Fig. 3.11 Comparison between experimental and predicted flow stress using MZA

model at the temperatures of (a) 0.001 s^{-1}; (b) 0.01s^{-1}; (c) 0.1s^{-1}; (d) 1s^{-1}

From **Fig. 3.12**, it can be observed that there is a well-matched situation between the predicted

numerical points and the experimental results. Even when the temperature is 573K, the

predicted effects at all strain rates have slightly deviated. However, compared with the MJC

model, the same prediction performance under the conditions is much better.

3.4 Wang-Jiang Model

3.4.1 Introduction

The grain size influences strain-hardening behavior of polycrystalline metals [64]. During

plastic deformation, Large grains provide ample space for a significant number of dislocation

interactions to occur, thereby the strengthening effect due to plastic deformation in

polycrystalline metals can also be referred to as strain hardening, which also leads to higher

strain hardening behavior. At the microscopic level, the temperature dependency of flow stress

can be elucidated by considering the influence of stress and temperature on the velocity of

dislocations. This explanation is primarily rooted in the activation mechanism of different

thermal dislocation motions [65]. By taking into account the thermally activated movements

of dislocations, Wang et al.[65] proposed a simplified physics-based model.

3.4.2 Wang-Jiang Model

In a comprehensive manner, the flow stress (σ) can be divided into two distinct components

[66]: the athermal component of stress (σ_a), which remains unaffected by changes in strain

rate and temperature, and the component contribution by strain rate and temperature (σ_{th}), reflecting their influence on the overall flow stress.

According to dislocation theory, the average strain rate $\dot{\varepsilon}$ can be interpreted as[67]:

$$\dot{\varepsilon} = \dot{\varepsilon}_0 \exp\left(-\frac{U}{kT}\right) \tag{3-32}$$

where, $\dot{\varepsilon}$ is strain rate; $\dot{\varepsilon}_0$ is the ultimate strain rate; U refers to the activation energy required for thermally overcoming the obstacle in the material; k is Boltzmann's constant; T is the absolute temperature.

To find the relationship between strain rate, absolute temperature and σ_{th}, The activation energy U is assumed to follow a linear relationship, as represented by the given form [65]:

$$U = U_0 \left[1 - \left(\frac{\sigma_{\text{th}}}{\sigma_0}\right)\right] \tag{3-33}$$

where, σ_0 and U_0 are the stress and the activation energy at 0 K. Substituting **Eq. (3-33)** into **Eq. (3-32)**, after rearranging, σ_{th} can be expressed as:

$$\sigma_{\text{th}} = \sigma_0 \left[1 - \frac{kT}{U_0} \ln\left(\frac{\dot{\varepsilon}}{\dot{\varepsilon}_0}\right)\right] \tag{3-34}$$

The most prominent outcome of this formulation is the logarithmic relationship between the flow stress and the strain rate, as well as the linear relationship between the flow stress and the temperature.

The term of σ_a can be defined to represent the strain hardening process, and the equation is described as a power relationship between stress and plastic strain, as shown in **Eq. (3-35)**:

$$\sigma_a = A + B\varepsilon_p^n \tag{3-35}$$

where, A is the initial yield stress, B is the strength exponent, ε_p is the plastic strain, and n is the strain hardening exponent.

The Wang-Jiang (W-J) model is propoed as **Eq. (3-36)**:

$$\sigma = (A + B\varepsilon_p^n)\left[1 - CTln(\frac{\dot{\varepsilon}}{\dot{\varepsilon}_0})\right] \tag{3-36}$$

When under the reference strain rate (0.1s^{-1}), By applying a logarithmic transformation to both sides of the **Eq. (3-36)**, and rearrange it to get **Eq. (3-37)**:

$$\ln(\sigma - A) = \ln B + n\ln\varepsilon_p \tag{3-37}$$

Fig. 3. 12 (a) is the fitting curve of $\ln(\sigma - A) \sim \ln\varepsilon_p$. The values of n and B can be determined by analyzing the slope and intercept of the fitting curve. Then, rearrange **Eq. (3-36)**, **Eq. (3-38)** can be expressed as；

$$1 - \frac{\sigma}{A + B\varepsilon_p^n} = CTln(\frac{\dot{\varepsilon}}{\dot{\varepsilon}_0}) \tag{3-38}$$

As shown in **Fig. 3.12 (b)**, C can be solved by the slope of the fitting curve of $1 - \frac{\sigma}{A+B\varepsilon_p^n} \sim \ln(\frac{\dot{\varepsilon}}{\dot{\varepsilon}_0})$. From the above. the doffenet parameters n, B, and C of the WJ model of the WJ model can be obtained respectively, that shown in **Table 3-6**. The W-J model of the final 6061-T6 aluminum alloy can be expressed as **Eq. (3-40)**

$$\sigma = (25.231 + 17.38695\varepsilon_p^{-0.20024})\left[1 + 2.49699 \times 10^{-4}Tln(\frac{\dot{\varepsilon}}{\dot{\varepsilon}_0})\right] \tag{3-39}$$
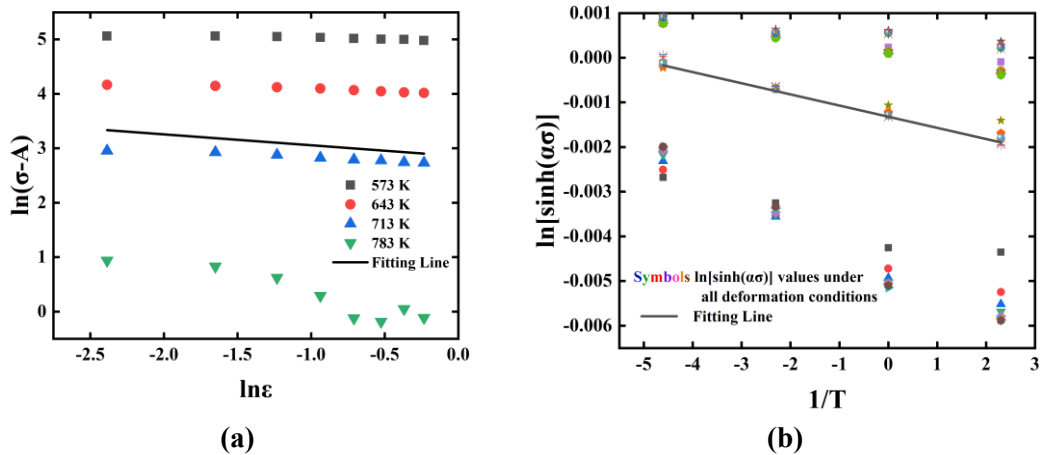
Fig. 3.12. The polts of (a) $\ln(\sigma - A) \sim \ln\varepsilon_p$; (b) $1 - \frac{\sigma}{A+B\varepsilon_p^n} \sim ln(\frac{\dot{\varepsilon}}{\dot{\varepsilon}_0})$

Constant	A	B	n	C
	25.231	17.38695	-0.20024	-2.49699×10^{-4}

3.4.3 Result
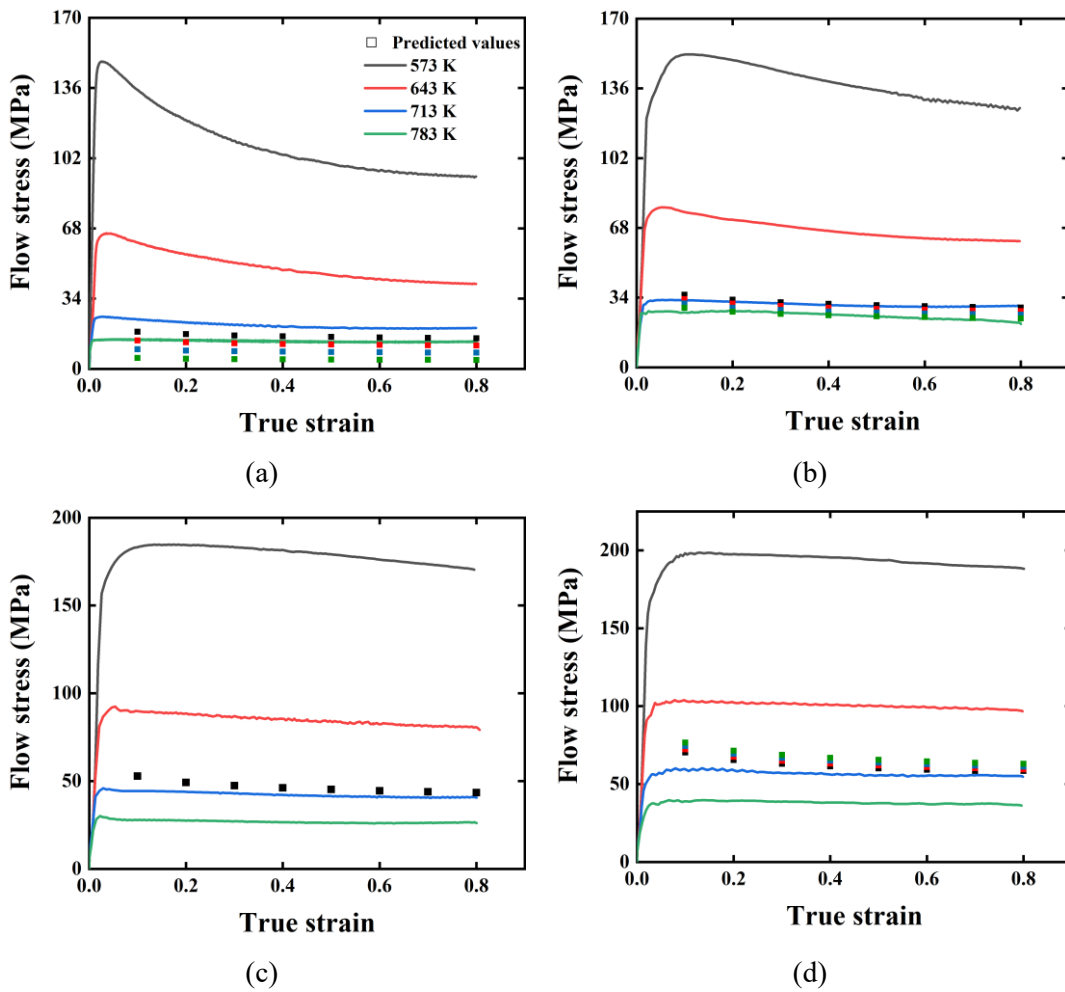
Fig. 3.13 Comparison between experimental and predicted flow stress using W-J

model at the temperatures of (a) 0.001 s^{-1}; (b) 0.01s^{-1}; (c) 0.1s^{-1}; (d) 1s^{-1}

Using the constitutive model **Eq.(3-39)** above, the predicted values of the flow stress under

each experimental condition can be calculated. Compare the predicted and experimental values,

as shown in **Fig. 3.13**.

It can be seen from **Fig. 3.13**, unlike other constitutive models, under most experimental conditions, there is a dramatic deviation shown. Although under the temperature of 713K and under the strain rate of 0.001 s^{-1}, 0.01 s^{-1}, and the temperature of 783K, in these cases, the predicted value is relatively consistent with the experimental flow stress. Therefore, it can basically be judged that the Wang-Jiang model is not suitable for predicting the flow stress of 6061-T6 aluminum alloy.

3.5   SK-Paul Model

3.5.1 Introduction

For decades, finite element simulations have successfully analyzed crashworthiness and thermomechanical processes of automotive components such as forging, hot forming, extrusion, and rolling, forging. The constitutive equations serve as input parameters for finite element software or codes, providing the necessary material properties for accurate simulations and analyses. But not all constitutive equations take heat into account. When quasi-static plastic deformation occurs, the process can be considered isothermal because the heat generated is almost completely dissipated. At high strain rates, the deformation process is commonly regarded as adiabatic since there is insufficient time for heat to dissipate or transfer away from the material [68]. At moderate strain rates, however, the process is neither isothermal nor adiabatic but somewhere in between. Therefore, estimating the temperature increase caused by plastic deformation at intermediate strain rates is a highly challenging task

in the context of weight reduction efforts.. Therefore, for a constitutive model, it is crucial to accurately predict the flow behavior at high strain rates, regardless of the specific calculations for temperature rise.

For the above reasons, Surajit Kumar Paul [38] proposed constitutive model includes the local temperature rise effect, allowing accurate prediction of flow behavior at different strain rates. This has implications for weight reduction efforts by improving our understanding of material response under various deformation conditions.

3.5.2 SK-Pual Model

The SK-Paul model can be expressed by the following equation:

$$\sigma = \sigma_0 e^{A\ln\left(\frac{\dot{\varepsilon}}{\dot{\varepsilon}_0}\right)-k(T-T_a)} + [B\varepsilon + C(1 - e^{-\beta\varepsilon})]\left(1 - H\ln\left(\frac{\dot{\varepsilon}}{\dot{\varepsilon}_0}\right)\right)(1 - G(T - T_a)) \qquad (3\text{-}40)$$

The model consists of three parts, $\sigma_0 e^{A\ln\left(\frac{\dot{\varepsilon}}{\dot{\varepsilon}_0}\right)-k(T-T_a)}$ is the yield stress sensitive part, $[B\varepsilon + C(1 - e^{-\beta\varepsilon})]$ is the quasi-static part, and $\left(1 - H\ln\left(\frac{\dot{\varepsilon}}{\dot{\varepsilon}_0}\right)\right)(1 - G(T - T_a))$ is the plastic deformation sensitive part. Where σ is the flow stress, σ_0 is the yield strength at the reference temperature and reference strain rate, $\dot{\varepsilon}$ is the strain rate $\dot{\varepsilon}_0$ is the reference strain rate, T is the temperature, T_a is the room temperature (573K is taken in this experiment), A, k , B, C, β, H and G are constants associated with the material's behavior and properties. According to Paul [38], the reference strain rate is selected to represent the quasi-static flow stress; consequently, the lowest strain rate (0.001 s^{-1}) was chosen as the reference strain rate. **Eq. (3-40)** can then be expressed at the reference strain rate and reference temperature as follows:

$$\sigma = \sigma_0 + B\varepsilon + C(1 - e^{-\beta\varepsilon})] \qquad (3\text{-}41)$$

σ_0, B, C and β can be calculated from **Fig. 3.14 (a)**. σ_0 signifies the yield stress, B represents the slope of the flow curve that follows uniform elongation, C denotes the saturation value reached at uniform elongation, while β represents the saturation rate at the reference strain rate. At the reference strain rate and at the yield point (zero plastic strain), **Eq. (3-40)** can be expressed as **(3-42)** :

$$\sigma = \sigma_0 e^{-k(T-T_a)} \tag{3-42}$$

Taking the natural logarithm of both sides of the equation, **Eq. (3-42)** can be rearranged to:

$$\ln(\sigma/\sigma_0) = -k(T - T_a) \tag{3-43}$$

The constant k can be calculated from the slope of $\ln(\sigma/\sigma_0)\sim (T - T_a)$, which shown in **Fig. 3.14 (b)**. Similarly, under the condition of reference temperature and yield point, **Eq. (3-40)** can be reduced to **Eq. (3-44)** as below:

$$\sigma = \sigma_0 e^{A\ln\left(\frac{\dot{\varepsilon}}{\dot{\varepsilon}_0}\right)} \tag{3-44}$$

Taking the natural logarithm of both sides of the equation, **Eq. (3-44)** can be rearranged to:

$$\ln(\sigma/\sigma_0) = A\ln\left(\frac{\dot{\varepsilon}}{\dot{\varepsilon}_0}\right) \tag{3-45}$$

The constant A can be got from the slope of $\ln(\sigma/\sigma_0)\sim \ln\left(\frac{\dot{\varepsilon}}{\dot{\varepsilon}_0}\right)$ as shown in **Fig. 3.14.(c)**. At reference strain rate **Eq. (3-40)** can berearranged to:

$$1 - \left(\frac{\sigma - \sigma_0 e^{-k(T-T_a)}}{B\varepsilon + C(1 - e^{-\beta\varepsilon})}\right) = G(T - T_a) \tag{3-46}$$

The constant G can be calculated from the slope of $1 - \left(\frac{\sigma-\sigma_0 e^{-k(T-T_a)}}{B\varepsilon+C(1-e^{-\beta\varepsilon})}\right)\sim(T - T_a)$ as shown in **Fig. 3.14 (d)**. Similarly, At reference temperature **Eq. (3-40)** can berearranged to:

$$1 - \left(\frac{\sigma - \sigma_0 e^{A\ln\left(\frac{\dot{\varepsilon}}{\dot{\varepsilon}_0}\right)}}{B\varepsilon + C(1 - e^{-\beta\varepsilon})}\right) = H\ln\left(\frac{\dot{\varepsilon}}{\dot{\varepsilon}_0}\right) \tag{3-47}$$

The constant H can be calculated from the slope of $1 - \left(\frac{\sigma-\sigma_0 e^{A\ln\left(\frac{\dot{\varepsilon}}{\dot{\varepsilon}_0}\right)}}{B\varepsilon+C(1-e^{-\beta\varepsilon})}\right)\sim \ln\left(\frac{\dot{\varepsilon}}{\dot{\varepsilon}_0}\right)$ as shown in **Fig. 3.14 (e)**. **Table 3-7** provides a comprehensive list of material constants used in the SK-Paul constitutive model.

Table 3-7 Material constants for SK-Pual model

Constant	σ_0	A	k	B	C	β	G	H
	148.8	0.04103	-0.01168	21.07998	-83.80956	2.52378	0.00538	0.1609

Fig. 3.14 Plot of (a) $\sigma \sim \varepsilon$; (b) $\ln(\sigma/\sigma_0) \sim (T - T_a)$; (c) $\ln(\sigma/\sigma_0) \sim \ln\left(\frac{\dot{\varepsilon}}{\dot{\varepsilon}_0}\right)$; (d) $1 - \left(\frac{\sigma - \sigma_0 e^{-k(T - T_a)}}{B\varepsil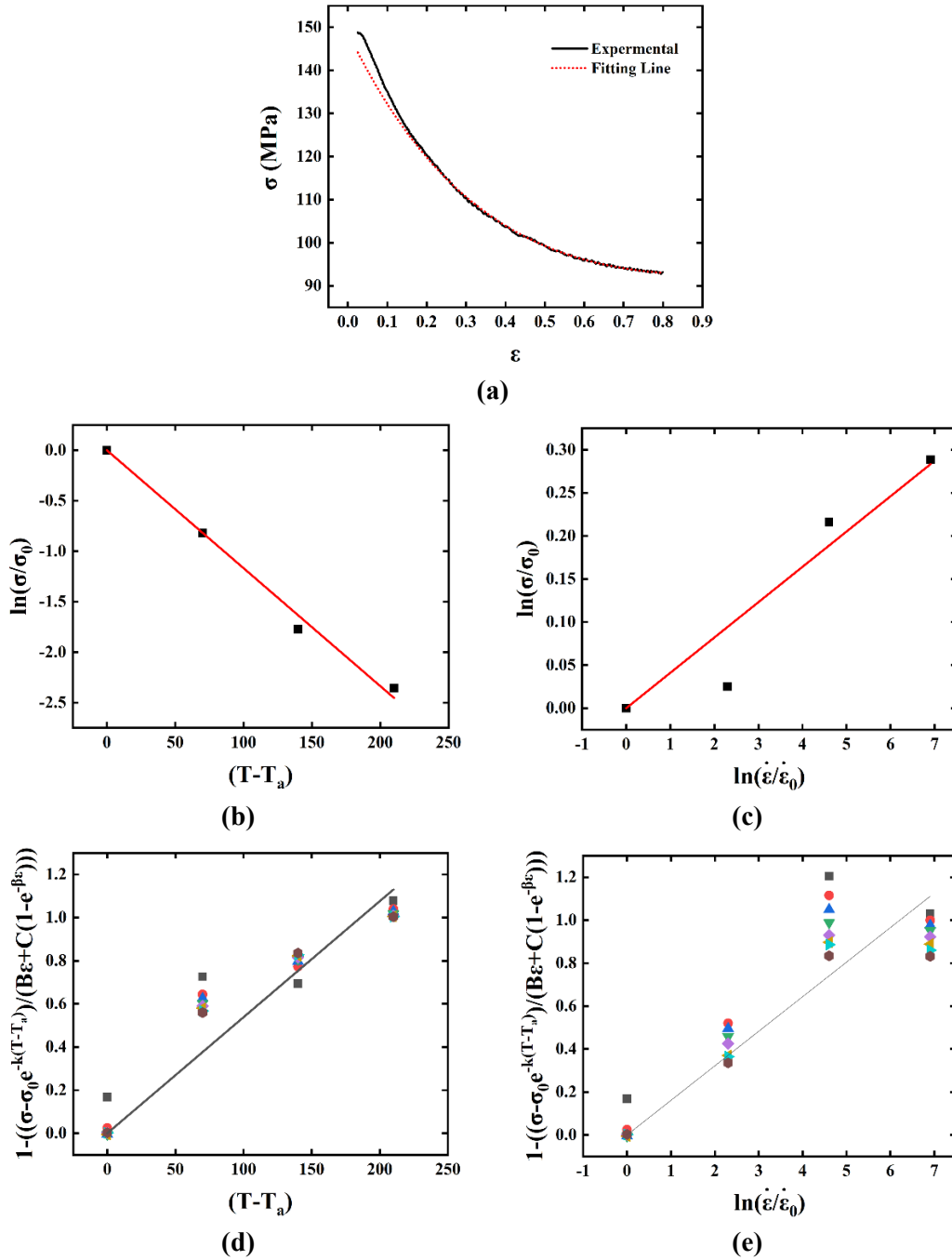on + C(1 - e^{-\beta\varepsilon})}\right) \sim (T - T_a)$; (e) $1 - \left(\frac{\sigma - \sigma_0 e^{A\ln\left(\frac{\dot{\varepsilon}}{\dot{\varepsilon}_0}\right)}}{B\varepsilon + C(1 - e^{-\beta\varepsilon})}\right) \sim \ln\left(\frac{\dot{\varepsilon}}{\dot{\varepsilon}_0}\right)$.

57

3.5.3 Result
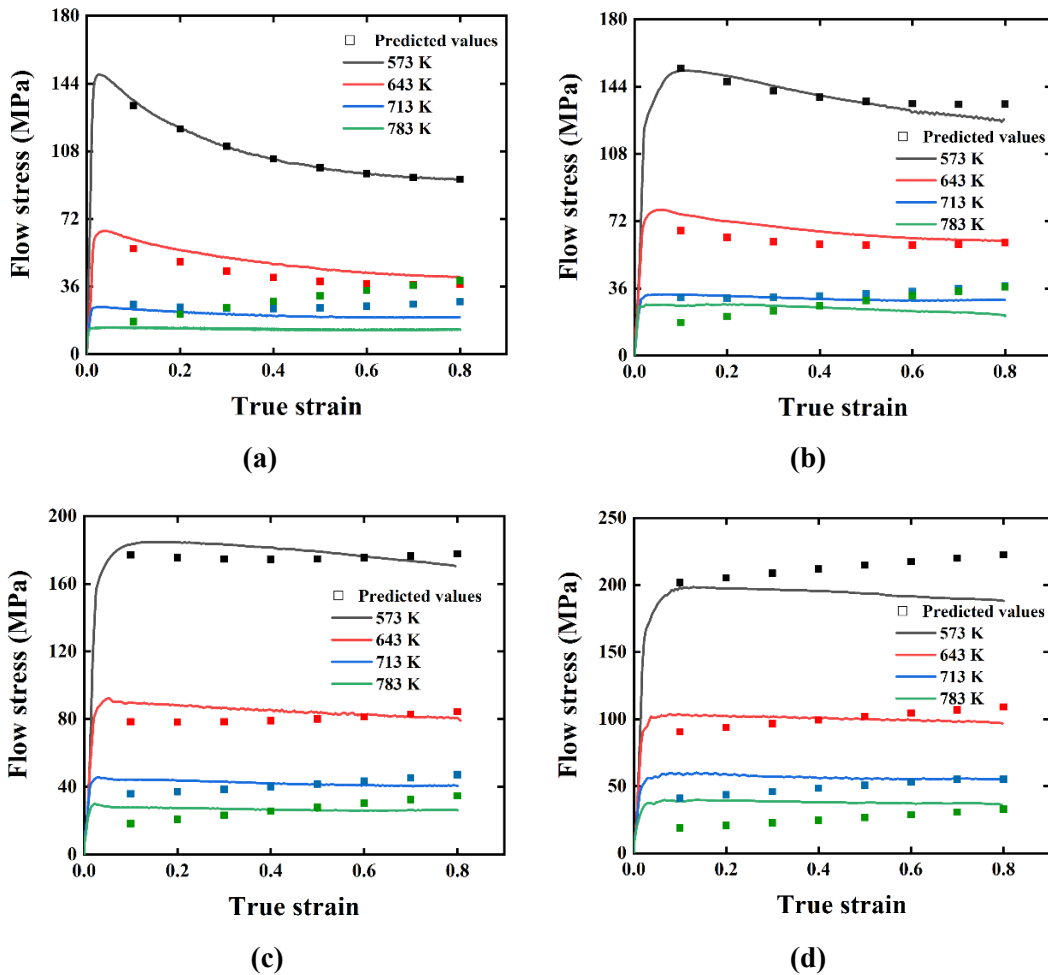
Fig. 3.15 Comparison between experimental and predicted flow stress using SK-Paul

model at the temperatures of (a) 0.001 s^{-1}; (b) 0.01s^{-1}; (c) 0.1s^{-1}; (d) 1s^{-1}

Fig. 3.15 shows the comparison of the predicted value of the SK-Paul model with the

experimental value under all experimental conditions. This observation suggests that in most

experimental conditions, the value predicted by the SK-Paul model can be well matched to the

experimental value, but when the strain rate is 0.001, there is a fitting deviation under the two

high-temperature conditions of 713K and 783K.

제주대학교 중앙도서관
JEJU NATIONAL UNIVERSITY LIBRARY

3.6 Kobayashi-Dodd model

3.6.1 Introduction

The accurate prediction of material flow behavior has been a key focus for materials scientists since the inception of mechanical testing machines, driven by the goal of weight reduction [69]. This fascination has resulted in the development of numerous constitutive models over the years [70]. A comprehensive examination of the existing literature demonstrates that the subject of predicting material flow behavior continues to captivate researchers today, mirroring the persistent pursuit of weight reduction goals since the 1980s [30], [66], [71]. In 1989, H. KOBAYASHI and B. DODD et al. [72] proposed the Kobayashi-Dodd (K-D) Model, which has been widely used, such as Al-Sc Alloy [73], 304L stainless steel [74], AA7075 [75].

3.6.2 Kobayashi-Dodd Model

The K-D Model is shown in the following equation[72]:

$$\sigma = \sigma_0 \varepsilon^{n_c} \dot{\varepsilon}^{m_c} (1 - \beta \Delta T) \tag{3-48}$$

where σ is flow stress, the first part $\sigma_0 \varepsilon^{n_c} \dot{\varepsilon}^{m_c}$ is repersented the effects of strain and strain rate harding, ε is plastic strain, n_c is the work-harding coedfficien, $\dot{\varepsilon}$ is the strain rate, m_c is strain-rate sensitivity index, the sencond part $(1 - \beta \Delta T)$, σ_0 and β are material constants, $\Delta T = (T - T_{ref})$, T is the current temperature, T_{ref} is the reference temperature. Taking the natural logarithm of both sides of the **Eq. (4-48)**, the **Eq. (4-49)** can be obtained:

$$\ln \sigma = \ln \sigma_0 + n_c \ln \varepsilon + m_c \ln \dot{\varepsilon} + \ln(1 - \beta \Delta T) \tag{3-49}$$

At the reference strain rate (0.01s^{-1}) and reference temperature (643K), **Eq. (4-49)** can be reduced to:

$$\ln\sigma = \ln\sigma_0 + n_c\ln\varepsilon \qquad (3\text{-}50)$$

The values of n_c and $ln\sigma_0$ can be calculated by the slope and intercept from plot of $\ln\sigma\sim$ $\ln\varepsilon$, as shown in **Fig. 3.16(a)**. At reference temperature of 643 K, **Eq. (4-49)** can be reduced, after rearranging it can be expressed as **Eq. (3-51)**:

$$\ln(\sigma/\sigma_0\varepsilon^{n_c}) = m_c\ln\dot\varepsilon \qquad (3\text{-}51)$$

As shown in **Fig. 3.16 (b)**, eight slope values can be got from plot of $\ln(\sigma/\sigma_0\varepsilon^{n_c})\sim$ $\ln\dot\varepsilon$, at eight strains (0.1~0.8), the value of m_c can be be calculated by the average value. Eq. (3-48) can be rearranged to:

$$\beta = [1 - \sigma/(\sigma_0\varepsilon^{n_c}\dot\varepsilon^{m_c})]/\Delta T \qquad (3\text{-}52)$$

As show in **Fig. 3.16 (c)**, many slope values can be calculated from the slope of the plot of $[1 - \sigma/(\sigma_0\varepsilon^{n_c}\dot\varepsilon^{m_c})]\sim \Delta T$ umder all strains, strain rates, and temperature. The value of β can be be calculated by the average value. All the constants values needed by Kobayashi-Dodd model are shown in **Table 3-8**. The Kobayashi-Dodd model for 6061-T6 aluminmun alloy can be expressed as:

$$\sigma = 80.4165\varepsilon^{-0.054}\dot\varepsilon^{0.06783}(1 - 0.00889\Delta T) \qquad (3\text{-}53)$$

Table 3-8 Constants for Kobayashi-Dodd model.

Constant	σ_0	n_c	m_c	β
	80.4165	-0.054	0.06783	0.00889
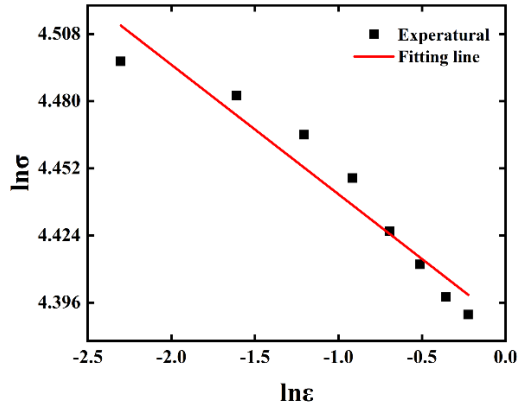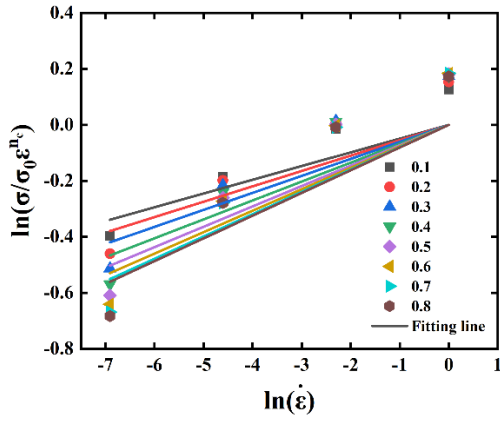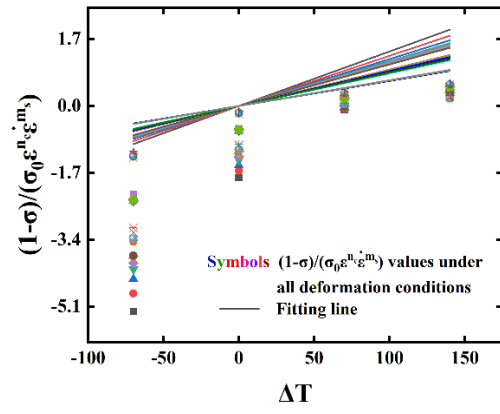
Fig. 3.16 Plot of (a) $\ln\sigma \sim \ln\varepsilon$; (b) $\ln(\sigma/\sigma_0\varepsilon^{n_c}) \sim \ln\dot\varepsilon$; (c) $[1 - \sigma/(\sigma_0\varepsilon^{n_c}\dot\varepsilon^{m_c})] \sim \Delta T$.

3.6.3 Result
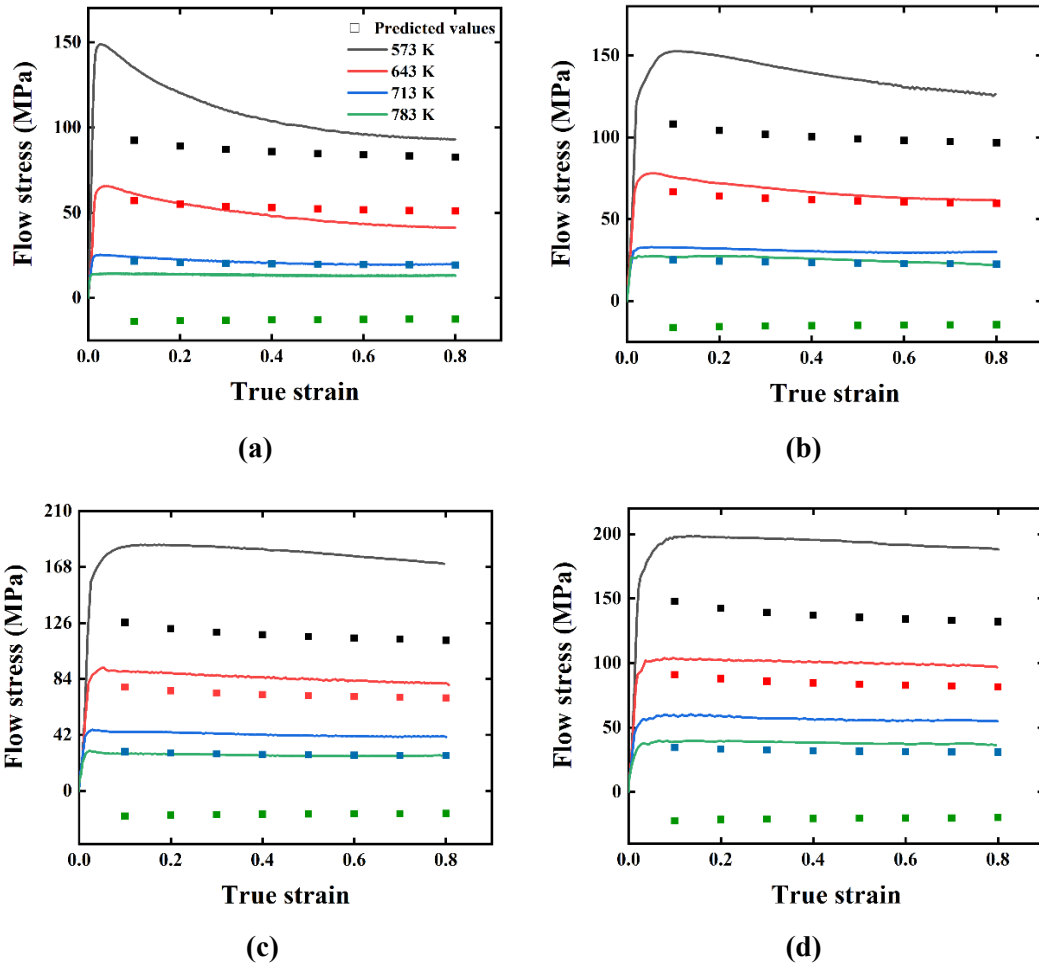
Fig. 3.17 Comparison between experimental and predicted flow stress using K-D

model at the temperatures of (a) 0.001 s^{-1}; (b) 0.01s^{-1}; (c) 0.1s^{-1}; (d) 1s^{-1}

Fig. 3-17 shows the comparison of Kobayashi-Dodd model with experimental values under

16 experimental conditions.

It can be seen from **Fig. 3.17** that there are deviations between the predicted values and the

experimental values, and the deviations are larger at the temperatures of 573K and 783K at all

strain rates, and the deviations are smaller at the temperatures of 643K and 713K.

3.7 Modified Fields–Backofen Model

3.7.1 Introduction

In 1957, Fields and Bachofen proposed the Fields–Backofen (FB) equation. But the FB fomula just can describe the flow stress curves of alloys and metal sheets in the strain hardening stage at high strain rates [76]. Zhang introduced a softening term to describe the softening behavior. This equation provides a better representation in many alloys (e.g., AZ80 magnesium alloy [77], 42CrMo steel [78], AZ31 magnesium alloy [76], 7075 aluminum alloy [79], 5052 aluminum alloy [80], etc.).

3.7.2 Modified Fields–Backofen Model

The Modified Fields-Backoften (MFB) model can be expressed as follow[76]:

$$\sigma = C\varepsilon^{n_c}\dot{\varepsilon}^{m_c}\exp(bT + s\varepsilon) \tag{3-54}$$

where σ is flow stress, C and b are material constants, ε is strain, n_c is the work-harding coedfficien, $\dot{\varepsilon}$ is the strain rate, m_c is strain-rate sensitivity index, s the exponential effect of work softening. Taking the natural logarithm on both sides of the **Eq. (3-54)**:

$$\ln\sigma = \ln C + n_c\ln\varepsilon + m_c\ln\dot{\varepsilon} + bT + s\varepsilon \tag{3-55}$$

Making $K_1 = \ln C + n_c\ln\varepsilon + bT + s\varepsilon$, then an equation of σ and $\dot{\varepsilon}$ at certain temperature and strain can be got, as shown in **Fig. 3.18 (a)**. Thirty-two m_c values can be calculated by the plot of $\ln\sigma \sim \ln\dot{\varepsilon}$ under all experament temperature and strain rate. m_c is the average value of all slope values.
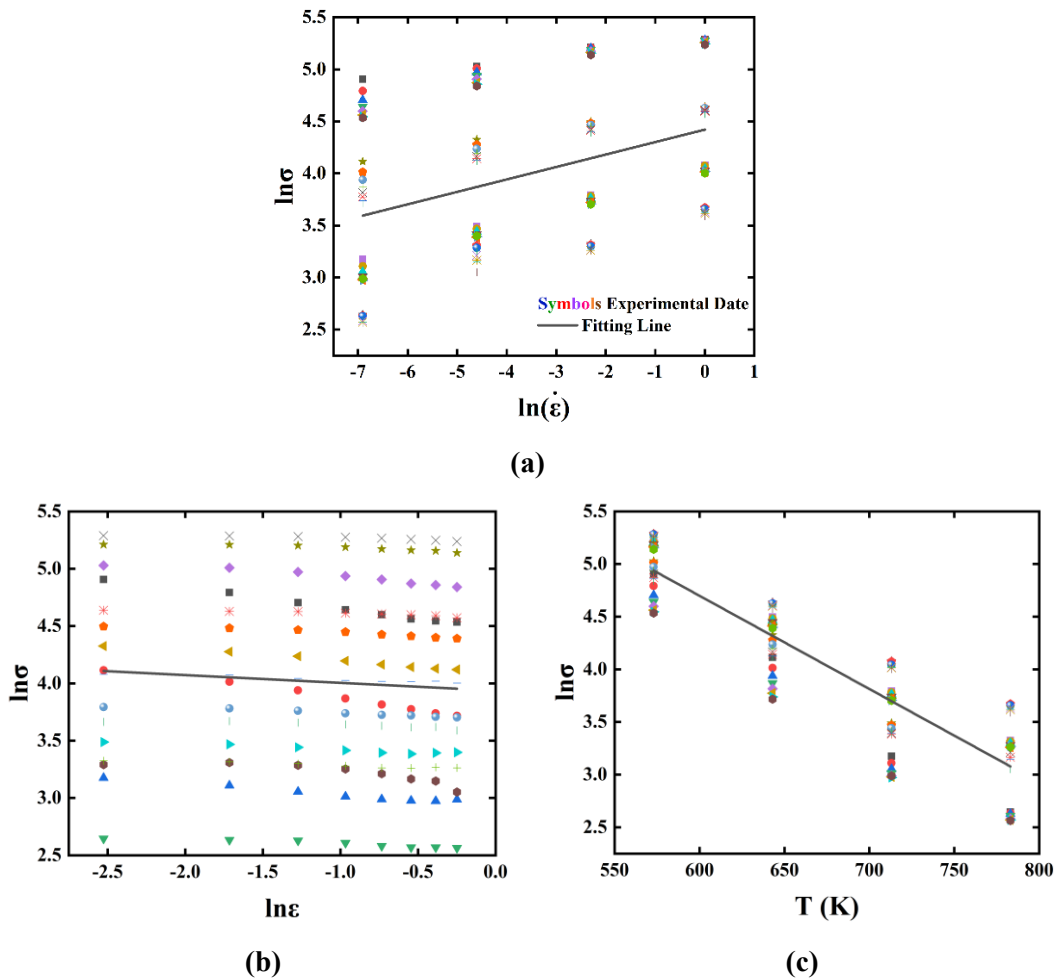
Fig. 3.18 Plot of (a) $\ln\sigma \sim \ln\dot{\varepsilon}$; (b) $\ln\sigma \sim \ln\varepsilon$; (c) $\ln\sigma \sim T$

$$\ln\sigma = m_c\ln\dot{\varepsilon} + K_1 \tag{3-56}$$

Similarly, making $K_2 = \ln C + m_c\ln\dot{\varepsilon} + bT + s\varepsilon$, an equation relating flow stress and strain at a specific temperature and strain rate can be derived, which is shown in **Fig. 3.18 (b)**. Sixteen n_c values can be calculated by the plot of $\ln\sigma \sim \ln\varepsilon$. n_c is the average value of all slope values.

$$\ln\sigma = n_c\ln\varepsilon + K_2 \tag{3-57}$$

In the same way, making $K_3 = \ln C + m_c\ln\dot{\varepsilon} + n_c\ln\varepsilon + s\varepsilon$, an equation of flow stress and temperature at certain strain and strain rate can be got, as shown in **Fig. 3.18 (c)**. Thirty-two b

values can be taken by the plot of $\ln\sigma \sim T$. b is the average value of all slope values.

$$\ln\sigma = bT + K_3 \tag{3-58}$$

Then, making $K_4 = \ln C + m_c \ln\dot\varepsilon + bT$, **Eq. (3-59)** of flow strain and temperature can be got.

$$\ln\sigma = n_c \ln\varepsilon + s\varepsilon + K_4 \tag{3-59}$$

When $\varepsilon = 0.08 = e^{-2.52573}$, **Eq. (3-59)** can be expressed as **Eq. (3-60)**:

$$\ln\sigma_{e^{-2.52573}} = -2.52573n_c + se^{-2.52573} + K_4 \tag{3-60}$$

And when $\varepsilon = 0.18 = e^{-1.7148}$, **Eq. (3-59)** can be expressed as **Eq. (3-61)**:

$$\ln\sigma_{e^{-1.7148}} = -1.7148n_c + se^{-1.7148} + K_4 \tag{3-61}$$

Combine **Eq. (3-60)** and **(3-61)** to get **Eq. (3-62)**:

$$s = \left[\ln\left(\frac{\sigma_{e^{-2.52573}}}{\sigma_{e^{-1.7148}}}\right) - n\right] / (e^{-2.52573} - e^{-1.7148}) \tag{3-62}$$

One hundred and twevel values can be calculated, and the s value can be got by the average value. Rearranging Eq. (3-54), congtant C can be got from the following equation:

$$C = \sigma / [\varepsilon^{n_c}\dot\varepsilon^{m_c}exp(bT + s\varepsilon)] \tag{3-63}$$

Therefore, one hundred and twenty-eigth values for C can be got, and the average C value is shown in **Table 3-9**. Finally, the MFB model of 6061-T6 alumimum can be obtained:

$$\sigma = 32498.69\varepsilon^{-0.06767}\dot\varepsilon^{0.11965}exp(0.00885T - 0.06848\varepsilon) \tag{3-54}$$

Table 3-9 The material contants of modified Fields–Backofen model

Constant	C	n_c	m_c	b	s
	32498.69	-0.06767	0.11965	0.00885	-0.06848

3.7.3 Result
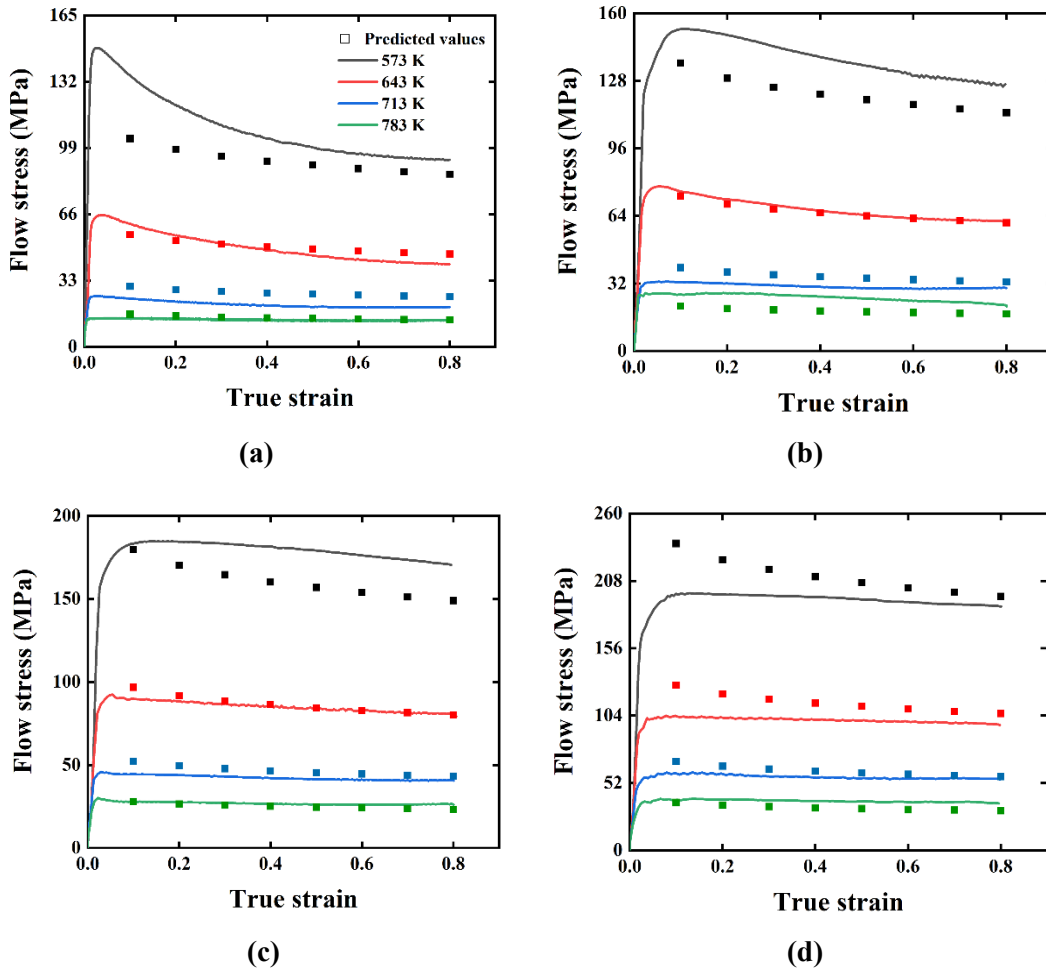
Fig. 3.19 Comparison between experimental and predicted flow stress using MFB

model at the temperatures of (a) 0.001 s^{-1}; (b) 0.01s^{-1}; (c) 0.1s^{-1}; (d) 1s^{-1}

By utilizing the aforementioned constitutive model, the flow stress is estimated for each

experimental condition using **Eq. (3-54)**. A comparison is then made between the experimental

and predicted values, as illustrated in **Fig. 3.19**. This analysis contributes to weight reduction

efforts by evaluating the accuracy and reliability of the model in capturing the material's

response under different conditions.

It can be seen from **Fig. 3.19** that the prediction of the MFB model is similar to that of the

MJC model. The fit between the predicted value and the experimental value is good, but there is a deviation when the temperature is 573K. In comparison, the deviation of the predicted value of the MFB model at 573K is smaller than that of the MJC model. Hence, the developed model can be employed to forecast the flow stress of 6061-T6.

4 Evolution of activation energy

4.1 Introduction

To achieve optimal yield in metal processing, meticulous selection of process parameters including temperature, rate of change of strain, and strain variation is imperative [81]. The same positional error motion is required to create and sustain plasticity flow in plastic deformation.

The activation energy Q, determined through dynamic analysis, characterizes the energy hurdle for dislocation movement and signifies the material's resistance to deformation. [82]–[85]. Base on the concept of activation energy, Malas [86] proposed the construction of an activation energy diagram to validate the thermal processing window. The region where the Q value remains consistent can be considered an optimal and secure area for effective work.

Therefore, Q can serve as a valuable denote for selecting suitable parameters and optimizing the thermal deformation process. [81]. Furthermore, the relationship between Q and strain can also be polynomially fitted [87], [88], and based on the same flow stress data in previous work, the corresponding composition equations for alloys with strain compensation were developed. According to the analysis of the Arrhenius-type model in Section 3.2, the flow behavior of 6061 aluminum alloy changes significantly with temperature, strain rate, and strain. Therefore, for materials with high strain sensitivity, it is important to develop activation energy diagrams involving strain, strain rate, and temperature[89].
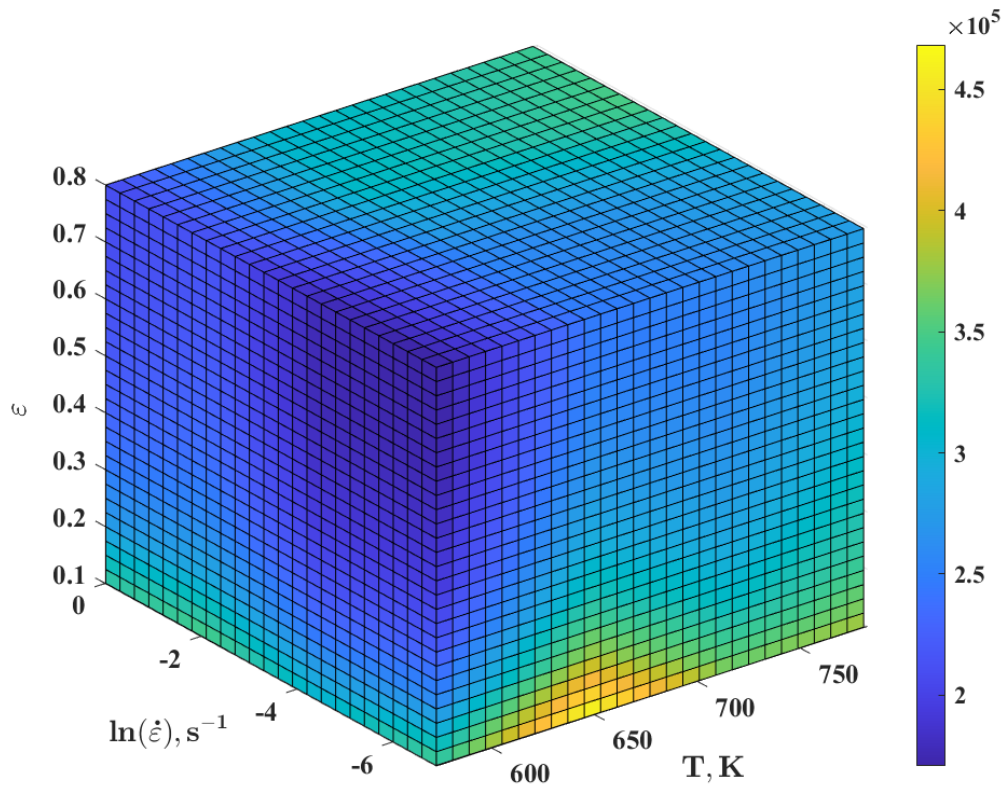
Fig. 4.1 three-dimensional activation energy map at different temperatures, strain, and

strain rates.

A series of Q values were obtained by the method in Section 3.2, at different temperatures

(523~673 K), strain rates (0.001–1 s^{-1}), and strains (from 0.1 to 0.8 in intervals of 0.1). Based

on these values, a three-dimensional activation energy map (**Fig. 4.1**) was created to provide

a comprehensive analysis of the Q evolution under various deformation conditions.

4.2   Effect of strain on activation energy

As shown in **Fig 4.2**, the Q value of 6061-T6 aluminum alloy decreases significantly with the deepening of plastic deformation. This situation is because a lot of deformation heat is producted during deformation and stored in the deformation system. The increase of heat increases the activity of atoms, thus reducing the threshold of microstructure evolution, which is reflected in the decrease of activation energy. It can be seen that the changes in **Fig. 4.2 (a)~(d)** are more obvious because the press needs to apply a lot of kinetic energy to the alloy in the initial deformation stage so that the material deforms at a certain deformation rate. Therefore, the energy increase in the deformed system is most pronounced at this stage. In contrast, at the stage of strain 0.5~0.8, the increase in the internal temperature of the system is not enough to have a significant impact on the change of Q.

As shown in **Fig. 4.2 (a)**, the Q value fluctuates the most under different deformation conditions. This is due to the significant influence of both temperature and strain on the plastic deformation of the alloy, particularly during the initial stage of deformation when a substantial number of dislocations are generated and entangled. Non-linear behavior. As the deformation progresses, the offset and rearrangement of dislocations within the material and the transition from low-angle grain boundaries to high-angle grain boundaries transform subgrains into grains, making the change of Q relatively stable.

To facilitate a more visual observation of the activation energy evolution under different strains, **Fig. 4.3** shows the stacked diagram of the change of Q value.
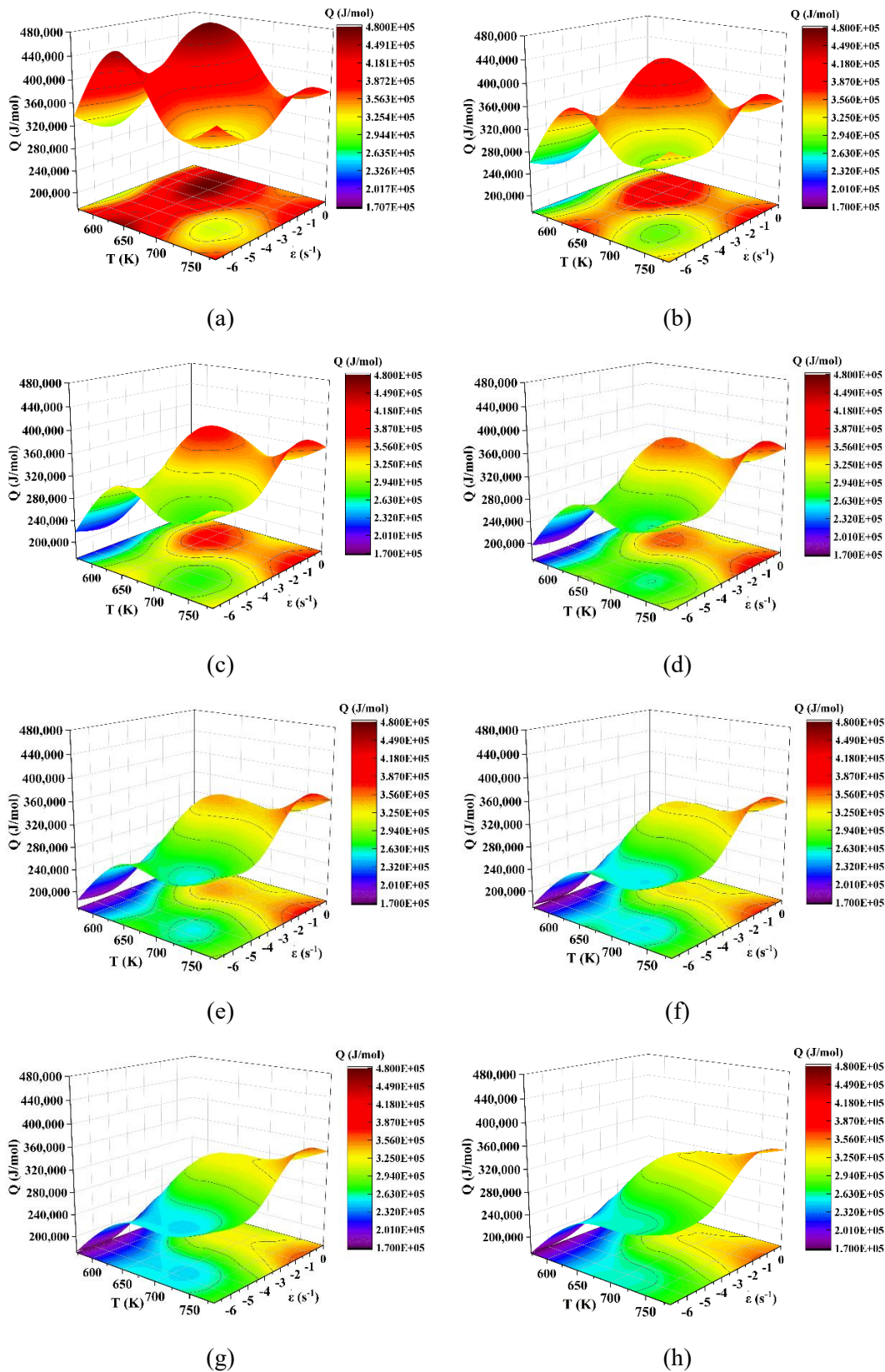
Fig 4.2 3D diagram of the change of Q under different strain rates (a) 0.1; (b) 0.2; (c) 0.3 (d) 0.4; (e) 0.5; (f) 0.6; (g) 0.7; (h) 0.8.
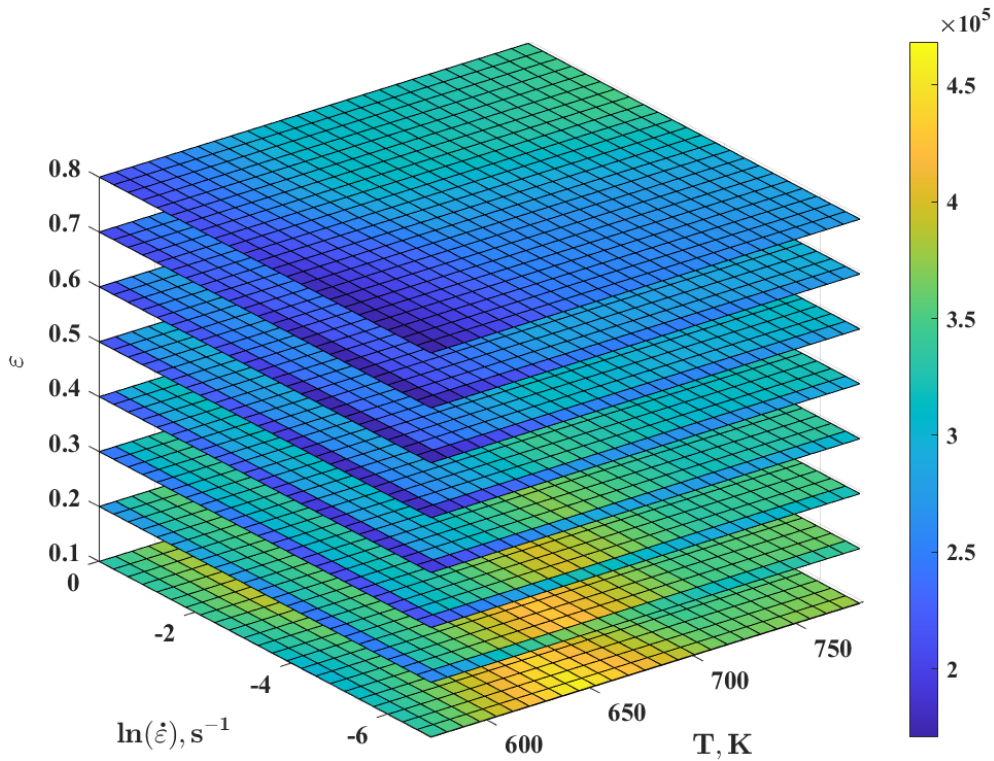
Fig. 4.3 three-dimensional activation energy map at different strain (0.1~0.8).

4.3 Effect of strain rate on activation energy

It is important to highlight that the activation energy Q is influenced by the interactions

between potentially mobile dislocations and other dislocations, solutes, or precipitates, as well

as the periodic friction at grain boundaries or lattices. These factors ultimately determine the

flow rate and yield strength of the material under constant conditions [90]. The deformation-

induced variation in the density of mobile dislocations ρ can be expressed by the following

equation, illustrating the contrasting relationship with the applied strain rate.[91]:

$$\dot{\varepsilon} = K\rho b\bar{v} \qquad (4\text{-}1)$$
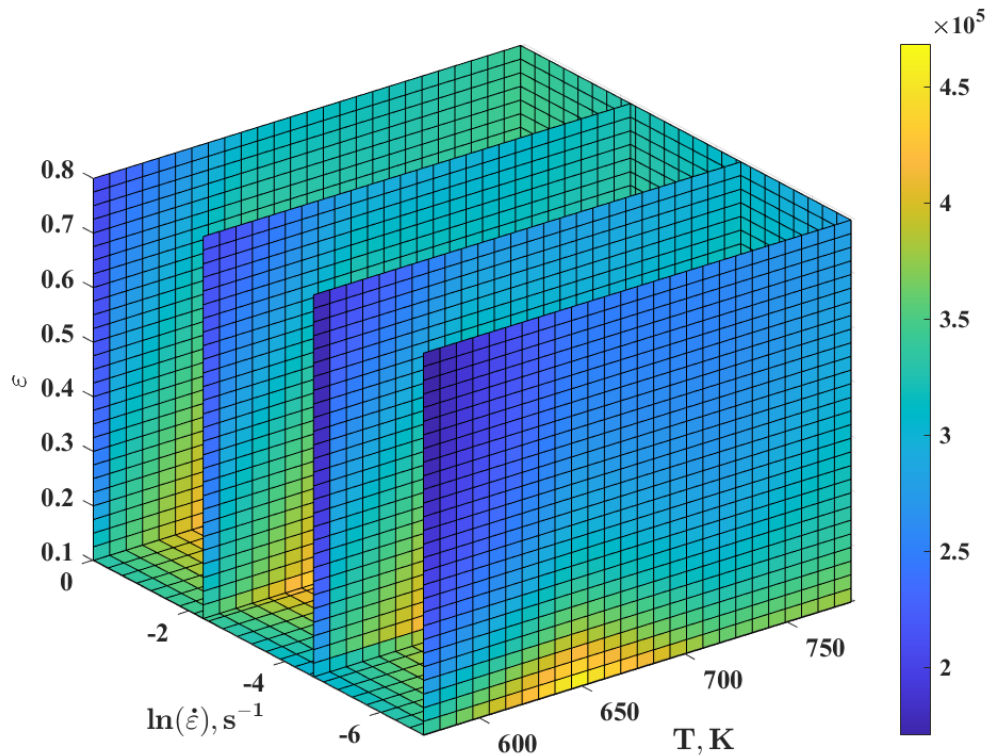
Fig. 4.4 three-dimensional activation energy map at different strain rates (0.001~1 s⁻¹).

Combining **Eq. (3-20)** and **(4-1)**, it can be known that Q is related to the dislocation density.

Fig. 4.4 depicts the evolution of the activation energy Q at different strain rates. An observation reveals that Q exhibits an upward trend as the strain rate increases. This phenomenon can be attributed to the elevated dislocation entanglement resulting from higher strain rates, consequently leading to an increased energy barrier. The corresponding increase in strain rate makes the DRV time shorter, and the difficulty of dislocation movement leads to the proliferation of dislocations, so the minimum value of Q tends to appear at a strain rate of $0.01\mathrm{s}^{-1}$.

4.4   Effect of temperature on activation energy

Fig. 4.5 illustrates the evolution of the Q at different temperatures. At low strain rates, With an increase in temperature, there is an initial rise followed by a rapid decrease in the activation energy Q. The maximum value of Q is observed at approximately 643K. Q increases at 573-643K, accompanied by insufficient DRV. This is because the stacking fault energy of the Al-Mg alloy is low, resulting in a larger extended dislocation that is difficult to escape from the dislocation network [92]. This limits the slip and climb of dislocations and makes it difficult for DRV to occur[93]. Thus DRX can be induced more easily with increasing temperature, and thermal energy is used to overcome the increase in energy barrier [89]. Dislocation motion is a thermally activated process that drives atomic activity and dislocation slip at high-temperatures. The average speed of dislocation is affected by many factors, which can be expressed as the following equation [85]:

$$\bar{v} = \beta b v \exp\left(-\frac{\Delta G(\sigma_S)}{kT}\right) \quad (4\text{-}2)$$

where β denote a dimensionless constant, v represent a attempt frequency, b represent a material constant, k corresponds to a Boltzman constant, usually k=1.3807×10^{-23}, $\Delta G(\sigma_S)$ is the free energy of the activity, which can be expressed as:

$$\Delta G(\sigma_S) = \Delta F\left(1 - \frac{\sigma_S}{\tau}\right) \quad (4\text{-}3)$$

where ΔF corresponds to the total free energy used to overcome the barrier without the help of external stress, σ_S signifies the yield stress, and τ signifies the external stress that forces the dislocation to pass through the barrier without the help of thermal energy

Through **Eq. (4-1)** and **(4-2)**, By elevating the temperature under a particular strain rate, the dislocation density can be significantly diminished, leading to effective reduction. This

observation aligns with the changes observed within the temperature range of 643K to 783K in **Fig. 4.5**. This is because the level of DRV can be enhanced by increasing temperature, thereby this temperature increase aids in diminishing the dislocation density and alleviating the restriction on dislocation motion. Due to the failure of dislocation motion, Q decreases with increasing temperature. Therefore, a higher temperature (643-783K) helps minimize Q, thereby improving work efficiency.
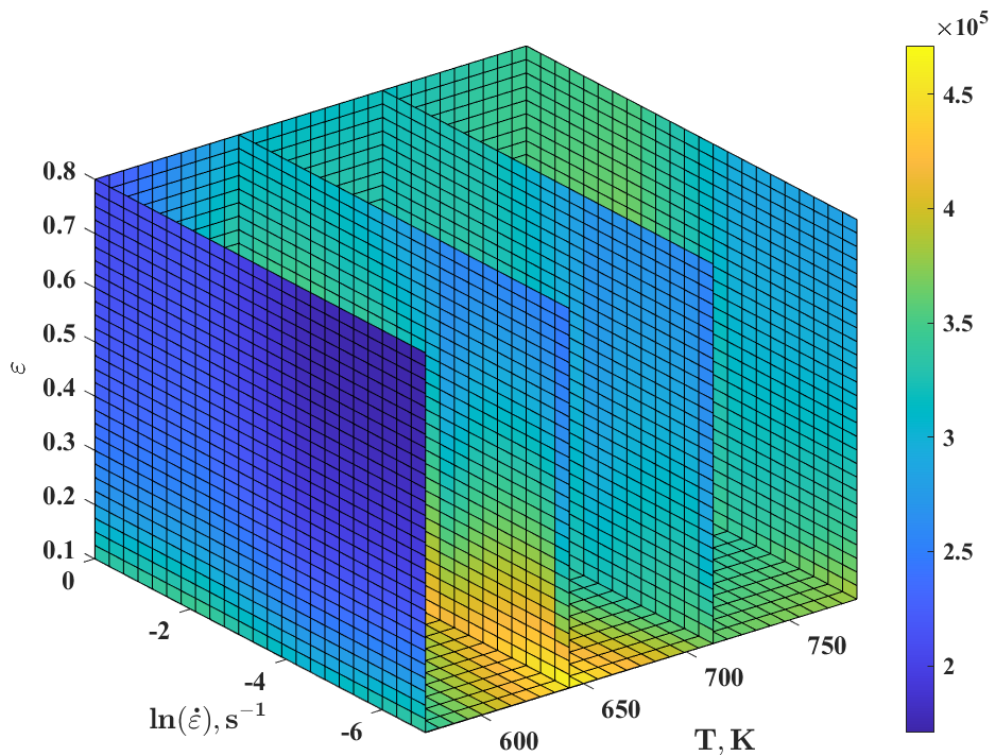
Fig. 4.5 three-dimensional activation energy map at different temperatures (573K, 643K, 713K, 783K).

5   Result and Discussion

Through the equations solved in the third part, the comparison between the predicted value of each constitutive model and the real experimental value can be analyzed. It can be obtained that the predicted values calculated by the three models of the Arrhenius-type (A-T) model, modified Zerilli-Armstrong (MZA) model, and SK-Pual model under all experimental conditions can fit with the experimental values. Therefore, the A-T model, MAZ model, and SK-Pual model can provide suitable predicted values. They are suitable for predicting the flow stress of the alloy. Moreover, by comparing the predicted value calculated by using the modified Johnson-Cook (MJC) model with the experimental value, it is found that except for the phenomenon of non-fitting at 573K, the fitting situation under other conditions is good. The fitting result of the modified Fields–Backofen (MFB) model is similar to that of the MJC model, and there is a slight deviation when the temperature is 573K, but in comparison, the deviation of the MFB model is smaller than that of the MJC model, so these two models can also be used for 6061-T6 The flow stress is predicted. The flow stress value predicted by Kobayashi-Dodd (K-D) model at the reference temperature fits well with the experimental value, but there is a slight deviation at other temperatures. Due to the inaccurate predicted value, it is not recommended to use this model to predict the flow stress. Unlike the other six models, the predicted values of the Wang-Jiang (W-J) model can fit the experimental values except for some conditions, but there are dramatic deviations under most conditions, so the W-J model is not applicable to the 6061-T6 aluminum alloy.

After the metal constitutive model is established, the average absolute relative error (AARE) and correlation coefficient (R^2) are often compared [29]. The role of these evaluation indicators is to evaluate the fitting degree and predictive ability of the metal constitutive model and to verify its feasibility and effectiveness in practical applications[94].

The calculation of AARE is shown in **Eq. (5-1)**, and it is an index to measure the error between the model prediction and the actual observation value. It calculates and averages the relative error between model predictions and actual observations. AARE can help evaluate how well a model predicts an entire dataset and a lower AARE value indicates a better predictive ability of the model.

$$AARE(\%) = \frac{1}{N} \sum_{i=1}^{N} \left| \frac{E_i - P_i}{E_i} \right| \times 100 \tag{5-1}$$

The calculation of the R^2 of determination is shown in **Eq. (5-2)**, which is one of the commonly used indicators for evaluating the degree of model fitting. It measures the correlation between model predictions and actual observations. The value range of the R^2 of determination is between 0 and 1, and the closer to 1, the stronger the ability of the model to explain the actual observations. A coefficient of determination of 1 indicates that the model fits the actual observations perfectly.

$$R^2 = \frac{\sum_{i=1}^{N}(E_i - \bar{E})(P_i - \bar{P})}{\sqrt{\sum_{i=1}^{N}(E_i - \bar{E})^2 \sum_{i=1}^{N}(P_i - \bar{P})^2}} \tag{5-2}$$

where, N is the number of data point，E_i and P_i are experimental value and predicted value, respectively. $\bar{E}$ and $\bar{P}$ are the average value of experimental values and the average value of predicted values, resperctively.

77

By comparing AARE and R^2, the predictive ability and fitting degree of the metal constitutive model can be comprehensively evaluated. The values of AARE and R^2 of the seven equations are shown in **Table 5-1**. The accuracy results of the seven models measured by R^2 are shown in **Fig. 5.1**, where (a) MJC model, (b) A-T model, (c) MZA model, (d) W-J model, (e) SK-Pual model; (f) K-D model; (g) MFB model.

Comparing the seven plots of experimental and predicted flow stresses in **Fig. 5.1**. It can be shown that, in comparison, the AT model, MZA model, SK-Pual model, and MFB model have better correlations between the prediction results and the experimental data, and the MZA model has the best correlation, reaching 0.99138. On the contrary, the correlations of the MJC model, W-J model, and K-D model are much lower, with W-J being the worst.

In order to better compare the prediction capabilities of the seven constitutive models, 3D histograms are used to describe the changes of AARE of each model at different temperatures and strain rates, as shown in **Fig. 5.2-5.5**. **Fig. 5.2** shows the AARE histograms of all models at different temperatures. It can be seen that the AARE value of the K-D model at 783K and the W-J model at 573K is too large. **Fig. 5.3** shows the AARE histograms of all models at different strain rates. Similarly, excessive values exist in the K-D model and the W-J model. It can be seen from **Table 5-1** that the AARE values of K-D and W-J are both more than 50%, and some of the values are too large to cause difficult analysis. In order to better analyze other models, after removing the above two models, 3D histograms are used to describe the changes of the other five models AARE at various conditions, as shown in **Fig. 5.4** and **5.5**.

As shown in **Fig. 5.4**, the effect of temperature changes on the MFB model is not obvious, and the accuracy is the highest at 643K. The prediction accuracy of the SK-Pual model, MZA model, A-T model, and MJC model decreases with the increase of temperature, but the accuracy of the A-T model and MZA model changes very little with temperature, SK-Pual model and MJC model is greatly affected by temperature, and the accuracy is the worst when the temperature is 783K.

As shown in **Fig. 5.5**, in a comprehensive sense, the accuracy of the five models decreases with the decrease of the strain rate, but the accuracy of the MFB model, MZA model, and A-T model change slightly with the strain rate, and the SK-Pual model and The MJC model is greatly affected by the strain rate, and the accuracy is the lowest when the strain rate is 0.001s. In a word, by analyzing the four 3D histograms, in comparison, the three models of AT, MZA, and MFB have better-predicted structures. They are less affected by changes in temperature and strain rate, followed by the MJC model and SK-Pual model, which will Because of changes in temperature and strain rate, the accuracy of the W-J model and K-D model is the worst.

It can be seen from Table 4-1 that the R of the MZA model is 0.99138, closest to 1, and has the smallest AARE value of 10.66%. Hence, among the seven models considered, the MZA model exhibits the highest accuracy in predicting the flow stress of the high-temperature aluminum alloy material 6061-T6.

Table 5.1 The values of AARE and R^2 of the seven constitutive models

	MJC	A-T	MZA	W-J	SK-Pual	K-D	MFB
R^2	0.9607	0.98925	0.99138	0.36741	0.98631	0.92615	0.9824
AARE	16.249%	11.443%	10.666%	52.194%	19.19%	58.861%	11.251%

In the research utilizing the A-T constitutive equation, an activation energy map was developed to elucidate the relationship between the Q value, temperature, and strain rate. The findings demonstrated the remarkable sensitivity of the Q value to strain, temperature, and strain rate, thereby highlighting the potential for adjusting the deformation parameters to modify the processability of the alloy. At the same time, the evolution of the internal microstructure of the alloy, such as DRV, work hardening, and DRX, has a significant impact on Q value. This finding is of significant importance for a deeper understanding of the deformation behavior of the alloy and for optimizing the processing conditions.

(a)   (b)
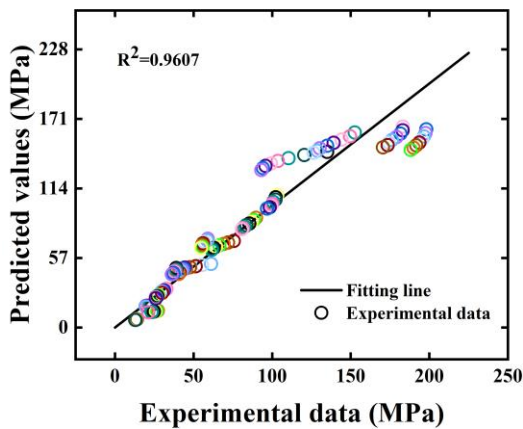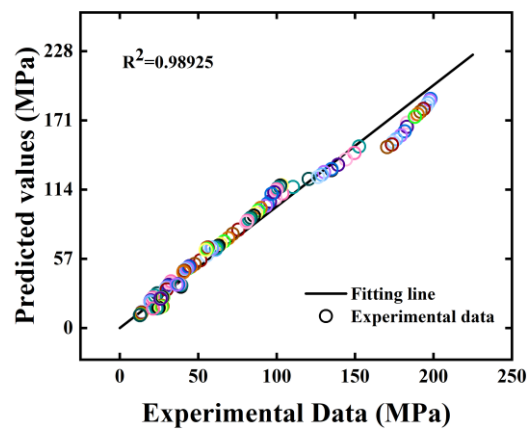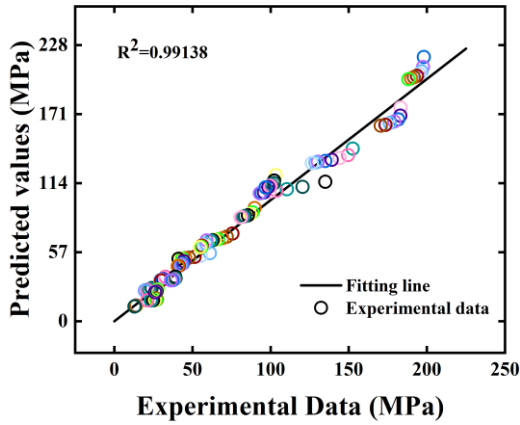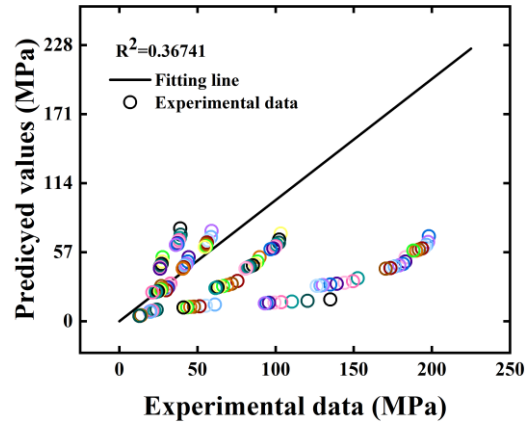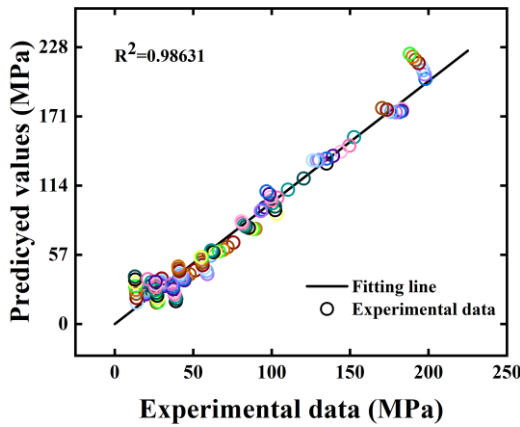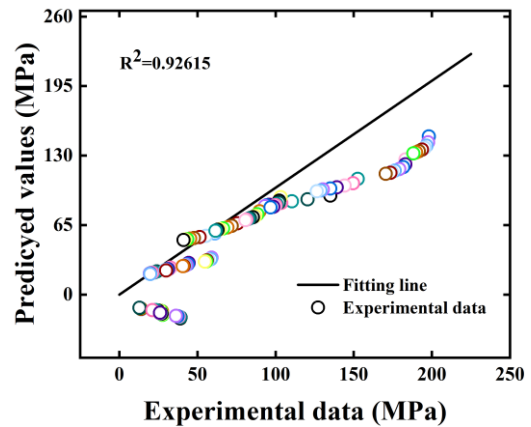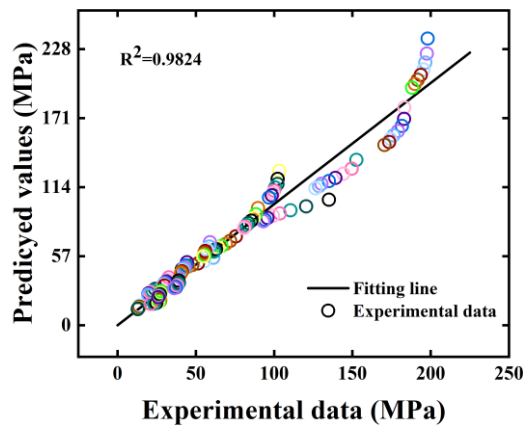
Fig. 5.1 The correlation coefficient (R^2) for seven constitutive models: (a) MJC

model, (b) A-T model, (c) MZA model, (d) W-J model, (e) SK-Pual model; (f) K-D model;

(g) MFB model
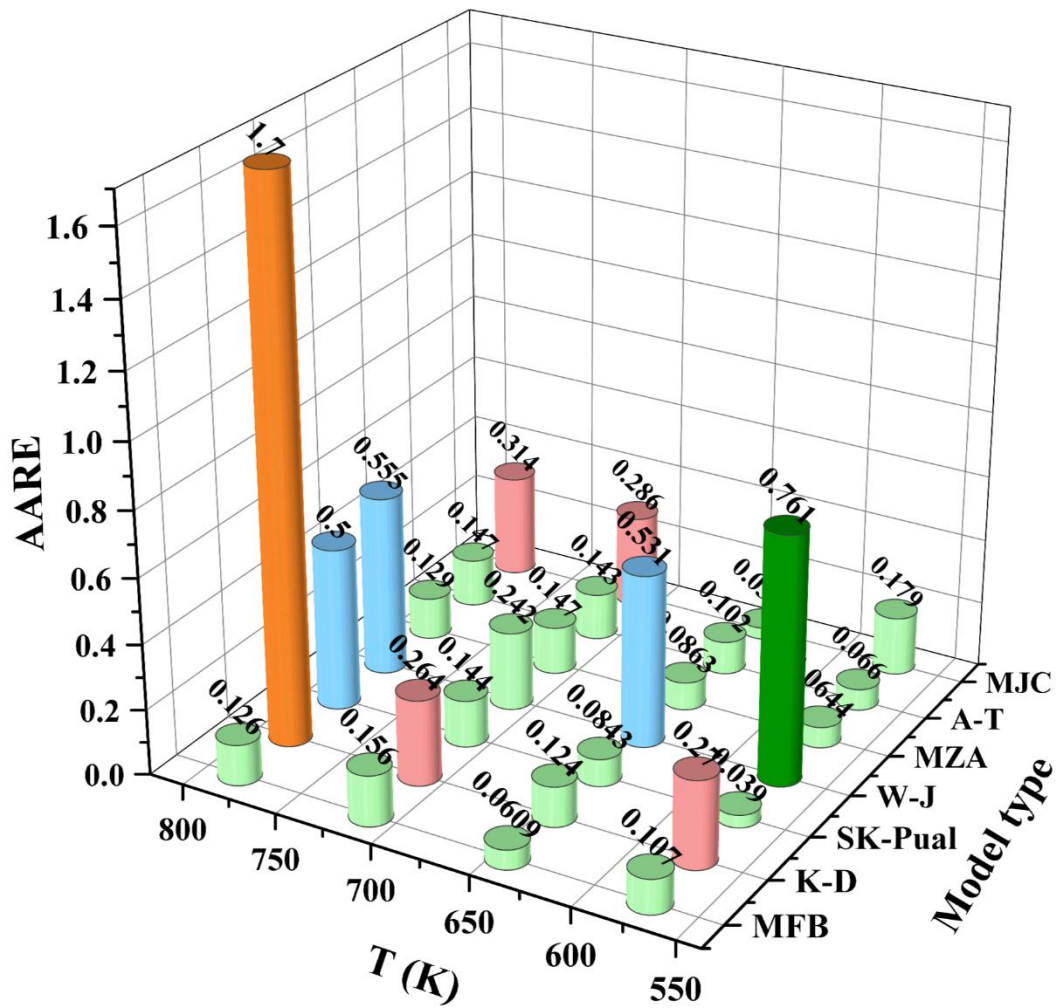
Fig. 5.2. The AARE histograms of all models at different temperatures
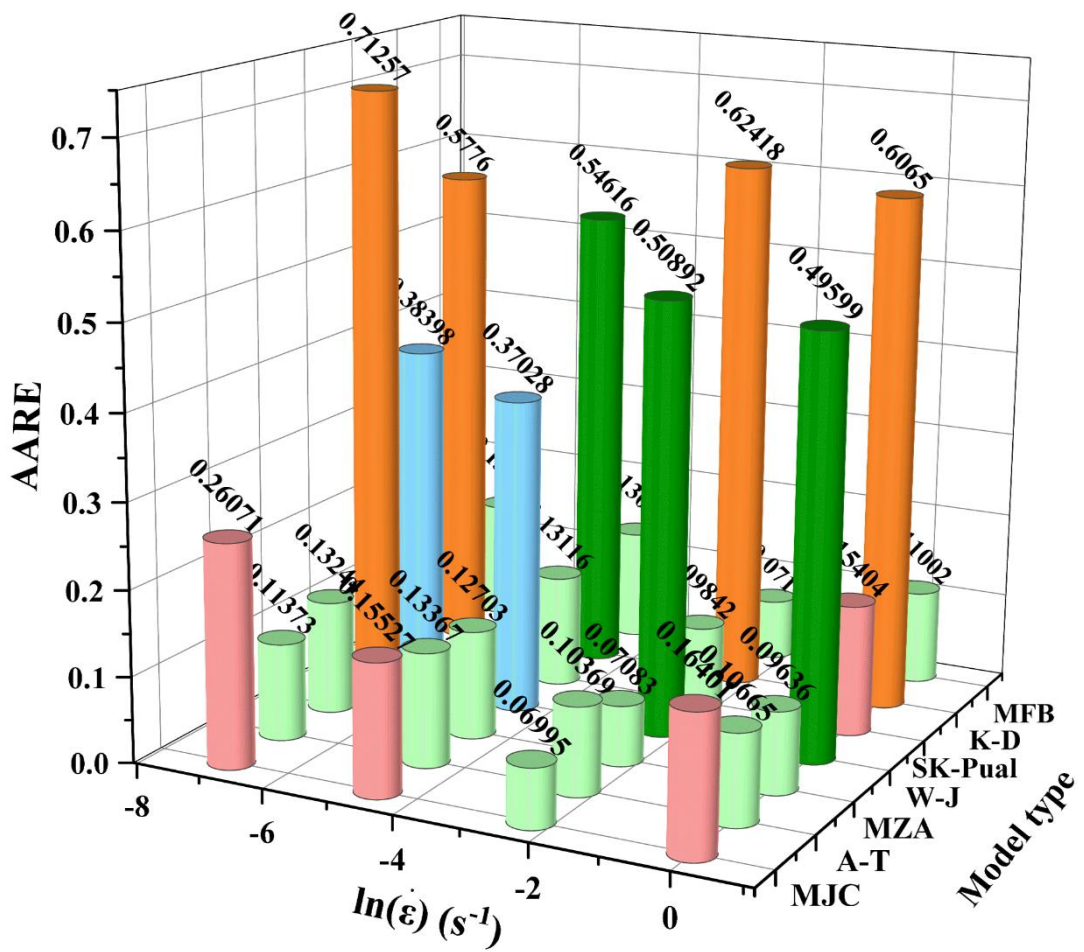
Fig. 5.3. The AARE histograms of all models at different strain rates
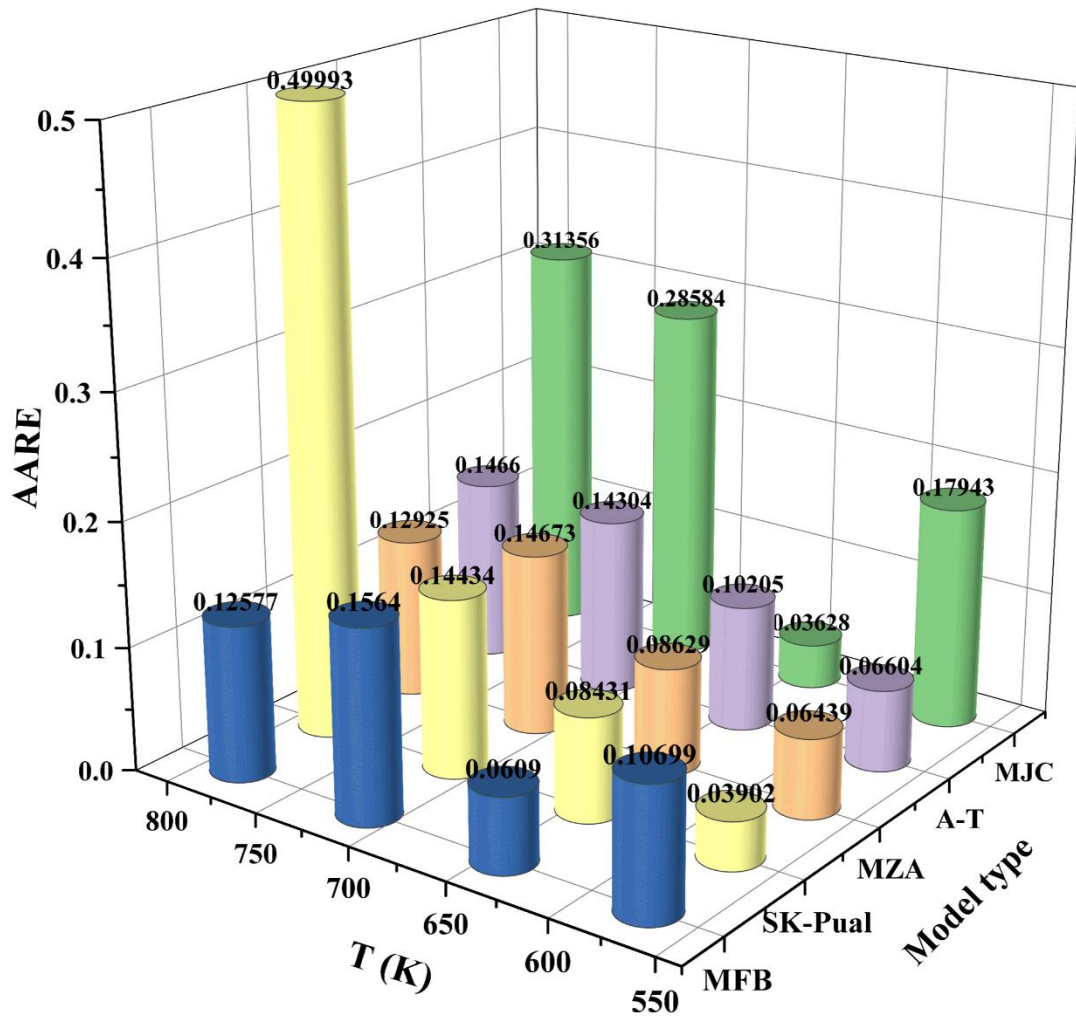
Fig. 5.4. the AARE histograms of part models at different temperatures
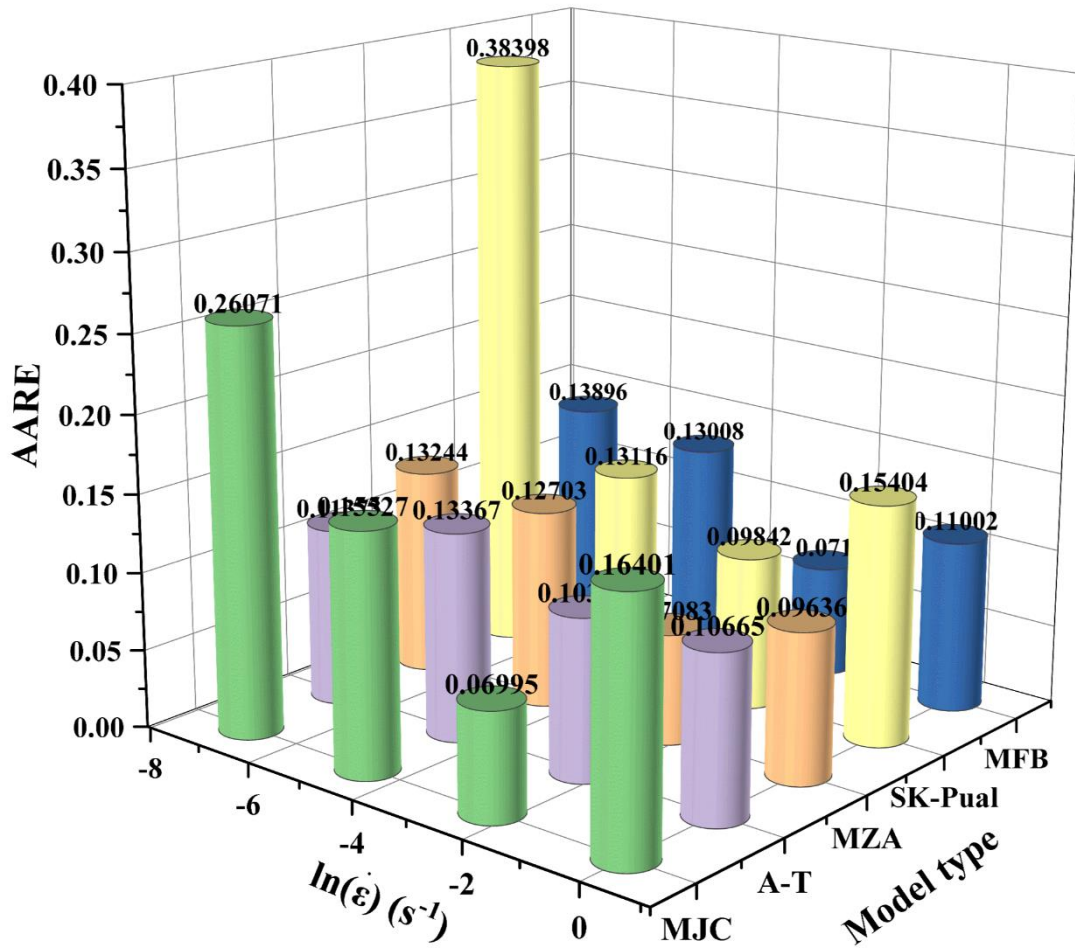
Fig. 5.5. the AARE histograms of all models at different strain rates

6   Conclusion

The thermal compression test was conducted using the Gleeble-3800 thermal simulation testing machine, and sixteen sets of compression tests were done according to the temperature and strain rate. On the basis of this experiment, the relationship amoung the flow stress, temperature, and strain rate of 6061-T6 aluminum alloy was studied according to the experimental data, according to the experimental data, seven constitutive equations of the aluminum alloy were determined: modified Johnson-Cook (MJC) model, Arrhenius-Type (A-T) model, modified Zerilli-Armstrong (MZA) model, Wang-Jiang (W-J) model, SK-Paul model, Kobayashi-Dodd (K-D) model, and modified Fields-Backofen (MFB) model. The models are compared by means of fitting the predicted value with the experimental value, calculating AARE and R^2 numerical statistical analysis. The following conclusions were obtained:

(1) Among the above seven constitutive equations, the predicted values calculated by the three models of the Arrhenius-type model, MZA model, and SK-Pual model under all experimental conditions are in good fit with the experimental values, which can be used for the prediction of 6061-T6 aluminum alloy. In contrast, the Wang-Jiang model has the worst fit and cannot be used to predict the flow stress of the test material.

(2) All these results obtained from these seven models vary significantly under certain deformation conditions, and the primary factor for this is likely due to that the deformation behavior of materials at high-temperature and strain rates is highly nonlinear.

(3) The R^2 and AARE predictability of seven constitutive equation models were measured, and

the results showed that the AARE values of MJC model, A-T model, MZA model, W-J model,

SK-Paul model, K-D model, and MFB model were 16.249%, 11.443%, 10.666%, 52.194%,

19.19%, 58.861%, and 11.251%, respectively, and the R^2 values were 0.9607, 0.98925,

0.99138, 0.36741, 0.98631, 0.92615, and 0.9824, respectively. Compared with other models,

the MZA model has the R closest to the critical correlation value 1, and the AARE value is the

smallest, which can most accurately represent the high-temperature flow behavior in the entire

processing region.

(4) The MZA model of 6061 aluminum alloy in high-temperature compression steady state is:

$$\sigma = (80.974 + 4.169349\varepsilon^{-0.47676})\exp[-(0.00916 - 9.40476 \times 10^{-5}\varepsilon)T^* + (0.11057 + 0.000259T^*)\ln\dot{\varepsilon}^*]$$

(5) The activation energy diagram depicts the significant nonlinear effects of temperature,

strain, and strain rate on the variation of the Q value. The evolution of the internal

microstructure of the alloy, such as DRX, DRV, and work hardening, has a significant effect

on the Q value.

Reference

[1] G. U. Jeong, J. Park, C. K. Jin, Y. H. Moon, and C. G. Kang, "Thermal Deformation Behavior and Formability of High-temperature with Corrosion Resistance Alloy," *Key Engineering Materials*, vol. 794, pp. 142–150, 2019, doi: 10.4028/www.scientific.net/KEM.794.142.

[2] Z. Liu, Q. Sun, M. Wang, T. Zhu, and F. Ji, "Study on the constitutive model of porous titanium alloy," *Emerging Materials Research*, vol. 8, no. 3, pp. 365–375, Sep. 2019, doi: 10.1680/jemmr.16.00153.

[3] R. Shen, Y. Quan, Z. Zhang, R. Ma, and Q. Wang, "Metal–Organic Framework as an Efficient Synergist for Intumescent Flame Retardants against Highly Flammable Polypropylene," *Ind. Eng. Chem. Res.*, vol. 61, no. 21, pp. 7292–7302, Jun. 2022, doi: 10.1021/acs.iecr.2c00715.

[4] F. Qayyum, S. Guk, and U. Prahl, "Applications of Crystal Plasticity in Forming Technologies," *Crystals*, vol. 12, no. 10, Art. no. 10, Oct. 2022, doi: 10.3390/cryst12101466.

[5] X. Li *et al.*, "Research on high-temperature deformation behavior and constitutive relation of TiAl alloy," *J. Phys.: Conf. Ser.*, vol. 2390, no. 1, p. 012074, Dec. 2022, doi: 10.1088/1742-6596/2390/1/012074.

[6] B. Blaiszik, K. Chard, J. Pruyne, R. Ananthakrishnan, S. Tuecke, and I. Foster, "The Materials Data Facility: Data Services to Advance Materials Science Research," *JOM*, vol. 68, no. 8, pp. 2045–2052, Aug. 2016, doi: 10.1007/s11837-016-2001-3.

[7] R. K. Singh, S. S. S. Guraja, O. O. Ajide, G. M. Owolabi, and N. Kumar, "Investigation of initial metallurgical factors on the dynamic impact response and adiabatic shear bands formation of the 6061 Al alloy," *Materials Science and Engineering: A*, vol. 865, p. 144636, Feb. 2023, doi: 10.1016/j.msea.2023.144636.

[8] Y. Zhao, L. Xu, M. Guo, Z. Li, X. Li, and S. Wei, "Compressive properties and deformation behaviors of sintered W-m-ZrO2 alloy under different temperature," *Materials Science and Engineering: A*, vol. 859, p. 144238, Nov. 2022, doi: 10.1016/j.msea.2022.144238.

[9] W. J. Bratina and S. Yue, "Fatigue Crack Growth — A Metallurgist's Point of View," in *Time-Dependent Fracture*, A. S. Krausz, Ed., Dordrecht: Springer Netherlands, 1985, pp. 27–42. doi: 10.1007/978-94-009-5085-6_3.

[10] G. Ji, G. Yang, L. Li, and Q. Li, "Modeling Constitutive Relationship of Cu-0.4 Mg Alloy During Hot Deformation," *J. of Materi Eng and Perform*, vol. 23, no. 5, pp. 1770–1779, May 2014, doi: 10.1007/s11665-014-0912-0.

[11] H. Ahmadi, H. R. Rezaei Ashtiani, and M. Heidari, "A comparative study of phenomenological, physically-based and artificial neural network models to predict the Hot flow behavior of API 5CT-L80 steel," *Materials Today Communications*, vol. 25, p. 101528, Dec. 2020, doi: 10.1016/j.mtcomm.2020.101528.

[12] M. T. Nasri *et al.*, "Experimental and numerical investigation of sheet metal failure based on Johnson-Cook model and Erichsen test over a wide range of temperatures," *Mechanics of Advanced Materials and Structures*, vol. 0, no. 0, pp. 1–14, Mar. 2022, doi: 10.1080/15376494.2022.2049934.

[13] X. He, P. Jiang, L. Zhou, C. Chen, and X. Deng, "Hot Deformation Behavior of 1Cr12Ni3Mo2VN

Martensitic Stainless Steel," *IOP Conf. Ser.: Earth Environ. Sci.*, vol. 81, no. 1, p. 012031, Aug. 2017, doi: 10.1088/1755-1315/81/1/012031.

[14] D. Li, Z. Yan, R. Wang, Y. Kang, and L. Shen, "Effect of Hot-Deformation Processes on Phase Transformation of Low-Alloyed, Multiphase, High-Strength Steel," *steel research international*, vol. 92, no. 1, p. 1900522, 2021, doi: 10.1002/srin.201900522.

[15] T.-Y. Ni, J.-G. Wang, Z.-J. Li, and R.-F. Yan, "Hot Deformation Behavior and Constitutive Model of AZ80–0.8wt%Y Considering the Compensation of Strain," *Advanced Engineering Materials*, vol. 24, no. 5, p. 2101113, 2022, doi: 10.1002/adem.202101113.

[16] W. Jia, S. Chen, L. Wang, F. Shang, X. Sun, and D. Yang, "Microstructure and properties of Ni-Co-Mn-Al magnetic shape memory alloy prepared by direct laser deposition and heat treatment," *Optics & Laser Technology*, vol. 141, p. 107119, Sep. 2021, doi: 10.1016/j.optlastec.2021.107119.

[17] X. Liu, L. Zhu, and Q. Zhang, "Analysis of TA2 hot deformation behavior and corrected TA2 constitutive model based on DRX," *Mater. Res. Express*, vol. 6, no. 4, p. 046531, Jan. 2019, doi: 10.1088/2053-1591/aafb1a.

[18] H. Li, L. Fan, M. Zhou, Y. Zhou, K. Jiang, and Y. Chen, "Hot Compression Deformation and Activation Energy of Nanohybrid-Reinforced AZ80 Magnesium Matrix Composite," *Metals*, vol. 10, no. 1, Art. no. 1, Jan. 2020, doi: 10.3390/met10010119.

[19] F. S. Qu, X. F. Dong, J. Y. Liu, D. M. Chen, Z. H. Wang, and J. Zhou, "The research on vacuum isothermal bloom for powder metallurgy V-5Cr-5Ti alloy guiding by the constitutive models and the error analysis," *International Journal of Refractory Metals and Hard Materials*, vol. 72, pp. 349–366, Apr. 2018, doi: 10.1016/j.ijrmhm.2018.01.007.

[20] F. Kong, W. Xie, G. Wei, Z. Ma, H. Chen, and C. Fan, "Microstructure evaluation and thermal deformation behaviours of wrought magnesium alloys," *Materials Science and Technology*, vol. 39, no. 3, pp. 283–299, Feb. 2023, doi: 10.1080/02670836.2022.2110374.

[21] X. Luo, S. Dang, and L. Kang, "Compression Deformation Behavior of AZ81 Magnesium Alloy at Elevated Temperatures," *Advances in Materials Science and Engineering*, vol. 2014, p. e717452, May 2014, doi: 10.1155/2014/717452.

[22] Y. Li *et al.*, "Hot deformation and constitutive model of as-cast Ni–Cr–Co nickel-base alloy," *International Journal of Materials Research*, vol. 113, no. 11, pp. 992–1011, Nov. 2022, doi: 10.1515/ijmr-2021-8716.

[23] H. R. R. Ashtiani and P. Shahsavari, "A comparative study on the phenomenological and artificial neural network models to predict hot deformation behavior of AlCuMgPb alloy," *Journal of Alloys and Compounds*, vol. 687, pp. 263–273, Dec. 2016, doi: 10.1016/j.jallcom.2016.04.300.

[24] X. Wang, Q. Pan, S. Xiong, L. Liu, Y. Sun, and W. Wang, "Prediction on hot deformation behavior of spray-formed 7055 aluminum alloy via phenomenological models," *Transactions of Nonferrous Metals Society of China*, vol. 28, no. 8, pp. 1484–1494, Aug. 2018, doi: 10.1016/S1003-6326(18)64789-2.

[25] R. H. Buzolin, M. Lasnik, A. Krumphals, and M. C. Poletti, "Hot deformation and dynamic α-globularization of a Ti-17 alloy: Consistent physical model," *Materials & Design*, vol. 197, p. 109266, Jan. 2021, doi: 10.1016/j.matdes.2020.109266.

[26] P. R. Yang, M. H. Cai, C. F. Wu, J. H. Su, and X. P. Guo, "Strain-rate dependent hot deformation

behavior and mechanism of interphase- precipitated Ti-Mo-xNb steels: Physical modeling and characterization," *Materials Science and Engineering: A*, vol. 729, pp. 230–240, Jun. 2018, doi: 10.1016/j.msea.2018.05.045.

[27] S. Kumar, A. Karmakar, and S. K. Nath, "Construction of hot deformation processing maps for 9Cr-1Mo steel through conventional and ANN approach," *Materials Today Communications*, vol. 26, p. 101903, Mar. 2021, doi: 10.1016/j.mtcomm.2020.101903.

[28] D. Hu, L. Wang, N. Wang, M. Chen, and H. Wang, "Hot tensile deformation behaviors of TA32 titanium alloy based on back-propagation neural networks and three-dimensional thermal processing maps," *Journal of Materials Research and Technology*, vol. 18, pp. 4786–4795, May 2022, doi: 10.1016/j.jmrt.2022.04.144.

[29] W. Chen, S. Li, K. S. Bhandari, S. Aziz, X. Chen, and D. W. Jung, "Genetic optimized Al–Mg alloy constitutive modeling and activation energy analysis," *International Journal of Mechanical Sciences*, vol. 244, p. 108077, Apr. 2023, doi: 10.1016/j.ijmecsci.2022.108077.

[30] G. R. Johnson and W. H. Cook, "Fracture characteristics of three metals subjected to various strains, strain rates, temperatures and pressures," *Engineering Fracture Mechanics*, vol. 21, no. 1, pp. 31–48, Jan. 1985, doi: 10.1016/0013-7944(85)90052-9.

[31] A. Shrot and M. Bäker, "Determination of Johnson–Cook parameters from machining simulations," *Computational Materials Science*, vol. 52, no. 1, pp. 298–304, Feb. 2012, doi: 10.1016/j.commatsci.2011.07.035.

[32] A. Shokry, S. Gowid, and G. Kharmanda, "An improved generic Johnson-Cook model for the flow prediction of different categories of alloys at elevated temperatures and dynamic loading conditions," *Materials Today Communications*, vol. 27, p. 102296, Jun. 2021, doi: 10.1016/j.mtcomm.2021.102296.

[33] W. Jia, S. Xu, Q. Le, L. Fu, L. Ma, and Y. Tang, "Modified Fields–Backofen model for constitutive behavior of as-cast AZ31B magnesium alloy during hot deformation," *Materials & Design*, vol. 106, pp. 120–132, Sep. 2016, doi: 10.1016/j.matdes.2016.05.089.

[34] J. Shen, L. Hu, Y. Sun, Z. Wan, X. Feng, and Y. Ning, "A Comparative Study on Artificial Neural Network, Phenomenological-Based Constitutive and Modified Fields–Backofen Models to Predict Flow Stress in Ti-4Al-3V-2Mo-2Fe Alloy," *J. of Materi Eng and Perform*, vol. 28, no. 7, pp. 4302–4315, Jul. 2019, doi: 10.1007/s11665-019-04174-0.

[35] S. A. Sani, G. R. Ebrahimi, H. Vafaeenezhad, and A. R. Kiani-Rashid, "Modeling of hot deformation behavior and prediction of flow stress in a magnesium alloy using constitutive equation and artificial neural network (ANN) model," *Journal of Magnesium and Alloys*, vol. 6, no. 2, pp. 134–144, Jun. 2018, doi: 10.1016/j.jma.2018.05.002.

[36] D.-N. Zou, K. Wu, Y. Han, W. Zhang, B. Cheng, and G.-J. Qiao, "Deformation characteristic and prediction of flow stress for as-cast 21Cr economical duplex stainless steel under hot compression," *Materials & Design*, vol. 51, pp. 975–982, Oct. 2013, doi: 10.1016/j.matdes.2013.04.065.

[37] X. Huang, Y. Zang, and B. Guan, "Constitutive models and microstructure evolution of Ti-6Al-4V alloy during the hot compressive process," *Mater. Res. Express*, vol. 8, no. 1, p. 016534, Jan. 2021, doi: 10.1088/2053-1591/abdaf0.

[38] S. K. Paul, "Predicting the flow behavior of metals under different strain rate and temperature through phenomenological modeling," *Computational Materials Science*, vol. 65, pp. 91–99,

Dec. 2012, doi: 10.1016/j.commatsci.2012.06.039.

[39] S. J. Li, W. N. Chen, B. Krishna Singh, N. Kosimov, and D. W. Jung, "Study on Flow Stress Model of AA5005 Material," *Solid State Phenomena*, vol. 335, pp. 107–112, 2022, doi: 10.4028/p-4t00fs.

[40] W. N. Chen, S. J. Li, N. Kosimov, B. Krishna Singh, and D. W. Jung, "Research on High-Temperature Constitutive Relationship of Aluminum Alloy," *Solid State Phenomena*, vol. 335, pp. 101–106, 2022, doi: 10.4028/p-zr45qd.

[41] A. Shokry, S. Gowid, H. Mulki, and G. Kharmanda, "On the Prediction of the Flow Behavior of Metals and Alloys at a Wide Range of Temperatures and Strain Rates Using Johnson–Cook and Modified Johnson–Cook-Based Models: A Review," *Materials*, vol. 16, no. 4, p. 1574, Feb. 2023, doi: 10.3390/ma16041574.

[42] X. Chen *et al.*, "A constitutive relation of AZ80 magnesium alloy during hot deformation based on Arrhenius and Johnson–Cook model," *Journal of Materials Research and Technology*, vol. 8, no. 2, pp. 1859–1869, Apr. 2019, doi: 10.1016/j.jmrt.2019.01.003.

[43] F. Abbassi, M. Srinivasan, C. Loganathan, R. Narayanasamy, and M. Gupta, "Experimental and numerical analyses of magnesium alloy hot workability," *Journal of Magnesium and Alloys*, vol. 4, no. 4, pp. 295–301, Dec. 2016, doi: 10.1016/j.jma.2016.10.004.

[44] J. Q. Tan, M. Zhan, S. Liu, T. Huang, J. Guo, and H. Yang, "A modified Johnson–Cook model for tensile flow behaviors of 7050-T7451 aluminum alloy at high strain rates," *Materials Science and Engineering: A*, vol. 631, pp. 214–219, Apr. 2015, doi: 10.1016/j.msea.2015.02.010.

[45] S. Li, W. Chen, K. S. Bhandari, D. W. Jung, and X. Chen, "Flow Behavior of AA5005 Alloy at High-temperature and Low Strain Rate Based on Arrhenius-Type Equation and Back Propagation Artificial Neural Network (BP-ANN) Model," *Materials*, vol. 15, no. 11, p. 3788, May 2022, doi: 10.3390/ma15113788.

[46] A. Iturbe *et al.*, "Mechanical characterization and modelling of Inconel 718 material behavior for machining process assessment," *Materials Science and Engineering: A*, vol. 682, pp. 441–453, Jan. 2017, doi: 10.1016/j.msea.2016.11.054.

[47] S. Deb, A. Muraleedharan, R. J. Immanuel, S. K. Panigrahi, G. Racineux, and S. Marya, "Establishing flow stress behaviour of Ti-6Al-4V alloy and development of constitutive models using Johnson-Cook method and Artificial Neural Network for quasi-static and dynamic loading," *Theoretical and Applied Fracture Mechanics*, vol. 119, p. 103338, Jun. 2022, doi: 10.1016/j.tafmec.2022.103338.

[48] W. Yu, Y. Li, J. Cao, Z. Yang, J. Zhang, and S. Lang, "The dynamic compressive behavior and constitutive models of a near α TA23 titanium alloy," *Materials Today Communications*, vol. 29, p. 102863, Dec. 2021, doi: 10.1016/j.mtcomm.2021.102863.

[49] M. E. Korkmaz, "Verification of Johnson-Cook parameters of ferritic stainless steel by drilling process: experimental and finite element simulations," *Journal of Materials Research and Technology*, vol. 9, no. 3, pp. 6322–6330, May 2020, doi: 10.1016/j.jmrt.2020.03.045.

[50] R. Motallebi, Z. Savaedi, and H. Mirzadeh, "Additive manufacturing – A review of hot deformation behavior and constitutive modeling of flow stress," *Current Opinion in Solid State and Materials Science*, vol. 26, no. 3, p. 100992, Jun. 2022, doi: 10.1016/j.cossms.2022.100992.

[51] A. Shokry, "On the constitutive modeling of a powder metallurgy nanoquasicrystalline

Al93Fe3Cr2Ti2 alloy at elevated temperatures," *J Braz. Soc. Mech. Sci. Eng.*, vol. 41, no. 3, p. 118, Feb. 2019, doi: 10.1007/s40430-019-1617-y.

[52] Y. C. Lin, X.-M. Chen, and G. Liu, "A modified Johnson–Cook model for tensile behaviors of typical high-strength alloy steel," *Materials Science and Engineering: A*, vol. 527, no. 26, pp. 6980–6986, Oct. 2010, doi: 10.1016/j.msea.2010.07.061.

[53] D. Samantaray, S. Mandal, and A. K. Bhaduri, "A critical comparison of various data processing methods in simple uni-axial compression testing," *Materials & Design*, vol. 32, no. 5, pp. 2797–2802, May 2011, doi: 10.1016/j.matdes.2011.01.007.

[54] X. Chen *et al.*, "Identification of the Constitutive Model Parameters by Inverse Optimization Method and Characterization of Hot Deformation Behavior for Ultra-Supercritical Rotor Steel," *Materials*, vol. 14, no. 8, Art. no. 8, Jan. 2021, doi: 10.3390/ma14081958.

[55] B. Zhang *et al.*, "A Comparative Study on Johnson–Cook, Modified Johnson–Cook, Modified Zerilli–Armstrong and Arrhenius-Type Constitutive Models to Predict Hot Deformation Behavior of TA2," *High-temperature Materials and Processes*, vol. 38, no. 2019, pp. 699–714, Feb. 2019, doi: 10.1515/htmp-2019-0026.

[56] Y. C. Lin, M.-S. Chen, and J. Zhong, "Constitutive modeling for elevated temperature flow behavior of 42CrMo steel," *Computational Materials Science*, vol. 42, no. 3, pp. 470–477, May 2008, doi: 10.1016/j.commatsci.2007.08.011.

[57] P. Geng, G. Qin, J. Zhou, and Z. Zou, "Hot deformation behavior and constitutive model of GH4169 superalloy for linear friction welding process," *Journal of Manufacturing Processes*, vol. 32, pp. 469–481, Apr. 2018, doi: 10.1016/j.jmapro.2018.03.017.

[58] Y. B. Tan, Y. H. Ma, and F. Zhao, "Hot deformation behavior and constitutive modeling of fine grained Inconel 718 superalloy," *Journal of Alloys and Compounds*, vol. 741, pp. 85–96, Apr. 2018, doi: 10.1016/j.jallcom.2017.12.265.

[59] H.-Y. Li, Y.-H. Li, D.-D. Wei, J.-J. Liu, and X.-F. Wang, "Constitutive equation to predict elevated temperature flow stress of V150 grade oil casing steel," *Materials Science and Engineering: A*, vol. 530, pp. 367–372, Dec. 2011, doi: 10.1016/j.msea.2011.09.097.

[60] D. Samantaray, S. Mandal, and A. K. Bhaduri, "A comparative study on Johnson Cook, modified Zerilli–Armstrong and Arrhenius-type constitutive models to predict elevated temperature flow behaviour in modified 9Cr–1Mo steel," *Computational Materials Science*, vol. 47, no. 2, pp. 568–576, Dec. 2009, doi: 10.1016/j.commatsci.2009.09.025.

[61] P. Tize Mha, P. Dhondapure, M. Jahazi, A. Tongne, and O. Pantalé, "Interpolation and Extrapolation Performance Measurement of Analytical and ANN-Based Flow Laws for Hot Deformation Behavior of Medium Carbon Steel," *Metals*, vol. 13, no. 3, p. 633, Mar. 2023, doi: 10.3390/met13030633.

[62] D. Samantaray, S. Mandal, U. Borah, A. K. Bhaduri, and P. V. Sivaprasad, "A thermo-viscoplastic constitutive model to predict elevated-temperature flow behaviour in a titanium-modified austenitic stainless steel," *Materials Science and Engineering: A*, vol. 526, no. 1, pp. 1–6, Nov. 2009, doi: 10.1016/j.msea.2009.08.009.

[63] H. Zhan, G. Wang, D. Kent, and M. Dargusch, "Constitutive modelling of the flow behaviour of a β titanium alloy at high strain rates and elevated temperatures using the Johnson–Cook and modified Zerilli–Armstrong models," *Materials Science and Engineering: A*, vol. 612, pp. 71–79, Aug. 2014, doi: 10.1016/j.msea.2014.06.030.

[64] P. L. Sun, E. K. Cerreta, G. T. Gray, and J. F. Bingert, "The effect of grain size, strain rate, and temperature on the mechanical behavior of commercial purity aluminum," *Metall Mater Trans A*, vol. 37, no. 10, pp. 2983–2994, Oct. 2006, doi: 10.1007/s11661-006-0180-1.

[65] Y. Wang and Z. Jiang, "Dynamic compressive behavior of selected aluminum alloy at low temperature," *Materials Science and Engineering: A*, vol. 553, pp. 176–180, Sep. 2012, doi: 10.1016/j.msea.2012.06.010.

[66] F. J. Zerilli and R. W. Armstrong, "Dislocation-mechanics-based constitutive relations for material dynamics calculations," *Journal of Applied Physics*, vol. 61, no. 5, pp. 1816–1825, Mar. 1987, doi: 10.1063/1.338024.

[67] L.-L. Wang, "A Thermo-Viscoplastic Constitutive Equation Based on Hyperbolic-Shape Thermo-Activated Barriers," *Journal of Engineering Materials and Technology*, vol. 106, no. 4, pp. 331–336, Oct. 1984, doi: 10.1115/1.3225726.

[68] U. Andrade, M. A. Meyers, K. S. Vecchio, and A. H. Chokshi, "DRX in high-strain, high-strain-rate plastic deformation of copper," *Acta Metallurgica et Materialia*, vol. 42, no. 9, pp. 3183–3195, Sep. 1994, doi: 10.1016/0956-7151(94)90417-0.

[69] S. Kumar, B. Aashranth, M. A. Davinci, D. Samantaray, U. Borah, and A. K. Bhaduri, "Assessing Constitutive Models for Prediction of High-Temperature Flow Behavior with a Perspective of Alloy Development," *J. of Materi Eng and Perform*, vol. 27, no. 4, pp. 2024–2037, Apr. 2018, doi: 10.1007/s11665-018-3237-6.

[70] Y. C. Lin and X.-M. Chen, "A critical review of experimental results and constitutive descriptions for metals and alloys in hot working," *Materials & Design*, vol. 32, no. 4, pp. 1733–1759, Apr. 2011, doi: 10.1016/j.matdes.2010.11.048.

[71] Z. Savaedi, R. Motallebi, and H. Mirzadeh, "A review of hot deformation behavior and constitutive models to predict flow stress of high-entropy alloys," *Journal of Alloys and Compounds*, vol. 903, p. 163964, May 2022, doi: 10.1016/j.jallcom.2022.163964.

[72] H. Kobayashi and B. Dodd, "A numerical analysis for the formation of adiabatic shear bands including void nucleation and growth," *International Journal of Impact Engineering*, vol. 8, no. 1, pp. 1–13, Jan. 1989, doi: 10.1016/0734-743X(89)90027-4.

[73] W.-S. Lee, T.-H. Chen, and Q.-J. Gong, "Dynamic Shear Behaviour of Unweldable Aluminum-Scandium (Al-Sc) Alloy," *Mater. Trans.*, vol. 48, no. 3, pp. 500–509, 2007, doi: 10.2320/matertrans.48.500.

[74] W.-S. Lee, J.-I. Cheng, and C.-F. Lin, "Deformation and failure response of 304L stainless steel SMAW joint under dynamic shear loading," *Materials Science and Engineering: A*, vol. 381, no. 1–2, pp. 206–215, Sep. 2004, doi: 10.1016/j.msea.2004.04.034.

[75] D. Trimble and G. E. O'Donnell, "Constitutive Modelling for elevated temperature flow behaviour of AA7075," *Materials & Design*, vol. 76, pp. 150–168, Jul. 2015, doi: 10.1016/j.matdes.2015.03.062.

[76] Y. Q. Cheng, H. Zhang, Z. H. Chen, and K. F. Xian, "Flow stress equation of AZ31 magnesium alloy sheet during warm tensile deformation," *Journal of Materials Processing Technology*, vol. 208, no. 1, pp. 29–34, Nov. 2008, doi: 10.1016/j.jmatprotec.2007.12.095.

[77] Q. G. Zheng, T. Ying, and Z. Jie, "Dynamic softening behaviour of AZ80 magnesium alloy during upsetting at different temperatures and strain rates," *Proceedings of the Institution of Mechanical Engineers, Part B: Journal of Engineering Manufacture*, vol. 224, no. 11, pp. 1707–

1716, Nov. 2010, doi: 10.1243/09544054JEM1965.

[78] G.-Z. Quan, Y. Shi, Y.-X. Wang, B.-S. Kang, T.-W. Ku, and W.-J. Song, "Constitutive modeling for the DRX evolution of AZ80 magnesium alloy based on stress–strain data," *Materials Science and Engineering: A*, vol. 528, no. 28, pp. 8051–8059, Oct. 2011, doi: 10.1016/j.msea.2011.07.064.

[79] G. Quan, K. Liu, J. Zhou, and B. Chen, "Dynamic softening behaviors of 7075 aluminum alloy," *Transactions of Nonferrous Metals Society of China*, vol. 19, pp. s537–s541, Dec. 2009, doi: 10.1016/S1003-6326(10)60104-5.

[80] W. N. Chen, S. J. Li, K. S. Bhandari, S. Aziz, N. Kosimov, and D. W. Jung, "A Flow Stress Equation of AA5005 Aluminum Alloy Based on Fields-Backofen Model," *Materials Science Forum*, vol. 1078, pp. 3–10, 2022, doi: 10.4028/p-95f697.

[81] K.-T. Son, M.-H. Kim, S.-W. Kim, J.-W. Lee, and S.-K. Hyun, "Evaluation of hot deformation characteristics in modified AA5052 using processing map and activation energy map under deformation heating," *Journal of Alloys and Compounds*, vol. 740, pp. 96–108, Apr. 2018, doi: 10.1016/j.jallcom.2017.12.357.

[82] J. C. Malas, "Methodology for design and control of thermomechanical processes," Ph.D., Ann Arbor, United States. Accessed: May 18, 2023. [Online]. Available: https://www.proquest.com/docview/303932546/abstract/FF6D0BDA030E4F8FPQ/1

[83] C. Shi, W. Mao, and X.-G. Chen, "Evolution of activation energy during hot deformation of AA7150 aluminum alloy," *Materials Science and Engineering: A*, vol. 571, pp. 83–91, Jun. 2013, doi: 10.1016/j.msea.2013.01.080.

[84] H. Asgharzadeh, A. Simchi, and H. S. Kim, "Hot deformation of ultrafine-grained Al6063/Al2O3 nanocomposites," *J Mater Sci*, vol. 46, no. 14, pp. 4994–5001, Jul. 2011, doi: 10.1007/s10853-011-5418-7.

[85] H. J. McQueen, "Development of DRX theory," *Materials Science and Engineering: A*, vol. 387–389, pp. 203–208, Dec. 2004, doi: 10.1016/j.msea.2004.01.064.

[86] J. Zhang, H. Di, H. Wang, K. Mao, T. Ma, and Y. Cao, "Hot deformation behavior of Ti-15-3 titanium alloy: a study using processing maps, activation energy map, and Zener–Hollomon parameter map," *J Mater Sci*, vol. 47, no. 9, pp. 4000–4011, May 2012, doi: 10.1007/s10853-012-6253-1.

[87] M. yan Zhan, Z. Chen, H. Zhang, and W. Xia, "Flow stress behavior of porous FVS0812 aluminum alloy during hot-compression," *Mechanics Research Communications*, vol. 33, no. 4, pp. 508–514, Jul. 2006, doi: 10.1016/j.mechrescom.2005.05.008.

[88] H. Mirzadeh, "A Simplified Approach for Developing Constitutive Equations for Modeling and Prediction of Hot Deformation Flow Stress," *Metall Mater Trans A*, vol. 46, no. 9, pp. 4027–4037, Sep. 2015, doi: 10.1007/s11661-015-3006-1.

[89] J. Long, Q. Xia, G. Xiao, Y. Qin, and S. Yuan, "Flow characterization of magnesium alloy ZK61 during hot deformation with improved constitutive equations and using activation energy maps," *International Journal of Mechanical Sciences*, vol. 191, p. 106069, Feb. 2021, doi: 10.1016/j.ijmecsci.2020.106069.

[90] Z. Mingjie, L. Fuguo, W. Shuyun, and L. Chenyi, "Characterization of hot deformation behavior of a P/M nickel-base superalloy using processing map and activation energy," *Materials Science and Engineering: A*, vol. 527, no. 24, pp. 6771–6779, Sep. 2010, doi:

10.1016/j.msea.2010.07.039.

[91] F. J. Humphreys and M. Hatherly, *Recrystallization and Related Annealing Phenomena*. Elsevier, 2012.

[92] Q.-X. Xia, J.-C. Long, N.-Y. Zhu, and G.-F. Xiao, "Research on the microstructure evolution of Ni-based superalloy cylindrical parts during hot power spinning," *Adv. Manuf.*, vol. 7, no. 1, pp. 52–63, Mar. 2019, doi: 10.1007/s40436-018-0242-9.

[93] X. Chen, Y. Du, T. Lian, K. Du, and T. Huang, "Hot Workability of Ultra-Supercritical Rotor Steel Using a 3-D Processing Map Based on the Dynamic Material Model," *Materials*, vol. 13, no. 18, Art. no. 18, Jan. 2020, doi: 10.3390/ma13184118.

[94] X. Chen *et al.*, "An enhanced lemaitre damage model and verification method for X12 alloy steel in hot forming process," *Engineering Fracture Mechanics*, vol. 273, p. 108711, Oct. 2022, doi: 10.1016/j.engfracmech.2022.108711.

Publications during the master's degree period

SCI index:

[1] S. Li, W. Chen, K. S. Bhandari, D. W. Jung, and X. Chen, "Flow Behavior of AA5005 Alloy at High Temperature and Low Strain Rate Based on Arrhenius-Type Equation and Back Propagation Artificial Neural Network (BP-ANN) Model," *Materials*, vol. 15, no. 11, p. 3788, May 2022, doi: 10.3390/ma15113788.

[2] W. Chen, S. Li, K. S. Bhandari, S. Aziz, X. Chen, and D. W. Jung, "Genetic optimized Al–Mg alloy constitutive modeling and activation energy analysis," *Int. J. Mech. Sci.*, vol. 244, p. 108077, Apr. 2023, doi: 10.1016/j.ijmecsci.2022.108077. (Common first author).

[3] S. Aziz, J. Ali, K. S. Bhandari, W. Chen, S. Li, and D. W. Jung, "Reverse Offset Printed, Biocompatible Temperature Sensor Based on Dark Muscovado," *Sensors*, vol. 22, no. 22, Art. no. 22, Jan. 2022, doi: 10.3390/s22228726.

Scopus index:

[4] S. J. Li, W. N. Chen, K. S. Bhandari, N. Kosimov, and D. W. Jung, "Study on Flow Stress Model of AA5005 Material," *Solid State Phenom.*, vol. 335, pp. 107–112, 2022, doi: 10.4028/p-4t00fs.

[5] S. Li, W. Chen, N. Kosimov, S. B. Krishna, and D. Jung, "Reduction of Explicit Incremental Forming Simulation Time by Mass Scaling Parameters Adjusting and Symmetrical Setting," *Int. J. Technol. Eng. Stud.*, vol. 7, no. 1, pp. 27–34, doi: https://dx.doi.org/10.20469/ijtes.7.10004-1.

[6] S. J. Li, W. N. Chen, S. Aziz, K. S. Bhandari, and D. W. Jung, "Modified Johnson-Cook model of AA5005 alloy for thermal tensile tests", accepted.

[7] W. N. Chen, S. J. Li, N. Kosimov, K. S. Bhandari, and D. W. Jung, "Research on High-Temperature Constitutive Relationship of Aluminum Alloy," *Solid State Phenom.*, vol. 335, pp. 101–106, 2022, doi: 10.4028/p-zr45qd.

[8] W. N. Chen, S. J. Li, K. S. Bhandari, S. Aziz, N. Kosimov, and D. W. Jung, "A Flow Stress Equation of AA5005 Aluminum Alloy Based on Fields-Backofen Model," *Mater. Sci. Forum*, vol. 1078, pp. 3–10, 2022, doi: 10.4028/p-95f697.

[9] W. Chen, S. Li, S. B. Krishna, N. Kosimov, and D. Jung, "Comparison of Shell Thickness Integration Rules and Element Types on Single Point Incremental Forming (SPIF) Simulation," *J. Adv. Technol. Eng. Res.*, vol. 7, no. 1, pp. 17–24, 2021, doi: https://doi.org/10.20474/jater-7.1.3.

[10] K. S. Bhandari, M. Murugesan, S. J. Li, W. N. Chen, J. Moon, and D. W. Jung, "Incremental Sheet Forming Simulation of Aluminum Alloys for Industry Level Production," *Mater. Sci. Forum*, vol. 1054, pp. 129–133, 2022, doi: 10.4028/p-bgl4ij.

[11] N. Kosimov, K. S. Bhandari, S. J. Li, W. N. Chen, J. Moon, and D. W. Jung, "Modeling Process of Manufacturing Parts Using Incremental Forming Process," *Solid State Phenom.*, vol. 330, pp. 45–49, 2022, doi: 10.4028/p-gs3z36.

[12] N. Kosimov, K. S. Bhandari, S. J. Li, W. N. Chen, and D. W. Jung, "Single Point Incremental Forming as a Cost-Effective Sheet Forming Process for Small Batch Production," *Appl. Mech. Mater.*, vol. 908, pp. 169–175, 2022, doi: 10.4028/p-77k9g3.

[13] N. Kosimov, K. S. Bhandari, S. J. Li, W. N. Chen, J. Moon, and D. W. Jung, "Developing Methods of Forming Sheet Materials Using Incremental Forming," *Mater. Sci. Forum*, vol. 1054, pp. 123–127, 2022, doi: 10.4028/p-51vr3j.

[14] K. S. Bhandari, W. N. Chen, S. J. Li, and D. W. Jung, "Formability of Aluminum in Incremental Sheet Forming," *Solid State Phenom.*, vol. 330, pp. 77–81, 2022, doi: 10.4028/p-25oilk.

[15] K. S. Bhandari, S. Aziz, W. N. Chen, S. J. Li, and D. W. Jung, "Forming Parameters and Optimization of A5052 in SPIF Process," *Mater. Sci. Forum*, vol. 1084, pp. 85–89, 2023, doi: 10.4028/p-248h81.

[16] K. S. Bhandari, S. Aziz, W. N. Chen, S. J. Li, and D. W. Jung, "Deformation Evaluation of A5052 Sheet Metal in SPIF Process," *Mater. Sci. Forum*, vol. 1084, pp. 91–95, 2023, doi: 10.4028/p-e6768o.